



A computational study of the stability and growth of Au clusters on MgO.

This thesis is being submitted in partial fulfilment of the requirements for the degree of PhD.

By Samantha Francis

May 2020

Summary

Supported gold nanoparticles are used for a wide range of catalytic processes. For example, Au/MgO catalysts are used in the low temperature oxidation of CO and the oxidation of alcohols. In this work, the most stable Au clusters of sizes up to 19 atoms on MgO(001) are determined (Au_n/MgO , $n < 20$). The Au clusters are created through the employment of two methods using DFT to minimise the electronic structure: i) a systematic build-up method and ii) unbiased global optimisation methods, i.e. genetic algorithm and basin hopping Monte Carlo. Optimisations are performed using dispersion corrected density functional theory (DFT-D). Trends relating to the structural and electronic properties that are associated with an increase in cluster size, are also evaluated and discussed concluding that as the Au clusters increase in size, they transition from perpendicular planar structures to parallel planar structures with an Au (111) interface configuration with the MgO support.

Searches for stable clusters performed with a Monte Carlo global optimisation procedure used empirical potentials to determine the energy. The resulting structures were subsequently optimised using DFT to determine the validity of the method for the Au_n/MgO ($n < 20$) system, and comparisons of the energetic and structural parameters of the clusters made to the findings of the previous search methods employing DFT. However, this methodology was not successful for determining the most stable clusters for the system (where $n < 20$).

Once the most stable Au_n/MgO systems were determined, the structures were employed in a study of the Ostwald ripening growth process. We have employed DFT calculations to calculate the barriers associated with ripening, combined with microkinetic simulations to investigate two mechanistic processes, ripening and digestion, relating to Au clusters size changes on a MgO(001) support.

Acknowledgements

Firstly, I would like to offer my deepest gratitude to my supervisor Dr Alberto Roldan, for his ongoing guidance and unwavering patience throughout the time we have been working together. I could not have imagined a better advisor and mentor whilst completing my PhD research.

Additional thanks must go to everyone in the Roldan group and department as a whole, with particular mention to Julien and Cameron for all their help and also Harry, Ali, Fabrizio, Matt, and Stefan for all the enlightening discussions over the years, without whom the office would have been a very dull place.

I must also extend my sincere thanks to Prof. Riccardo Ferrando and his group at University of Genoa for all the help and guidance offered to me during my visit to Italy with the HPC-Europa.

I would also like to acknowledge funding/CPU-time from Cardiff University, the Engineering and Physical Sciences Research Council (EPSRC), the High-performance computing (HPC) Materials Consortium (UK) and the HPC-Europa Transnational Access Programme (EU).

Last, but certainly not least, I would like to acknowledge the love and support of my family. In particular, my wonderful partner, Dan.

Contents

Introduction.....	1
Nanoparticle size and shape	2
Size effects	2
Shape effects.....	4
Dispersion	5
Catalyst preparation	6
Catalyst preparation of Au _n /MgO catalysts	7
Growth and stability of nanoparticles.	8
Nucleation.....	8
Nanoparticle growth	10
Catalyst deactivation.....	12
Sintering.....	13
Experimental techniques for observing sintering processes.	16
Nanoparticle morphology	17
Supported nanoparticles.....	20
References	23
Theoretical background.....	32
Electronic structure.....	32
Density functional theory (DFT).....	33
Functionals.....	35
Basis set - planewaves	36
Dispersion forces.....	38
Atomic charges.....	38
Exploration of the potential energy surface (PES).....	39
Minimisation to the ground state	39
Transition state methods.....	40
Model description.....	42
Characterisation.....	43
Band structures, Density of states (DOS) and Crystal Orbital Hamilton Population. (COHP).....	43
References	47
Au_n/MgO cluster determination using DFT methods.....	50
Introduction	50
Methodology.....	51
Computational details.....	51

General methodology	52
Measurements	52
Results	53
MgO support	53
Structure of supported Au clusters.....	54
Structural trends of the lowest energy Au _n structures.....	65
Adsorption, cohesion and binding energies	67
Electronic charge analysis	70
Bader charges.....	70
Density of states (DOS) and Crystal Orbital Hamilton Populations (COHP).....	71
Conclusions	77
References	79
Growth of Au_n on MgO surfaces – Ostwald ripening	83
Introduction	83
Ostwald ripening.....	84
Smoluchowski ripening or Coalescence.....	84
Ostwald or Smoluchowski ripening?.....	85
Methodology.....	86
Microkinetic methodology.....	88
Metal dispersion	91
Results and Discussion	92
Migration mechanism	92
Ostwald Ripening mechanism.....	94
Microkinetic modelling	98
Ripening	99
Digestion	103
Conclusions	106
References	108
Monte Carlo global optimisation	112
Introduction	112
Simple pair potentials	112
Methodology.....	114
Empirical potentials	114
Monte Carlo global optimisation	116
Monte Carlo optimisation algorithms.....	117
Results and discussion	118

Results from Au ₅₀ and Au ₇₀ calculations	118
Results for Au _n /MgO (n = 5-20).....	120
Discussion of the Monte Carlo method for Au _n /MgO systems.....	123
Interface epitaxy	124
Mismatch	124
Conclusions	127
References	128
Conclusions.....	130

Chapter 1

Introduction

A catalyst, in simple terms, is a substance that accelerates a chemical reaction without itself being affected. For many reactions in chemical industry, catalysts are extremely important, if not vital,¹ as they serve to reduce the activation barriers and increase selectivity to reactions.

Examples of major industrial process that rely on catalysts include, the water gas shift reaction for the production of hydrogen, the contact process in the production of sulphuric acid and the Haber process for the production of ammonia.² The products formed in these processes go on to be used in further reactions to form a wide range of other products. For this reason, the utilisation and performance of a catalyst has huge financial implications.

The catalyst can come in many forms, but can be categorised into, homogenous, heterogeneous and biological. However, discussion in this thesis will focus on heterogeneous alone. For heterogeneous catalysts (those which are typically found in the solid state, whereas the reactants are gas or liquid phase) their efficacy can be determined by the quality of the catalyst surface.³⁻⁷ This is because heterogeneous catalytic reactions usually follow a series of common steps:

- Adsorption of reactant to active site.
- Chemical transformation for the formation of products.
- Desorption of products from the active site.

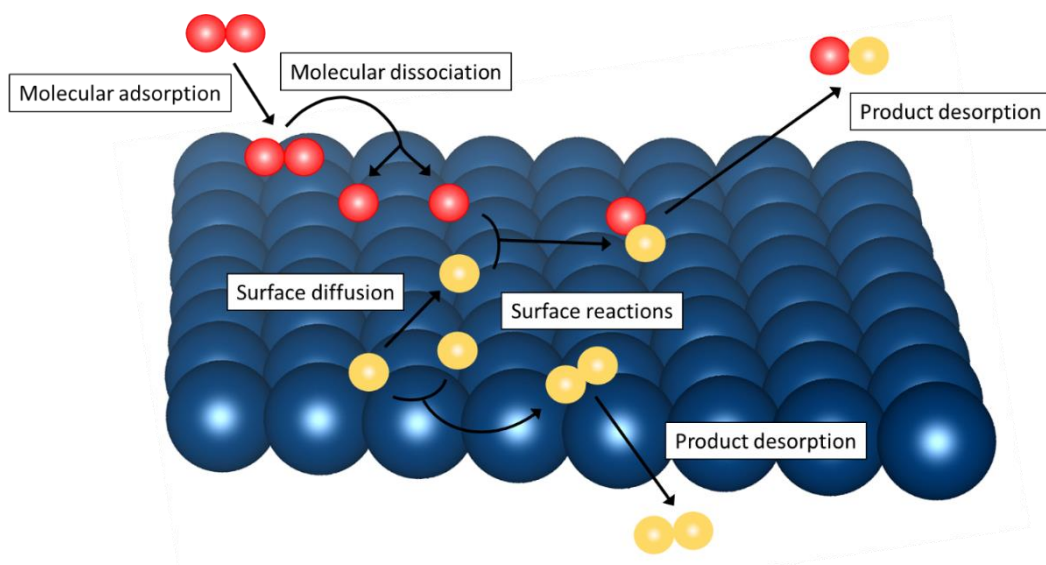


Figure 1.1: Adsorption, transformation and desorption of molecules on a catalytic surface. The blue atoms represent the atoms in the surface, whilst the yellow and red atoms represent reacting particles.

A careful balance between adsorption and desorption needs to be set up to allow for product formation. This relationship is described by the Sabatier principle,^{8,9} which states that the interactions of the species with the surface must not be too strong or too weak. A stronger than desired interaction will prevent the species from moving to the next stage and may lead to the poisoning of the catalyst. A weaker than required interaction will prevent the reactant from “sticking” to the surface long enough to support a successful reaction, rendering the catalyst ineffective.¹⁰ The adsorption and desorption processes are characterised by the degree of interaction that the catalyst surface has with reacting molecules. This is governed by the orbital interactions, that lead to bonding and anti-bonding states.

The adsorption, reaction and desorption steps occur on a catalyst at a region called an “active site”, an ensemble of atoms responsible for the catalysis of a reaction. An understanding of the structure and composition of the active site for particular reaction is of great importance to maximise the number of active sites during the production of an efficient catalyst.

Nanoparticle size and shape

Size effects

Commonly, heterogeneous catalysts are formed by a large area of material which supports metal nanoparticles, that form the active sites. Metal nanoparticles (NPs) are a collection of bonded atoms that may consist of particle arrangements, the size of these particles dictates the number of atoms as well as the particular arrangements present. Depending on the number of atoms that make up these NPs, they are also termed “clusters”. In this thesis, the term “clusters” is used interchangeably with nanoparticles for structures below 1.5 nm in size.

For supported metal catalysts, the properties that govern the careful balance between adsorption and desorption of molecular species are described by the geometric and electronic structure of these active sites. Typically a particular arrangement of atoms that make up the active site, is especially effective for reaction transformations. Therefore, numerous researchers have determined that controlling particle size is of vital importance to control the activity^{3,6,11,12} and the selectivity^{13–15} of the catalyst. This because the properties of the active site change with size. For example, once particle size reaches the “nano” scale, i.e. 1nm, then size of the particle is too small to be comparable to the wavelength of the electron and quantum size effects play a significant role in terms of the electronic characteristics.¹⁶ At quantum sizes, the electronic structure changes from a band structure in the bulk to discrete energy levels in isolated atoms, see Figure 1.2. This results in the production of discrete energy levels in the electronic spectrum rather than the expected continuum seen as for extended metals, due to the reduction in the number of electrons.^{17–19} Electron transition between the states affect the emission and adsorption of photons, resulting in large changes to the optical properties of semi-conductors and metals, as a function of particle size. For instance, colloidal suspensions of Au show different colours depending on the size of the nanoparticles.²⁰

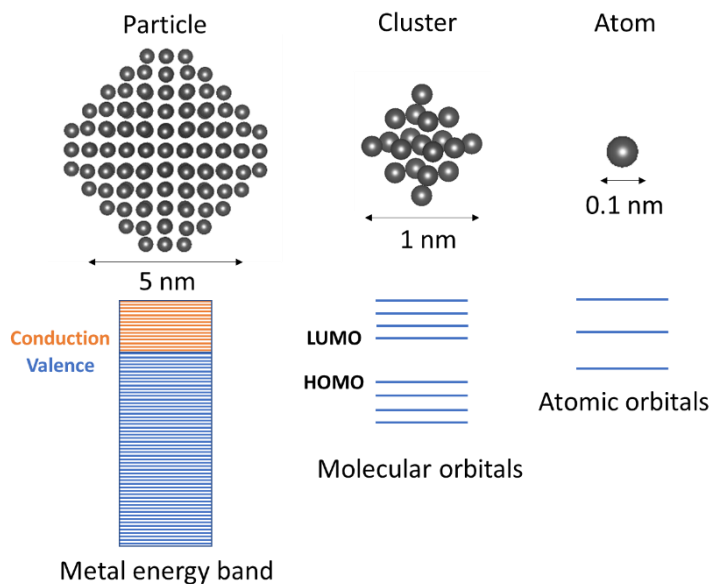


Figure 1.2: Diagram showing how the electronic band structure changes with the number of atoms.

The structural properties of “nano” particles are also important. All atoms in a particle can be divided into surface atoms and atoms in the bulk. The smaller the particle the greater the presence of surface sites, e.g. an Au_{13} cluster has 92% of its atoms on the surface, whilst an Au_{55} cluster has 76% of its atoms on the surface.²¹ The ratio of the bulk atoms sharply increases with nanoparticle size, for example for a spherical particle 10 nm in size, the

calculated surface to volume ratio is $3 \times 10^8 \text{ m}^{-1}$, for a nanoparticle 1 nm in size this is increased to $3 \times 10^9 \text{ m}^{-1}$. The importance of surface atoms is that they are bound to fewer neighbouring atoms, therefore, the smaller the particle, the greater the ratio of surface atoms and the greater the presence of under coordinated sites. An illustration of this is shown in Figure 1.3. For a FCC metal, the atoms in the bulk will have a coordination number of 12, for atoms on a terrace, the coordination decreases to 9, for a step site, this decreases to 7, and at an edge site the atom has a coordination of 6.

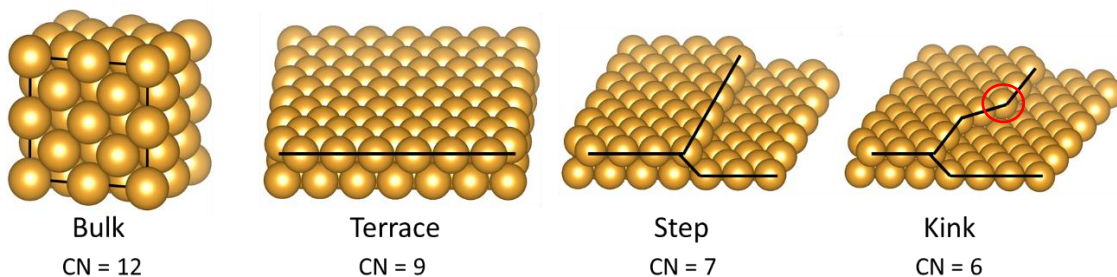


Figure 1.3: Illustration of the various sites on a regular FCC surface. CN is the coordination number for an atom at that site.

Particles with lower coordination numbers tend to be more reactive as lower coordination leads to less stability and higher reactivity.²² For example, DFT calculations show that adsorption of CO and O is stronger on Au edge atoms at steps and kinks than on terrace sites.^{23,24} Under coordinated sites have often been shown to be the active sites for a reaction. For instance, in the case of Cu and Cu-Zn catalysts for methanol synthesis, step sites provide lower energy barriers to dissociation reactions and transitions states and hence, the greater formation of products.⁵ Therefore, for this reaction, in order to provide enough of these step sites, the particles needed to be 8 – 15 nm in diameter, i.e. not too small and not too big.

Shape effects

While the size of a nanoparticle can affect its properties, their shape has also been seen to have an effect, often in similar ways. An example of how the shape of supported catalysts effects reactivity can be found in relation to the Fischer-Tropsch reaction, where synthesis gas (H_2 and CO) is converted into hydrocarbons of various chain lengths. It was observed by Mandić *et al.*²⁵ that maintaining activity for larger cluster sizes was achievable by the creation of “eggshell” particles. These hollow, spherical particles allowed for better flow of species in the reaction medium around the active metal component, helping to avoid limitations in gas diffusion and increased catalyst efficiency as a result.

Nanoparticle shape has also been shown to influence CO oxidation activity by Janssens *et al.*²⁶ in a study using various supports with varying NP shapes. The results determined that

smaller, more rounded particles were more efficient and it was concluded that catalyst efficiency and the significance of shape for this reaction is directly related to the number of atoms at particular sites, e.g. Au atoms at corner sites were found to be more reactive than higher coordinated sites, thus, the greater the number of corner sites determined by the shape the nanoparticle adopts, the greater the conversion to CO₂.

Additionally, the creation of more complex and unusual 3D morphologies has also produced structures with interesting properties. For example, gold nanorods (Au NRs) have found uses in biological applications, such as sensors and drug-delivery systems as they exhibit unique optical properties.²⁷ Compared to spherical Au NPs, nanorods have stronger light scattering properties from stronger surface plasmon resonance allowing them to be used in applications such as the detection of pathogenic DNA.

The influence that shape has on reactivity extends even further for multi-metallic systems and their applications. However, discussion in this thesis is limited to monometallic NP systems due to the nature of the research performed.

Dispersion

Supported catalyst efficiency is generally increased by a more dispersed surface. A catalyst with a greater metal dispersion is characterised by more metal atoms being exposed on the surface, with fewer atoms making up the bulk volume of the particles. The better the dispersion, the smaller the size of the metal particles and the greater the number of available surface sites. As described, low coordinated sites are often more reactive, and as a result, there is more active material available for reaction in the form of a greater number of active sites. While the active site differs from reaction to reaction, generally, an effective catalyst surface consists of a series of well-dispersed, active, metal moieties. As an added benefit, higher dispersion also means a smaller amount of metal is necessary to produce a viable number of active sites. The metals used in catalysis are often noble metals that are highly valuable, such as platinum, palladium, gold, silver and ruthenium, as such, the task in creating well-dispersed, active catalysts should be an actively undertaken one. A greater dispersion also has the added benefit of reducing the rate of sintering processes, which are explained later.

Catalyst preparation

Initially, the composition of a heterogeneous catalyst is dictated during preparation. There are a range of methods for catalyst preparation and these have varying results in terms of

their ability to create effective surfaces with active nanoparticles of a specific size and shape with narrow distributions.²⁸ As a result, there is no single description of how a solid-state catalyst can be made. In basic terms, to prepare a metal supported catalyst, the idea is to induce some interaction between the support materials and the metals in a way that produces a combined material with catalytic properties. The general steps followed for creating a heterogeneous catalyst are: the selection of components, i.e. the support, salt precursors, required promoters and solvents, preparation conditions (temperature, pH), the mixing of the components (the order of which varies for the method type) and subsequent treatments like drying or calcining techniques.

There are many different methods used to prepare supported metal catalysts, each with their own adaptations. The wide range of nanoparticle sizes and shapes obtained by different preparation methods, for the same system, shows how important the preparation is to the surface of the resulting catalyst. The following section is a brief description of a few of these methods, in order to give the general idea behind each.

Impregnation methods rely on the interaction between the active metal component and the support. They involve interactions including ion exchange and adsorption processes and are governed by the point of zero charge (PZC) of the surface and the choice of metal salt. The PZC is the pH at which the net charge of the adsorbent surface equals zero²⁹ and influences the degree of interaction adsorbates have to the surface. Working at pH's below the surface PZC means that the support's surface is saturated with positive charges, above the PZC the surface is negatively charged. This influences the interaction of the surface with adsorbates and effects how metals are deposited onto the catalyst support. This then results in varying dispersions of varying sized metal nanoparticles.

Precipitation methods produce crystallites in solution which can then be deposited onto a chosen support. A chemical precipitation method for the synthesis of NP's is generally a multi-step process. The metal atoms may undergo an initial reduction by various agents, e.g. borohydrides. This is followed by stabilisation of the particles using adsorbents such as polymers and surfactants like cetyltrimethylammonium bromide (CTAB),³⁰ which prevents the agglomeration of nanoparticles, minimising the distribution of particle sizes. Precipitation methods are generally more successful than impregnation in terms of preparing small nanoparticles with narrower size distributions.³¹

These descriptions satisfy the general procedures of traditional methods, however, exact preparation details vary wildly as procedures used by individual experimentalists often have

alterations. Additionally, working parameters such as pH, temperature, precursors used, stirring during synthesis and subsequent activation treatments (e.g. calcination) are all important factors in the shape/size of the resultant nanoparticles and in turn catalytic processes. This being said, a “trial-and-error” methodology is often adopted³² and it would be of great benefit to guide catalyst preparation with a more operational methodology to save both time and cost.

Once catalyst preparation has been completed, characterisation of catalysts can be performed with many experimental methods including: Extended X-ray adsorption fine structure (EXAFS), diffuse reflectance infrared fourier transform spectroscopy (DRIFTS), X-ray adsorption spectroscopy (XAS), mass spectroscopy (MS) and various imaging techniques, e.g. transmission electron microscopy (TEM) and scanning tunnelling microscopy (STM). These techniques aim to help experimentalists understand the exact nature of what is being formed by these preparation methods.

Catalyst preparation of Au_n/MgO catalysts

The system discussed in this thesis is Au_n/MgO ($n < 20$ atoms), and, with regard to creating small Au NP/MgO systems in particular, a wide range of preparation methods have been used, in order to increase the control of NP formation. Some of these methods and their results are described below.

Impregnation procedures are used regularly due to the ease of the method, rather than its success in producing small NP catalysts. A large Au particle size distribution with particle sizes of between 5 nm-10 nm is typically obtained.^{33,34} The agglomeration of these Au NP's is expedited further with use of chloride salts, typically used in this method.³⁵ Moreover, the low pH levels of the Au precursors can cause degradation of the MgO support, rendering impregnation a poor technique for synthesising small Au clusters on MgO.³⁶ However, a modified version of impregnation, called the double impregnation method (DIM)³⁷ shows size distributions of 2-12 nm, with an average particle size of 5.4 nm.³⁸

Precipitation approaches, such as deposition precipitation (DP) see better results in producing small supported nanoparticles. DP has produced catalysts with Au NP's of around 3-6 nm.³⁹⁻⁴¹ In addition, the use of a base in the metal solution raises the pH, avoiding MgO support degradation. This makes precipitation methods a better choice for creating an Au/MgO catalyst. Gold nanoparticles of 6 nm were reported in the literature for Au/MgO catalysts prepared by co-precipitation (CP) and on a pre hydroxylated MgO surface, NP size

decreases to 4 nm.⁴² Sol-immobilisation has been used to produce catalysts with average Au sizes of 2.6 nm by Bogdanchikova *et al.*⁴¹ and 4 nm when prepared by Gaiassi *et al.*⁴⁰

It is intended that the information gathered from computational studies can be used in conjunction with experimental findings to ultimately understand the relationship between the structure of a catalyst, the resulting properties and the catalytic performance. The recent improvements in the characterisation of catalysts using experimental methods,⁴³ in partnership with the advancements in computational methods have meant that characterisation of metal supported catalysts has become increasingly more instructive and has helped to guide development of catalysts with desired properties.^{44,45}

Growth and stability of nanoparticles.

Nucleation

Greater understanding of the nucleation stage during NP formation may help to provide information pertaining to the generation of nanoparticles with specific sizes and shapes.

Nucleation can be defined as the localised formation of a distinct phase. Nucleation is a competition between creating a more stable phase and the energy cost of creating a new surface. As an extension of this, nucleation is the first step in the formation of a new crystallite. In terms of heterogeneous catalysis nucleation this may start from the first metal atom on the surface of a support, which may then come together with other atoms to form seeds. As the system undergoes growth processes, the seeds being to form thermodynamically stable clusters, Figure 1.4.

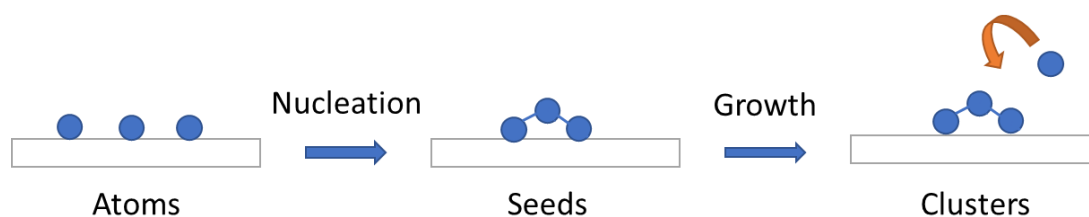


Figure 1.4: Illustration representing the nucleation of seeds on a support, followed by growth processes to form clusters.

There are two types of nucleation: heterogeneous and homogeneous. The former being much more commonplace than the latter. Homogeneous nucleation occurs without preferential sites and it requires more energy than heterogeneous nucleation, from the requirement of the exposure of a new surface and does not proceed without supercooling or superheating of the mixture. Supercooling occurs from decreasing the temperature of a liquid to below its freezing point without crystallisation and aids homogeneous nucleation by increasing the saturation of the medium. Supersaturation brings about a change in free energy, which can balance the cost of creating a new interface, thereby aiding in nucleation. Superheating occurs from increasing the temperature of a liquid to above its boiling point without vaporisation. In a super-heated state, nucleation sites will form from the energy of the increased temperatures. This energy breaks the bonds within the system until the creation of a new phase, e.g. steam forming from water. When the overall free energy change is negative, nucleation becomes favourable, see Figure 1.5. At critical seed size (r^*) nucleation proceeds, as now the nucleus is large enough, and the volume energy high enough, to satisfy the energy needed to create a new surface.

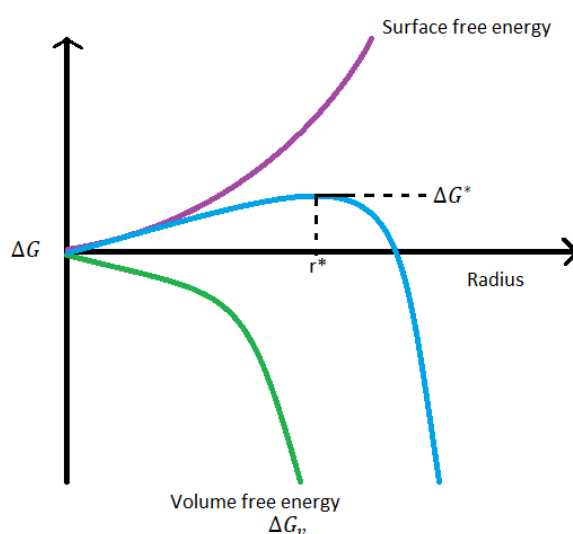


Figure 1.5: Free energy and its relation to homogeneous nucleation of NP's

Heterogeneous nucleation occurs at preferential sites, called nucleation sites, or on a support that provides a lower effective surface area, e.g. at phase boundaries, defects or impurities, lessening the otherwise high free energy barrier that restricts nucleation.^{46,47} For instance, the presence of the MgO support in the Au_n/MgO system means that seeds will be formed by heterogeneous nucleation. Surfaces promote nucleation because of a phenomenon called wetting. The wettability is the affinity of the new phase (in our case Au atom clusters) to adhere to the extended surface. As described, nucleation occurs more readily at surfaces, but even more readily at high energy sites like defects. This can be

explained by the increased binding energies with Au. This increased binding energy anchors the atom, and so it becomes the site for more Au atoms to form a cluster,⁴⁸ therefore, facilitating nucleation even further than when occurring on pristine surfaces. Case in point, it has been found with Au on oxide surfaces that nucleation occurs at edge, step and defect sites preferentially, particular when Au loading is low.^{49–52}

According to Ferrando and Fortunelli,⁵³ mobility studies are an excellent way to determine favourable nucleation sites. If atom mobility is lower, the atom will find it harder to move across the surface, requiring more energy, i.e. temperature, to do so. The atom, is therefore, much less likely to find one of these anchoring defective sites and will settle with binding to a less favourable site (terrace). Thus, the faster the diffusion the more likely it is that nucleation will occur only at defect sites. There are therefore, two factors that drive nucleation: a low free energy barrier to the seed radius (r^*) and a low diffusion barrier for atom migration across the surface of the support.

The rate of nucleation also has an influence on particle size: a fast nucleation relative to growth rate results in a larger number of crystallites of smaller size. Whilst the growth processes are dominant over nucleation, then fewer nanoparticles of larger sizes are produced. The stability of the system dictates the balance of these rates. In terms of catalyst synthesis, colloidal and co-precipitation methods rely on the observation of this nucleation rate to control particle morphologies. However, once formed, the stability is key to avoid growth via, for example, sintering processes.

Nanoparticle growth

Once the nucleation of a new phase has occurred, the system will undergo further processes, resulting in cluster growth, driven by thermodynamics. Larger particles have a lower surface to volume ratio, which results in a lower energy state with lower surface energy (γ), therefore, larger particles are more stable than smaller particles. Thus, larger particles continue to grow and smaller particles shrink and even disappear, often called ripening or coarsening.⁵⁴ Smaller clusters will diffuse to join larger clusters, or atoms from smaller, more energetically unfavourable particles will detach to join larger particles. Further discussion of growth processes, relating to the specific mechanisms of growth: Ostwald ripening and coalescence can be seen in Chapter 4. This is due to the Gibbs-Thompson relation,⁵⁵ which states that the chemical potential (or the partial molar free energy) of a metal atom in a particle of radius R , $\mu(R)$, differs from that in the bulk, $\mu(\infty)$ by:

$$\mu(R) - \mu(\infty) = \frac{2\gamma_m\Omega}{R} \quad (1.1)$$

Where γ_m is the surface free energy of the metal and Ω is the bulk metals volume per atom. This relation states that the larger the surface free energy (higher ratio of surface to bulk atoms) and the larger the bulk metal volume per atom, the greater the difference in chemical potential and the greater the drive to ripening.

The driving force of the growth processes, is therefore, the chemical potential of the cluster atoms on the support. The chemical potential is a measure of how much the free energy of a system changes when a number particles of the particle species (N_i) is altered while the number of the other particles ($N_{j \neq i}$), temperature (T) and the pressure (P) are kept constant⁵⁶.

$$\mu_i = \left(\frac{\partial G}{\partial N_i} \right)_{T,P,N_{j \neq i}} \quad (1.2)$$

The atoms in a smaller NP with a greater ratio of surface atoms will have a greater chemical potential than the atoms in an NP with a greater volume and a larger ratio of bulk atoms. Therefore, by adding more atoms to the particle the chemical potential of the system decreases towards the bulk, the ΔG decreases and lessens the drive to ripening.

For a supported nanoparticle, the usual Gibbs-Thompson relationship also needs to consider adhesion energy to the support, by increasing the adsorption of the nanoparticle to the support, the chemical potential can decrease. In turn, the drive to larger nanoparticles through growth processes would be reduced. Understanding the relationship between adsorption and growth of NP's could help to produce narrower size distributions of particular particle sizes.

For smaller cluster sizes (< 6 nm), as seen in the Au_n/MgO ($n= 1-19$) systems discussed in this work, it has been found that a much more accurate description of chemical potential as a function of particle size can be found using an empirical addition, fitted to a 1.5 nm particle. Failings of the usual equations (1.1 and 1.2) in describing the chemical potential of a nanoparticle of small size (< 6 nm) comes from a greater than expected increase change in potential with very small particle sizes. Thus, surface energy is of greater concern and the chemical potential must account for the larger proportion of atoms with lower coordination numbers.

Catalyst deactivation

Catalyst deactivation is of significant detriment to the operation of a heterogenous catalyst and the process that it catalyses. Deactivation causes a decline in the activity and/or selectivity of the catalyst, reducing its performance and leading to a decrease in the amount of the desired product obtained.^{57–59} Reduction in performance is caused by: i) a decrease in the number of active sites, ii) a decrease in the quality of the active sites or iii) a reduction in the accessibility to the active site.

There are many processes that can lead to catalyst deactivation, these include: poisoning, mechanical straining, leaching, coking and phases changes (shown in Figure 1.6), as well as, changes in size and shape, from a process called *sintering*.⁶⁰ *Poisoning* take place when species are irrevocably adsorbed onto the catalyst surface preventing other species from adsorbing to undergo surface reactions. *Mechanical strain* can cause changes in the shapes and size of the active site through attrition. This can commonly occur in reactors or from thermal stress, from temperature fluctuations in the catalyst preparation and during a reaction. *Leaching* is the loss of the active metal species from the catalyst into liquid phase reaction medium, which results in a lower number of atoms available to make up active sites. *Coking* is the deposition of carbon residues that results in the blocking of active sites. If reactants are limited in the number of active sites than they can reach, then catalyst performance suffers. Additionally, catalyst deactivation can also come about from *phase changes*, for instance the oxidation of metals by the solvent or oxygen present in the reaction to form catalytic inactive oxides of the metal species. The mostly relevant deactivation process to this thesis (sintering) is described in much more detail below, in its own section.



Figure 1.6: Schematic representation of supported catalyst deactivation processes

A typical catalyst cycle (that is the time scale it operates for) differs substantially, for example, zeolite catalysts used in fluid catalytic cracking have a life cycle of only a few seconds, while the iron catalyst used in the Haber process can last for several years.⁵⁸ There are many methods used to prevent the process of deactivation, and extend catalytic lifetime. Prevention is often achieved by the control of operational parameters and by the design of industrial plants.^{57,61} For instance, in the case of the Fischer-Tropsch synthesis, a multi-stage

process is employed along with reactor designs that control the temperature increases that can occur in individual reactors and prevent the thermal degradation of catalysts.⁶² Pre-purification of feedstocks is also performed along with the employment of “guard beds” to prevent the poisoning of the catalyst by impurities such as sulfur.⁶³

Unfortunately, preventative measures are only effective temporarily. Eventually catalyst deactivation is inevitable and the catalyst will need to be replaced. As described, often the metals used as the active phase in heterogeneous catalysts are valuable transition metals, therefore having to replace the catalyst leads to significant costs. Accumulated costs are not only associated with the replacement catalyst, but also due to the cost of undergoing the replacement. The process that uses the catalyst often must be shut down in order to ensure safe replacement, this is otherwise known as “down time” and can cost the companies millions.⁵⁹ Depending on the reaction process, they may also be technical aspects to replacing it, i.e. removal of certain machinery or requirement of specialists.

There are occasions where catalyst deactivation can be reversed. In these cases, costs may still arise from the process used in the “regeneration”. In the case of the zeolites used in fluid catalytic cracking, which have a very short catalytic cycle due to rapid coking, constant regeneration occurs via combustion of the coke at high temperature (~700°C), to help extend the lifetime of the catalyst. This involves the cost of the temporary removal of the catalyst into a regenerator and the application of high temperatures.⁶⁴ Therefore, consideration needs to be made to the financial impact of using catalysts, where possible corporations try to find efficient catalysts that use cheaper materials and have longer life cycles.

Sintering

One of the most common processes that lead to catalyst deactivation, and the one most relevant to the work presented, is *sintering*,^{65,66} which causes changes in the NP's size and shape. This phenomenon is driven by the thermodynamic desire to form larger nanoparticles, (described in the Growth section of this chapter) where atoms and small supported clusters aggregate to form a larger one, increasing the volume and decreasing the surface area. Sintering also encompasses changes to the support under thermal treatment but this aspect falls out of the scope of the present work. Sintering can cause a reduction in the specific metal surface area, leading to a decrease in the proportion of edges and corner sites. This reduces the number of available active sites, and thus, bring about the reduction of catalytic performance and eventual deactivation of the catalyst. There are many factors that contribute to sintering, both in catalyst preparation and during catalyst operation, these

include, temperature, gas environment, type of metal, type of support and promoters added.⁶⁵ The lack of understanding in the models and existence of methods for inhibiting ripening is a serious drawback in the creation of long-term stable catalysts. Additionally, more kinetic data pertaining to dispersion and particle size distribution is required to both develop and validate accurate sintering models under specific reaction conditions.⁵⁹

It is well-known that sintering processes are accelerated at high temperatures.^{65,67} For example, quantitative evidence of sintering is described in a paper by Parker *et al.*⁶⁸ using Au/TiO₂ catalysts, where the Au area reduced from 0.25 monolayers (ML) to 0.18 ML when temperature was increased from 300 K to 900 K. The increase in cluster size with higher temperatures, can be explained by higher diffusion, migration and detachment rates from the increased thermal energy. The higher temperatures increase the likelihood of bond breaking in the system and the mobility of the metal species, causing faster agglomeration. This is because a metal's resistance to sintering is closely linked to its melting point. Metals with a lower melting point will become molten and more mobile at lower temperatures, hence, reaction and preparation temperatures will have a greater effect on these metals and more sintering will occur. It is also important to note that the melting temperature of metals is size dependant,^{69,70} and nano-sized particles will have significantly reduced melting points, e.g. bulk gold has a melting point of 1094 °C, while for a 2 nm Au particle this decreases to around 400 °C.⁷¹ However, the relationship between melting point and stability is not always so clear. For example, the incorporation of an additional metal, such as Cu into Au metal catalysts have been seen to reduce sintering rates. The catalyst activity for Au-Cu/SiO₂ catalyst toward CO oxidation was comparable to monometallic Au/SiO₂ catalysts, but the addition of Cu into the NP increases its stability and provided sintering resistance.^{13,72} A similar effect has been described by Liu *et al.*, with Ag as the secondary metal.⁷³ Therefore, while Au-Cu and Au-Ag alloys have a lower melting points than monometallic Au,⁷⁴ clearly there are other considerations in these supported systems that add stability to the clusters.

Unfortunately, in catalysed reactions, high temperatures are often used, for various thermodynamic and kinetic reasons, adding difficulty when using catalysts in industry.⁵⁹ For example, changes to the catalyst surface, such as agglomeration of the metal species, is seen with the catalysts used for ammonia synthesis (performed at 450 - 550 °C) and methanol synthesis (200 - 300 °C),² decreasing the lifetime of the catalyst.

Regarding the influence of gas atmosphere on sintering processes, an oxygen atmosphere has been seen to influence the rates of sintering with Au catalysts.⁷⁵ In an ultra-high vacuum

(UHV), an Au/TiO₂ system had stable particle sizes up to 500 °C. In the same system, under an O₂ atmosphere, particle sizes are seen to increase after annealing at 400 °C, while in an air atmosphere particle growth was seen at room temperature according to work by Kielbassa *et al.*⁷⁶

Additionally, the presence of adsorbents on the surface influences sintering rates. For example, the presence of a strong adsorbate can induce weaker metal-metal bonds in the nanoparticle structure. This leads to detachment of metal atoms, progressing sintering processes, as described in research by Ouyang *et al.*⁶⁶ and Kolmakov *et al.*⁷⁷ regarding Au nanoparticles on TiO₂. Furthermore, according to Brown *et al.*⁷⁸ at 650 K, single Au atoms on a hydroxylated MgO surface are prevented from binding to favourable sites by the presence of the surface OH groups, thus diffusion is increased, resulting in atom agglomeration.

Supporting the metal will almost certainly increase its resistance to sintering. However, the level of interaction between the cluster and the support, and therefore, the degree of protection the support offers from sintering, is dependent on its nature and the synergy that metal has with the chosen support.⁷⁰ Altering catalyst supports to prevent sintering has also been explored, for example, a combination of TiO₂ and hydroxyapatite has been used to support Au NP's. The increased stability of NP's is reportedly due to partial encapsulation of the NP's through strong metal support interactions.⁷⁹ Similarly, 4-6 nm sized nanoparticles were stabilized by a perovskite support, up to temperatures of 700 °C.⁸⁰ Greater metal-support interactions mean stronger adsorption energies (E_{ads}). This gives support to the conclusion that increased E_{ads} reduces sintering processes.

Through the observation of the factors that influence sintering processes, the methods of finding ways to slow down and/or reverse sintering processes are highlighted. While taming reaction conditions, e.g. using lower reaction temperature and pressures of reacting mediums, may help to reduce the rates of sintering, these changes may not be conducive to the optimum catalyst performance. Therefore, more resilient catalysts are being created using a range of methodologies.

For instance, there have been attempts at "anchoring" Au NP's rather than conventionally supporting them. This has been attempted using SiO₂ shells to isolate metal nanoparticles and prevent sintering,⁸¹ and also by embedding Au particles in zeolites.⁸²

An alternative idea is to reverse the effects of sintering through digestion of the larger nanoparticles back to smaller ones. An example of a method for reversing sintering for Pt

catalysts is described in a review by Bartholomew.⁶⁵ The “redispersion” technique involves high temperature treatment with O₂ and Cl₂. And has seen the dispersion (D) of the metal increase. Essentially, the ‘oxychlorination’ induces the formation of volatile metal oxides and metal chlorides on the catalyst surface, which stick to the support and decompose into small metal crystallites before being reduced. Another example of the redispersion of sintered catalysts is described for Au/oxide systems with CH₃-I/Ar treatments by Sá *et al.*⁸³ The proposed reaction mechanism is that gold is initially oxidised by interaction with iodine, followed by the dissociation the Au–I bond formed. The largest difference being made to the Au/Al₂O₃ system where Au NP’s were reduced from 1 – 3 nm to < 1 nm in size.

[Experimental techniques for observing sintering processes.](#)

The observation of changes to the size and shape of supported NPs is extremely important to the production of resilient heterogeneous catalysts. Changes to the catalyst surface through sintering processes are common during harsh reaction conditions and after preparation methods. In reusability tests, the catalyst will be assessed for its resilience to change by undergoing typical reaction conditions several times. These tests give an indication of how reusable the catalyst is, which relates to its economic viability in industrial applications. Between these tests, the following techniques may be used to analyse changes to catalyst surface to explain any alteration in catalyst activity.

Selective chemisorption can be used to determine catalyst dispersion, as long as significant interaction of the adsorbed gas with the metal surface occurs and if the stoichiometry of the adsorption is known. Typical gases used in chemisorption are H₂ and CO. However, with Au catalysts, both CO and H₂ bind too weakly.⁸⁴ Therefore, these prerequisites are not met for Au systems⁸⁵ and chemisorption is not an appropriate method for determining Au sites.

X-ray diffraction (XRD) techniques are also often used to determine particle size.⁸⁶ However, they can be of little use for catalysts with very small nanoparticles. Particle size measurements which apply the Scherrer equation, i.e. XRD, are unreliable at these sizes due to the presence of broad peaks and statistical averaging. The smaller the nanoparticle size, the broader the peaks and the lower the intensities,^{84,87} this effect is seen from below 200 nm. Therefore, for sub-nanometre cluster sizes, the technique is not sensitive enough to discern anything except huge changes to the system.

Electron microscopy techniques offer a more successful solution to measuring supported small metal cluster systems. These techniques include: transmission electron microscopy (TEM), in which a beam of electrons is transmitted through a sample to form an image and

Scanning transmission electron microscopy (STEM), which works in the same way but with the added ability to scan across the surface to make images. The key to them being used successfully with clusters as small as Au_n/MgO ($n = 1-19$), is a high resolution. High resolution TEM (HRTEM) can image sub-nanometre clusters, allowing the study of materials at the atomic scale.^{38,88-90} Additionally, the “in-situ” methods allow observation of the catalyst surface in real time, giving added information about sintering in specific time frames.

Nanoparticle morphology

Nanoparticles may also undergo processes that change its shape, where atoms of a nanoparticle rearrange away from the original structure. The NP shape is influenced by many of the same factors such that influence size, including temperature and gas environments that affect the distribution of energy within the system, i.e. the strength and arrangement of bonds holding the NP's and the support together. On nucleation and subsequent growth of unsupported particles, the rearrangement and resulting equilibrium shapes are directly related to the surface energy, this is described by the Gibbs-Wulff theorem.⁹¹

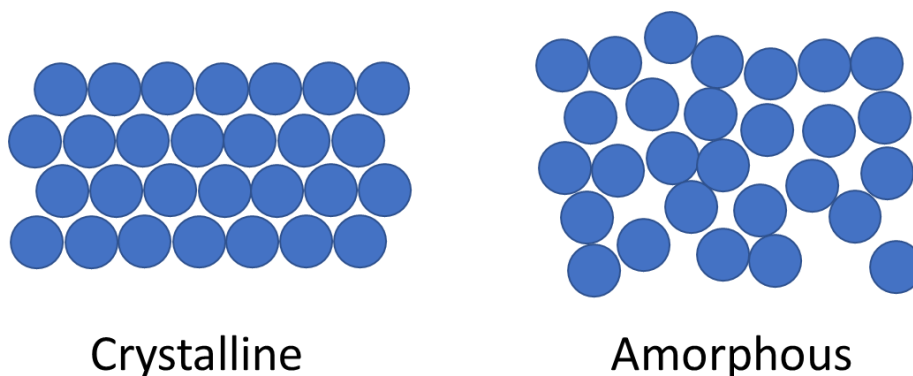


Figure 1.7: Scheme to show the regular arrangement of atoms in a crystalline solid in comparison to the irregularly arranged atoms found in an amorphous solid.

The Gibbs - Wulff theorem suggests that a particle will adopt the shape with the lowest total surface energy. Therefore, the facets with the lowest surface energy will dominant the shape, unless the NP formation is kinetically controlled.⁹² The shape of the NP is constructed in the following way: Starting from the nucleation point, a plane is drawn normal to a vector with a magnitude proportional to the surface energy required to create the surface along that plane. The greater the surface energy, the further away the facets are expressed from the nanoparticle nucleation point. The facet appearance is derived from the fact that in crystalline solids (see Figure 1.7) the surface energy is anisotropic i.e. the properties of the structure change in different directions. The nearest facet (the one with the lowest surface energy) then dictates the shape of the resultant nanoparticle, see Figure 1.8.

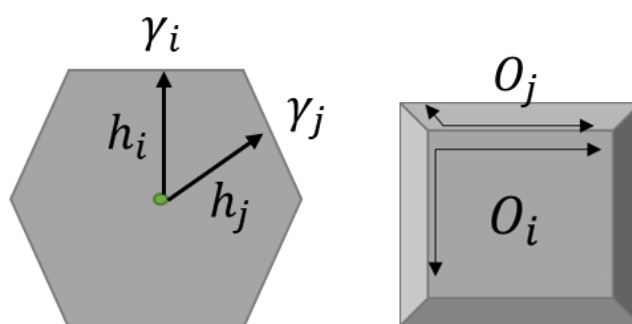


Figure 1.8: Diagram showing the parameters of the Wulff construction, side view (left) and top view (right). The green dot shows the nucleation point. h_i and h_j are the vectors to facets with surface energy γ_i and γ_j respectively. O_i and O_j are the facets created with surface energy γ_i and γ_j .

Even when the nanoparticles are synthesised in a way to minimise their size or to give them a particular shape, subsequent treatments, either in pre-treatment or during reaction, can alter their shape and size returning them to thermodynamic equilibrium, kinetics permitting.

In the production of anisotropic transition metal nanoparticles, such as, Au, Pt and Ag. The energy-minimizing shape is obtained by enclosing the crystal with the facets of the lowest possible surface energy (γ) as well as truncating the facets in order to give minimum possible surface area for a given volume, which results in a polyhedron shape. For example, a face centred cubic (fcc) crystal structure, such as Au, possesses surface energies of the low-index crystallographic facets in the order $\gamma(111) < \gamma(100) < \gamma(110)$.⁹³ Based on these facet energies, minimum surface-energy requirement predict that the seed crystals of fcc metals should

show a tendency to adopt a tetrahedral or an octahedral shape enclosed by $\{111\}$ facets, see Figure 1.9.⁹⁴

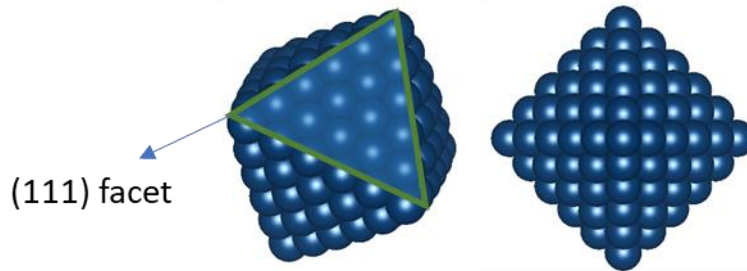


Figure 1.9: Octahedral crystal shape, (left) angled side and (right) top view. Displaying the $\{111\}$ facets.

However, for some sizes, tetrahedron or octahedron shapes are not the minimum surface area shapes for a given volume, the Gibbs–Wulff shape for an fcc crystal structure is a truncated octahedron, e.g. a cuboctahedron, which is enclosed by eight hexagonal $\{111\}$ facets and six square $\{100\}$ facets. Truncation introduces a relatively high-energy $\{100\}$ facet but generates nearly spherical shape, thereby decreasing the total surface area and free energy, by reducing to surface/volume ratio, see Figure 1.10.⁹⁵

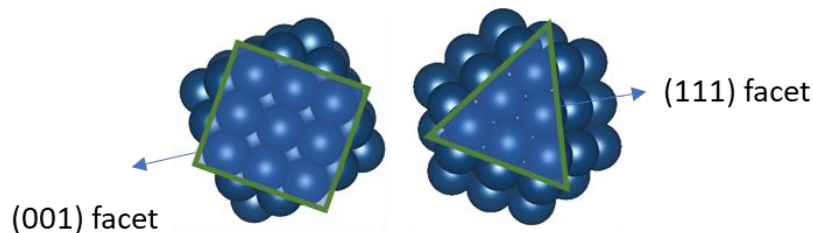


Figure 1.10: Cuboctahedron crystal shape, (left) angled side and (right) top view. Displaying the $\{001\}$ and $\{111\}$ facets

However, the accuracy of Wulff's theorem for describing the shape of nanoparticles in some systems has been put under scrutiny. For instance, it is noted that Au particles, as well as other fcc metals, have been seen under electron microscopy imaging to take on some unexpected shapes, such as icosahedral and decahedral structures.⁹⁶ These were termed multiply twinned particles (MTP's).⁹⁷ The result of this observation was a new variant of the Wulff construction called the *modified Wulff construction*,⁹⁷ which has the inclusion of a "twin facet" energy to take into account the existent of twin boundaries.

In terms of the kinetic growth of particles, the surface-energy factor continues to play a major role in determining the shapes of particles as they grow. For example, terrace faces of closely packed transition metals grow more slowly than stepped faces or kinked faces with high surface energy (γ). Thus, in a growing crystal, flat facets will be exposed more and more,

while stepped faces and kinked faces will gradually disappear. This results in a shrinkage in area (or elimination) of higher-energy facets, while the area of lower-energy facets increases. The effect of growth kinetics on cluster shape is taken into account by the *kinetic modified Wulff construction* by the inclusion of growth velocities and includes growth enhancement at favoured nucleation sites.⁹⁷

As for particles of nanometre dimensions, a significant proportion, if not all the atoms, have varying coordination numbers increasing the complexity of the shape to beyond what is predictable by the Wulff construction. It is suggested that the theorems can only be applied if size effects and surface defects, like edges and corner sites, do not contribute significantly to the surface energy, such as would be the case for the cluster size used in the Au_n/MgO system described.^{97,98}

Moreover, the low number of atoms in the Au_n/MgO systems ($n < 20$ atoms) used in this thesis prohibits the formation of regular terraces of any real size and limits the applicability the Wulff models. Additionally, the regular polyhedron shapes can be obtained only at 0 K, when the growth is purely thermodynamically controlled. Temperature has a significant influence on anisotropy and should be considered, i.e. as temperature increases, surface-energy anisotropy decreases, and the equilibrium shape rounds off.

Supported nanoparticles

Additionally, lattice mismatch and strain from the addition of a support to the system contributes to overall surface energy, and therefore the stability of the system. The addition of a support is therefore an additional consideration to the equilibrium shape of the nanoparticles. This has been taken into account by a modification of the Wulff construction by Winterbottom⁹⁹ and applied to supported particles. Essentially, the Wulff construction predicted shapes are truncated at a plane and depth that depend on the crystals' orientation and the relative surface energies. To consider the influence of a metal-support interface on the surface energy of the particle, there is an additional free energy term associated with adsorption of the particle to the support γ_{ads} (per nanoparticle atom at the interface). This is combined with the surface free energy of the metal particle, γ_i to produce the interfacial

surface energy γ_{int} , as seen in Figure 1.11 The interfacial surface energy is used instead of the exposed metal surface energy when summing the total surface energy of the particle.

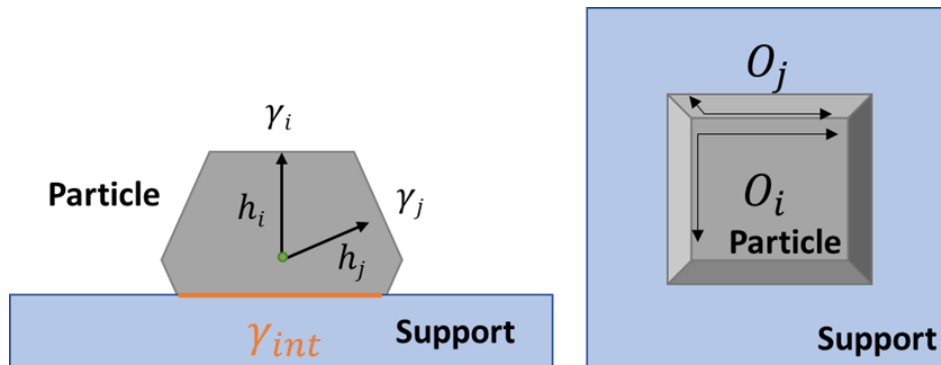


Figure 1.11: Schematic illustrating the Winterbottom amendments to the Wulff construction for supported nanoparticles. γ_{int} replaces γ_i for the metal-support interface by the addition of the free energy of adsorption per interface atom (γ_{ads}).

γ_{int} is related to surface “wetting” by its relation to γ_i , if the surface energy at the interface (γ_{int}) is much smaller than the surface energy of the cluster (γ_i) the cluster wets the support. If the surface energies of γ_{int} and γ_i compete then the cluster wetting is reduced. If interface surface energy is the same as the cluster surface energy, then “de-wetting” occurs.

The stronger the adsorption energy, the lower the interface surface energy (γ_{int}), which leads to a greater degree of wetting. An example of this is displayed in Chapter 3, where a greater ratio of the metal adsorption energy to the bulk cohesive energy of the metal cluster (E_{ads}/E_{coh}) has been shown to produce 2D NP structures over 3D ones.^{100,101}

Lattice mismatch occurs when the structure of the cluster and metal-metal bond distances are different to that of the support, see Figure 1.12.¹⁰² This is also a factor that effects the interaction of the cluster with the support. Lattice mismatch can cause interfacial strain, which can have an influence throughout the whole of the metal particle. The degree of this mismatch can be important to the shape of the resulting particle. If the mismatch is small, the strain within the cluster may be minimal and the structure favoured by the nanoparticle retained. At larger mismatches, the cluster may not be able to accommodate the strain, and so will deform. It should also be noted that mismatch is not only a function of bond lengths but also of the symmetry of the cluster and the support. This is discussed further in Chapter 5.

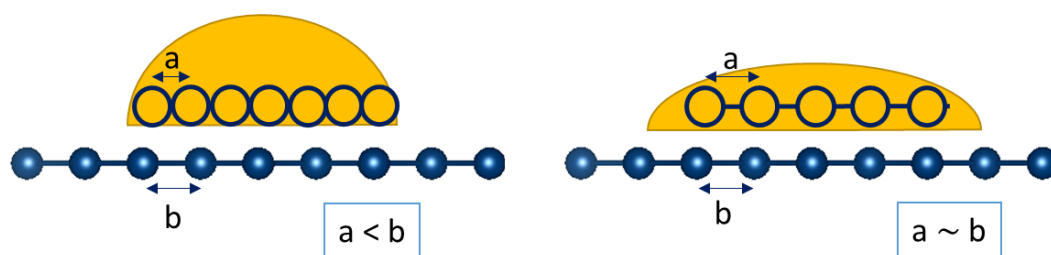


Figure 1.12: Illustration of mismatch in a supported nanoparticle system, where a is the bond distance between cluster atoms and b is the bond distance between favourable adsorption sites of the support.

This chapter serves to validate as well as introduce the research performed in this thesis. In the following chapters the supported metal catalyst Au_n/MgO is modelled, and the stability and growth of the Au_n clusters is analysed using a range of computational methods. By exploring the current capabilities and limitations of the computational methods described, it is endeavoured that they can be used successfully, and in conjunction with experimental methods, in the understanding of the processes that lead to changes in size of shape of active metal nanoparticles.

References

1. Wacławek, S., Padil, V. V. T. & Černík, M. Major Advances and Challenges in Heterogeneous Catalysis for Environmental Applications: A Review. *Ecol. Chem. Eng. S* **25**, 9–34 (2018).
2. Hagen, J. *Industrial catalysis : a practical approach*. (Weinheim : Wiley-VCH, 2006).
3. Mostafa, S. *et al.* Shape-Dependent Catalytic Properties of Pt Nanoparticles. *J. Am. Chem. Soc.* **132**, 15714–15719 (2010).
4. Wang, Y. *et al.* Shape-controlled synthesis of Pt particles and their catalytic performances in the n-hexadecane hydroconversion. *Catal. Today* **259**, 331–339 (2016).
5. Berg, R. van den *et al.* Structure sensitivity of Cu and CuZn catalysts relevant to industrial methanol synthesis. *Nat. Commun.* **7**, 20457–20465 (2016).
6. Haruta, M. Size-and support-dependency in the catalysis of gold. *Catal. Today* **36**, 153–166 (1997).
7. Fu, Q., Weber, A. & Flytzani-Stephanopoulos, M. Nanostructured Au–CeO₂ catalysts for low-temperature water–gas shift. *Catal. Letters* **77**, (2001).
8. Cheng, J. & Hu, P. Utilization of the Three-Dimensional Volcano Surface To Understand the Chemistry of Multiphase Systems in Heterogeneous Catalysis. *J. Am. Chem. Soc.* **130**, 10868–10869 (2008).
9. Medford, A. J. *et al.* From the Sabatier principle to a predictive theory of transition-metal heterogeneous catalysis. *J. Catal.* **328**, 36–42 (2015).
10. Oudar, J. & Wise, H. *Deactivation and poisoning of catalysts*. (M. Dekker, 1985).
11. Roldán, A. & Ricart, J. M. Origin of the size dependence of Au nanoparticles toward molecular oxygen dissociation. *Theor Chem Acc.* **128**, 675–681 (2011).
12. James T. Nurmi *et al.* Characterization and Properties of Metallic Iron Nanoparticles: Spectroscopy, Electrochemistry, and Kinetics. *Environ. Sci. Technol.* **39**, 1221–1230 (2005).
13. Li, W., Wang, A., Liu, X. & Zhang, T. Silica-supported Au-Cu alloy nanoparticles as an efficient catalyst for selective oxidation of alcohols. *Applied Catal. A, Gen.* **433–434**, 146–151 (2012).

14. Janaina F. Gomes, Demetrius Profeti, and L. J. D. Influence of the Particle Size Distribution on the Activity and Selectivity of Carbon-Supported Platinum Nanoparticle Catalysts for Ethanol Electrooxidation. *CHEMELECTROCHEM* **1**, 655–662 (2014).
15. Bhattacharjee, S., Dotzauer, D. M. & Bruening, M. L. Selectivity as a Function of Nanoparticle Size in the Catalytic Hydrogenation of Unsaturated Alcohols. *J. Am. Chem. Soc.* 3601–3610 (2009) doi:10.1021/ja807415k.
16. Daniel, M.-C. & Astruc, D. Gold nanoparticles: assembly, supramolecular chemistry, quantum-size-related properties, and applications toward biology, catalysis, and nanotechnology. *Chem. Rev.* **104**, 293–346 (2004).
17. Hammer, B. & Nørskov, J. K. Theoretical Surface Science and Catalysis—Calculations and Concepts. in *Advances in Catalysis: Impact of Surface Science on Catalysis* 71–126 (2001).
18. Li, L., Abild-Pedersen, F., Greeley, J. & Nørskov, J. K. Surface Tension Effects on the Reactivity of Metal Nanoparticles. *J. Phys. Chem. Lett.* **6**, 3797–3801 (2015).
19. Henry, C. R. Catalytic activity of supported nanometer-sized metal clusters. *Appl. Surf. Sci.* **164**, 252–259 (2000).
20. Michele L. Anderson, †, Catherine A. Morris, †, Rhonda M. Stroud, ‡, Celia I. Merzbacher, A. & Debra R. Rolison*, †. Colloidal Gold Aerogels: Preparation, Properties, and Characterization. *Langmuir* **15**, 674–681 (1999).
21. Kattan, P. *Ratio of Surface Area to Volume in Nanotechnology and Nanoscience*. (Petra books, 2011).
22. Uglov, V. V., Doroshevich, I. L., Kvasov, N. T., Remnev, G. E. & Shymanski, V. I. On physical properties of nanoparticles: size effect and scale of nanoobjects. *Phys. status solidi* **13**, 903–907 (2016).
23. Yim, W.-L. *et al.* Universal Phenomena of CO Adsorption on Gold Surfaces with Low-Coordinated Sites. *J. Phys. Chem. C* **111**, 445–451 (2007).
24. Ye, X. & Mavrikakis*, M. Adsorption and Dissociation of O₂ on Gold Surfaces: Effect of Steps and Strain. *J. Phys. Chem. B* **107**, 9298–9307 (2003).
25. Mandić, M., Todić, B., Živanić, L., Nikačević, N. & Bukur, D. B. Effects of Catalyst

- Activity, Particle Size and Shape, and Process Conditions on Catalyst Effectiveness and Methane Selectivity for Fischer–Tropsch Reaction: A Modeling Study. *Ind. Eng. Chem. Res.* **56**, 2733–2745 (2017).
26. Janssens, T. V. W., Carlsson, A., Puig-Molina, A. & Clausen, B. S. Relation between nanoscale Au particle structure and activity for CO oxidation on supported gold catalysts. *J. Catal.* **240**, 108–113 (2006).
 27. Parab, H. J., Jung, C., Lee, J.-H. & Park, H. G. A gold nanorod-based optical DNA biosensor for the diagnosis of pathogens. *Biosens. Bioelectron.* **26**, 667–673 (2010).
 28. Wuithschick, M. *et al.* Size-Controlled Synthesis of Colloidal Silver Nanoparticles Based on Mechanistic Understanding. *Chem. Mater.* **25**, 4679–4689 (2013).
 29. Kosmulski, M. *Surface Charging and Points of Zero Charge*. (CRC Press, 2009).
 30. Herizchi, R., Abbasi, E., Milani, M. & Akbarzadeh, A. Current methods for synthesis of gold nanoparticles. *Artif. Cells, Nanomedicine, Biotechnol.* **44**, 596–602 (2016).
 31. Regalbuto, J. *Catalyst Preparation: Science and Engineering*. (CRC Press, 2016).
 32. Perego, C. & Villa, P. Catalyst preparation methods. *Catal. Today* **34**, 281–305 (1997).
 33. Santos, V. P. *et al.* Oxidation of CO, ethanol and toluene over TiO₂ supported noble metal catalysts. *Appl. Catal. B Environ.* **99**, 198–205 (2010).
 34. Blick, K. *et al.* Methane oxidation using Au/MgO catalysts. *Catal. Letters* **50**, 211–218 (1998).
 35. Alshammari, A. S. Heterogeneous Gold Catalysis: From Discovery to Applications. *Catalysts* **9**, 402 (2019).
 36. Prati, L. & Villa, A. *Gold Catalysis: Preparation, Characterization, and Applications*. (Jenny Stanford Publishing, 2016).
 37. Bowker, M., Nuhu, A. & Soares, J. High activity supported gold catalysts by incipient wetness impregnation. *Catal. Today* **122**, 245–247 (2007).
 38. Carabineiro, S. A. *et al.* Gold nanoparticles supported on magnesium oxide for CO oxidation. *Nanoscale Res. Lett.* **6**, 435 (2011).
 39. Demirel-Gülen, S., Lucas, M. & Claus, P. Liquid phase oxidation of glycerol over

- carbon supported gold catalysts. *Catal. Today* **102–103**, 166–172 (2005).
40. Gaiassi, A. & Prati, L. Gold catalysts for the direct oxidation of aminoalcohols to aminoacids. *Catal. Today* **141**, 378–384 (2009).
 41. Bogdanchikova, N. *et al.* More Insights into Support and Preparation Method Effects in Gold Catalyzed Glycerol Oxidation. *Curr. Org. Synth.* **14**, 377–382 (2017).
 42. Schubert, M. M. *et al.* CO Oxidation over Supported Gold Catalysts—“Inert” and “Active” Support Materials and Their Role for the Oxygen Supply during Reaction. *J. Catal.* **197**, 113–122 (2001).
 43. Han, Y., Ferrando, R. & Li, Z. Y. Atomic Details of Interfacial Interaction in Gold Nanoparticles Supported on MgO(001). *J. Phys. Chem. Lett.* **5**, 131–137 (2014).
 44. Barnard, A. S., Young, N. P., Kirkland, A. I., van Huis, M. A. & Xu, H. Nanogold: A Quantitative Phase Map. *ACS Nano* **3**, 1431–1436 (2009).
 45. Barnard, A. S. Modelling of nanoparticles : approaches to morphology and evolution. *Rep. Prog. Phys.* **73**, 86502–52 (2010).
 46. Baerns, M. *Basic principles in applied catalysis: Preface. Springer Series in Chemical Physics* vol. 75 (Springer, 2004).
 47. Narula, G. K., Narula, K. S. & Gupta, V. K. *Materials Science*. (Tata McGraw-Hill, 1989).
 48. Vitto, A. Del, Pacchioni, G., Delbecq, F. & Sautet, P. Au Atoms and Dimers on the MgO(100) Surface: A DFT Study of Nucleation at Defects. *J. Phys. Chem. B* **109**, 8040–8048 (2005).
 49. Wallace, W. T., Min, B. K. & Goodman, D. W. The nucleation, growth, and stability of oxide-supported metal clusters. *Top. Catal.* **34**, 17–30 (2005).
 50. Wahlström, E. *et al.* Bonding of Gold Nanoclusters to Oxygen Vacancies on Rutile. *Phys. Rev. Lett.* **90**, 4 (2003).
 51. Sanchez, A. *et al.* When Gold Is Not Noble: Nanoscale Gold Catalysts. *J. Phys. Chem. A* **103**, 9573–9578 (1999).
 52. Häkkinen, H., Abbet, S., Sanchez, A., Heiz, U. & Landman, U. Structural, Electronic, and Impurity-Doping Effects in Nanoscale Chemistry: Supported Gold Nanoclusters.

- Angew. Chemie Int. Ed.* **42**, 1297–1300 (2003).
53. Barcaro, G., Fortunelli, A., Nita, F. & Ferrando, R. Diffusion of Palladium Clusters on Magnesium Oxide. *Phys. Rev. Lett.* **95**, 246103 (2005).
54. Dai, Y., Lu, P., Cao, Z., Campbell, C. T. & Xia, Y. The physical chemistry and materials science behind sinter-resistant catalysts. *Chemical Society Reviews* vol. 47 4314–4331 (2018).
55. Campbell, C. T., Parker, S. C. & Starr, D. E. The effect of size-dependent nanoparticle energetics on catalyst sintering. *Science* **298**, 811–4 (2002).
56. Chorkendorff, I. (Ib) & Niemantsverdriet, J. W. *Concepts of modern catalysis and kinetics*. (Wiley-VCH, 2007).
57. Bartholomew, C H. and Argyle, M. D. *Advances in Catalyst Deactivation. Advances in Catalyst Deactivation* (MDPI AG - Multidisciplinary Digital Publishing Institute, 2018). doi:10.3390/books978-3-03842-188-7.
58. Moulijn, J. ., van Diepen, A. . & Kapteijn, F. Catalyst deactivation: is it predictable?: What to do? *Appl. Catal. A Gen.* **212**, 3–16 (2001).
59. Argyle, M. D. & Bartholomew, C. H. Heterogeneous Catalyst Deactivation and Regeneration: A Review. *Catalysts* **5**, 145–269 (2015).
60. Mebrahtu, C., Krebs, F., Abate, S., Centi, G. & Palkovits, R. CO₂ Methanation: Principles and Challenges. *Stud. Surf. Sci. Catal.* **178**, 85–103 (2019).
61. Hammond, C. Intensification studies of heterogeneous catalysts: probing and overcoming catalyst deactivation during liquid phase operation. *Green Chem.* **19**, 2711–2728 (2017).
62. Speight, J. G. & Speight, J. G. The Fischer–Tropsch Process. in *Gasification of Unconventional Feedstocks* 118–134 (Gulf Professional Publishing, 2014). doi:10.1016/B978-0-12-799911-1.00005-4.
63. Tsakoumis, N. E., Rønning, M., Borg, Ø., Rytter, E. & Holmen, A. Deactivation of cobalt based Fischer–Tropsch catalysts: A review. *Catal. Today* **154**, 162–182 (2010).
64. Almas, Q. *et al.* Transformations of FCC catalysts and carbonaceous deposits during repeated reaction-regeneration cycles. *Catal. Sci. Technol.* **9**, 6977–6992 (2019).

65. Bartholomew, C. H. Mechanisms of catalyst deactivation. *Appl. Catal. A Gen.* **212**, 17–60 (2001).
66. Ouyang, R., Liu, J.-X. & Li, W.-X. Atomistic Theory of Ostwald Ripening and Disintegration of Supported Metal Particles under Reaction Conditions. *J. Am. Chem. Soc.* **135**, 1760–1771 (2013).
67. Fendler, J. H. & Wiley InterScience (Online service). *Nanoparticles and nanostructured films : preparation, characterization and applications*. (Wiley-VCH, 1998).
68. Parker, S. C. & Campbell, C. T. Reactivity and sintering kinetics of Au/TiO₂(110) model catalysts: Particle size effects. *Top. Catal.* **44**, 3–13 (2007).
69. Campbell, C. T. & Sellers, J. R. V. Anchored metal nanoparticles: Effects of support and size on their energy, sintering resistance and reactivity. *Faraday Discuss.* **162**, 9 (2013).
70. Buffat, P. & Borel, J.-P. Size effect on the melting temperature of gold particles. *Phys. Rev. A* **13**, 2287–2298 (1976).
71. Hugon, A., Kolli, N. El & Louis, C. Advances in the preparation of supported gold catalysts: Mechanism of deposition, simplification of the procedures and relevance of the elimination of chlorine. *J. Catal.* **274**, 239–250 (2010).
72. Liu, X., Wang, A., Zhang, T., Su, D.-S. & Mou, C.-Y. Au–Cu alloy nanoparticles supported on silica gel as catalyst for CO oxidation: Effects of Au/Cu ratios. *Catal. Today* **160**, 99–104 (2011).
73. Liu, X. *et al.* Synthesis of Thermally Stable and Highly Active Bimetallic Au–Ag Nanoparticles on Inert Supports. *Chem. Mater.* **21**, 410–418 (2009).
74. Guisbiers, G. *et al.* Electrum, the Gold-Silver Alloy, from the Bulk Scale to the Nanoscale: Synthesis, Properties, and Segregation Rules. *ACS Nano* **10**, 188–98 (2016).
75. S. Kielbassa, M. Kinne, A. & Behm*, R. J. Thermal Stability of Au Nanoparticles in O₂ and Air on Fully Oxidized TiO₂(110) Substrates at Elevated Pressures. An AFM/XPS Study of Au/TiO₂ Model Systems. *J. Phys. Chem. B* **108**, 19184–19190 (2004).
76. Bartholomew, C. H. & Sorensen, W. L. Sintering kinetics of silica- and alumina-

- supported nickel in hydrogen atmosphere. *J. Catal.* **81**, 131–141 (1983).
77. Kolmakov, A. & Goodman, D. W. Imaging gold clusters on TiO₂ (110) at elevated pressures and temperatures. *Catal. Letters* **70**, 93–97 (2000).
78. Brown, M. A., Carrasco, E., Sterrer, M. & Freund, H.-J. Enhanced Stability of Gold Clusters Supported on Hydroxylated MgO(001) Surfaces. *J. Am. Chem. Soc.* **132**, 4064–4065 (2010).
79. Tang, H. *et al.* Ultrastable Hydroxyapatite/Titanium-Dioxide-Supported Gold Nanocatalyst with Strong Metal-Support Interaction for Carbon Monoxide Oxidation. *Angew. Chemie Int. Ed.* **55**, 10606–10611 (2016).
80. Tian, C. *et al.* Toward the Design of a Hierarchical Perovskite Support: Ultra-Sintering-Resistant Gold Nanocatalysts for CO Oxidation. *ACS Catal.* **7**, 3388–3393 (2017).
81. Jia, C.-J. & Schüth, F. Colloidal metal nanoparticles as a component of designed catalyst. *Phys. Chem. Chem. Phys.* **13**, 2457 (2011).
82. Laursen, A. B. *et al.* Substrate Size-Selective Catalysis with Zeolite-Encapsulated Gold Nanoparticles. *Angew. Chemie Int. Ed.* **49**, 3504–3507 (2010).
83. Sá, J. *et al.* Redispersion of Gold Supported on Oxides. *ACS Catal.* **2**, 552–560 (2012).
84. Villa, A. *et al.* Characterisation of gold catalysts. *Chem. Soc. Rev.* **45**, 4953–4994 (2016).
85. Choudhary, T. V. & Goodman, D. W. Catalytically active gold: The role of cluster morphology. *Appl. Catal. A Gen.* **291**, 32–36 (2005).
86. Pecharsky, V. K. & Zavalij, P. Y. *Fundamentals of powder diffraction and structural characterization of materials.* (Springer, 2009).
87. Bunaciu, A. A., Udriștioiu, E. gabriela & Aboul-Enein, H. Y. X-Ray Diffraction: Instrumentation and Applications. *Crit. Rev. Anal. Chem.* **45**, 289–299 (2015).
88. Wang, H. *et al.* Atomically dispersed Au catalysts supported on CeO₂ foam: controllable synthesis and CO oxidation reaction mechanism. *Nanoscale* **9**, 16817–16825 (2017).
89. Duan, X. *et al.* Size controllable redispersion of sintered Au nanoparticles by using

- iodohydrocarbon and its implications. *Chem. Sci.* **7**, 3181–3187 (2016).
90. Wang, T., Yuan, X., Li, S., Zeng, L. & Long, J. CeO₂-Modified Au@SBA-15 Nanocatalysts for Liquid-phase Selective Oxidation of Benzyl Alcohol. *Nanoscale* **7**, (2015).
91. Wulff, G. On the question of speed of growth and dissolution of crystal surfaces. - Cardiff University.
<http://onlinelibrary.wiley.com/doi/10.1002/ange.19530650106/pdf> **34 (5/6)**, 449–530 (1901).
92. Konferenz über Struktur und Eigenschaften fester Oberflächen Lake. Geneva (Wisconsin) USA, 29. September bis 1. Oktober 1952. *Angew. Chemie* **65**, 34–35 (1953).
93. Tran, R. *et al.* Surface energies of elemental crystals. *Sci. data* **3**, 160080 (2016).
94. Xia, Y., Xiong, Y., Lim, B. & Skrabalak, S. E. Shape-Controlled Synthesis of Metal Nanocrystals: Simple Chemistry Meets Complex Physics? *Angew. Chemie Int. Ed.* **48**, 60–103 (2009).
95. Elechiguerra, J. L., Reyes-Gasga, J. & Yacaman, M. J. The role of twinning in shape evolution of anisotropic noble metal nanostructures. *J. Mater. Chem.* **16**, 3906 (2006).
96. Ino, S., Ino & Shozo. Epitaxial Growth of Metals on Rocksalt Faces Cleaved in Vacuum. II. Orientation and Structure of Gold Particles Formed in Ultrahigh Vacuum. *J. Phys. Soc. Japan* **21**, 346–362 (1966).
97. Ino, S. Stability of Multiply-Twinned Particles. *J. Phys. Soc. Japan* **27**, 941–953 (1969).
98. Jupille, J. & Thornton, G. *Defects at Oxide Surfaces*. (Springer International Publishing, 2015).
99. Winterbottom, W. . Equilibrium shape of a small particle in contact with a foreign substrate. *Acta Metall.* **15**, 303–310 (1967).
100. Liu, X. *et al.* Metals on graphene: correlation between adatom adsorption behavior and growth morphology. *Phys. Chem. Chem. Phys.* **14**, 9157 (2012).
101. Engel, J., Francis, S. & Roldan, A. The influence of support materials on the structural

and electronic properties of gold nanoparticles – a DFT study. *Phys. Chem. Chem. Phys.* **21**, 19011–19025 (2019).

102. Ayers, J. E. *Heteroepitaxy of semiconductors : theory, growth, and characterization*. (CRC Press, 2007).

Chapter 2

Theoretical background

Electronic structure

A description of the quantum behaviours of atoms and molecules and, therefore, the fundamental properties of systems, can be obtained through the solution of the Schrodinger equation, the time-independent form is shown below (Equation 2.1).¹

$$\hat{H}\Psi = E\Psi \quad (2.1)$$

Where \hat{H} is the Hamiltonian operator, containing the kinetic (\hat{T}) and potential (\hat{V}) energy contributions, E is the system energy, where the lowest value corresponds to the ground state and Ψ is the wavefunction, which contains all the information of the system.

The Schrodinger equation can be solved exactly for hydrogenic systems or simple systems such as a particle in a box or a harmonic oscillator. However, where there are multiple electrons interacting (greater than two-bodied system), it becomes increasingly difficult to the point of becoming inconceivable.

There are certain approximations put in place to help provide an approximate solution to the Schrodinger equation. The most significant example of these is the Born-Oppenheimer approximation, which allows the nuclear and the electronic parts of the system to be treated separately due to the large difference in their mass and velocities. By applying this approximation, the Hamiltonian operator becomes the electronic Hamiltonian (\hat{H}_{el}) and is reduced from Equation 2.2 to 2.3.

$$\hat{H} = \hat{T}_n + \hat{T}_e + \hat{V}_{ee} + \hat{V}_{nn} + \hat{V}_{ne} \quad (2.2)$$

$$\hat{H}_{el} = \hat{T}_e + \hat{V}_{ee} + \hat{V}_{nn} + \hat{V}_{ne} \quad (2.3)$$

The electronic Hamiltonian operator can then be expanded to:

$$\hat{H}_{el} = \sum_{i=1}^N -\frac{\hbar^2}{2m_e} \nabla_i^2 + \sum_i \sum_{j>i} \frac{e^2}{4\pi\epsilon_0 |r_i - r_j|} + \sum_k \sum_{l>k} \frac{Z_k Z_l e^2}{4\pi\epsilon_0 |R_k - R_l|} - \sum_k \sum_i \frac{Z_k e^2}{4\pi\epsilon_0 |R_k - r_i|} \quad (2.4)$$

Where Z_k and Z_l are the charge on the nuclei (k, l), m_e and e are the mass and charge of an electron, ϵ_0 is the vacuum permittivity, \hbar is the reduced Planck's constant, R_k and R_l are the positions of nuclei k and l , and r_i and r_j are the positions of the electrons i and j .

An additional complexity to solving the Schrodinger equation is in obtaining the wavefunction of the system. When there are multiple bodies, such as electrons in the system, then the wavefunction becomes a product of the individual wavefunctions of these bodies, which are functions of each of the spatial coordinates of each of the N electrons. To put this into perspective, for a single molecule of water that contains 10 electrons, the number of dimensions of the wavefunction equates $(3N)$ to 30. For something more chemically complex, such as a slab of MgO with 64 atoms of Mg and 64 atoms of O, this results in 3,840 dimensions. This renders ab initio calculations (from first principles that relies purely on quantum mechanics) unfeasible for complex systems due to computational power and time requirements and is why a wide range of alternative approaches have been developed. Therefore, pure ab initio methods, e.g. Hartree-fock (HF), which use first principle mathematics to solve the Schrodinger equation, would not be suitable to calculate the properties of a system, such as the one under examination here. In the Au/MgO system, which has the inclusion of a support, the number of atoms increases the complexity to beyond the capabilities of such methods and while calculations may be performed, the time required to compute these properties is prohibitive. One of the aims of this thesis is to screen a selection of methods previously used successfully for a number of different systems and discern their effectiveness in describing the Au_n/MgO ($n < 20$) system.

Density functional theory (DFT)

Density functional theory (DFT) has been used successfully as an electronic structure method by finding approximate solutions to Schrodinger equation using electron density instead of wavefunctions.

Although early ideas were introduced by Thomas, Fermi and Dirac,²⁻⁴ these were proved and expanded upon by Kohn and Hohenberg,⁵ who put forward the theorems that DFT rests upon. The first theorem states that the ground state energy from Schrodinger's equation is

a unique functional of the electron density. Therefore, the ground state energy can be expressed as $E[n(r)]$, the electron density $n(r)$ is related to the wavefunction (ψ) according to Equation 2.5:

$$n(r) = 2 \sum_i \psi_i^*(r) \psi_i(r) \quad (2.5)$$

This is useful, as the electron density uniquely determines all properties of the system, i.e. the wavefunction. The Kohn-Sham equations reproduce the electron density of a system of interacting particles as a collection of non-interacting particles experiencing an effective potential and instead of the huge number of dimensions required to calculate a ψ per electron in the system, this is reduced to three.

The second theorem seeks to help determine the functional that solves the Schrodinger equation through electron density. This is achieved by proving that the correct electron density is the one that minimises the energy of the overall function⁶.

DFT is therefore a self-consistent field (SCF) method, where the most accurate solution for the electron density and energy of a system is obtained through an iterative approach. Firstly, an initial guess for the Kohn-Sham molecular orbitals (χ_i) is made. The electron density ($n(r)$) is calculated for these orbitals using Equation 2.6 from which the Coulomb potential ($\hat{v}_c(r)$, Equation 2.7) and the exchange-correlation potential ($\hat{v}_{xc}(r)$, Equation 2.8) are obtained.

$$n(r) = \sum_{i=1}^N |\chi_i(r)|^2 \quad (2.6)$$

$$\hat{v}_c(r) = \hat{v}(r) + \int \frac{n(r')}{|r - r'|} dr' \quad (2.7)$$

$$\hat{v}_{xc}(r) = \frac{\partial E_{xc}(n)}{\partial n(r)} \quad (2.8)$$

The sum of $\hat{v}_c(r)$ and $\hat{v}_{xc}(r)$ is known as the effective potential (\hat{v}_{eff}):

$$\hat{v}_{eff}(r) = \hat{v}(r) + \int \frac{n(r')}{|r - r'|} dr' + \frac{\partial E_{xc}(n)}{\partial n(r)} \quad (2.9)$$

The Hamiltonian operator for the KS equation (\widehat{H}_{KS}) can now be obtained, and a Schrodinger type equation can be solved, Equation 2.11. Next, a new electron density is calculated from the new KS orbitals. If the new electron density is the same as was previously obtained,

within the set threshold, then convergence has been reached and the solution accepted as correct. If not, then the process is repeated from the calculation of the effective potential until convergence is reached.

$$\hat{H}_{KS} = -\frac{\hbar^2}{2m_e} \nabla^2 + \hat{v}_{eff}(r) \quad (2.10)$$

$$\hat{H}_{KS} \chi_i = E_{KS} \chi_i \quad (2.11)$$

Whilst the electron density obtained by the Kohn-Sham equations can be considered correct, the approximation of the wavefunctions is inaccurate. However, a good qualitative analysis can be made and quantitative differences obtained from the properties found using DFT, as the shape, symmetry and energetic order of KS orbitals is very similar to that of the HF ones.

Additionally, obtaining energy as a function of electron density in DFT means that long-range interactions are not properly represented. Any property relating to long-range interactions is therefore, overall more poorly modelled by DFT methods.

Functionals

The DFT theorems proved that the exact answer can be obtained if you have a perfect functional. Therefore, computational chemists continue to develop the best functional to apply to a particular system that allows them to find the exact properties of that system in ground state. As a result of this search, there are many functionals that have been developed. Examples include, local density approximation (LDA), Generalised Gradient approximation (GGA) and hybrid functionals.

LDA is a class of functional where the E_{xc} , would be obtained exclusively from the density (n) at that position (r), i.e. the “local” value of n . This value is usually derived from a uniform electron gas and means that n is equal at all positions of (r). LDA functionals work well for systems where the electron density does not change much across the space, e.g. bulk of heavy metals. For molecules or ionic systems, where the electron density is generally far from uniform, LDA gives a poor estimation of bond distances and energies.

An improvement upon LDA for less uniform systems is the semi-local GGA functional. As is implied by the name, the electron density is now not only described in terms of density, but also in terms of density gradient. This allows variations in the electron density to be taken into account and improves the representation of localised bonds and energies, as well as being better at representing charge densities. However, GGA’s still have some weaknesses, for example, the energy of unoccupied orbitals is underestimated, while adsorption energies

are overestimated. Additionally, long-range interactions are still inadequately modelled, and corrections have been implemented into calculations to improve this, e.g. dispersion corrections as described below. Whilst many GGA functionals use empirical parameters, some GGA's have been developed based on rational function expansions of the reduced gradient and do not require empirical additions. GGA functionals of this type include PBE, which is employed in the DFT calculations presented.

Hybrid functionals have been developed with the aim of improving the aforementioned issues with GGA's. These functionals include some of the exact exchange energy from HF calculations, along with some of the exchange and correlation energy from DFT functionals, such as GGA. A commonly used example of a hybrid functional is the B3LYP model, seen in Equation 2.12:

$$E_{XC}^{B3LYP} = (1 - a)E_X^{LSDA} + aE_X^{HF} + b\Delta E_X^B + (1 - c)E_C^{LSDA} + cE_C^{LYP} \quad (2.12)$$

Where a , b and c are 0.20, 0.72 and 0.81, respectively. E_X^{LSDA} is the exchange energy from a LDA functional that is adapted for spin polarisation, i.e. local spin density approximation (LSDA).

Basis set - planewaves

A basis set also needs to be defined for the atoms to compute the whole system energy. In this thesis, due to the periodic boundary conditions set up for the calculations, the wavefunctions of the system are described as planewaves rather than atom centred basis sets. Planewaves are also periodic and so their use retains the periodicity of the model.⁷

The periodicity of the system is described by Equation 2.13:

$$\Psi(\mathbf{r}) = \Psi(\mathbf{r} + \mathbf{R}) \mid \mathbf{R} = n_1\mathbf{a}_1 + n_2\mathbf{a}_2 + n_3\mathbf{a}_3 \quad (2.13)$$

Where \mathbf{R} is the translational vector of the unit cell, n_n are integers and \mathbf{a}_n are the lattice vectors for the primitive cell.

The wavefunction is limited to the number of electrons in the unit cell by the Bloch theorem. Each one-electron wavefunction is expressed as a product of a periodic part and a wave-like part.

$$\psi_n(\mathbf{r}) = f_n(\mathbf{r})e^{n\mathbf{k}\mathbf{r}} \mid f_n(\mathbf{r}) = f_n(\mathbf{r} + \mathbf{R}) \quad (2.14)$$

Where $e^{n\mathbf{k}\mathbf{r}}$ is the exponential function for the planewave part with \mathbf{k} as the wave vector, which is confined to the first Brillouin zone (the name given to the primitive cell in reciprocal space). As the periodic function can be expressed as a linear combination of planewaves, the

periodic part of these functions can be written as a Fourier series, this allows the use of the Fast Fourier Transform in the calculations to move between reciprocal and real space. The wavefunction can consequently be expressed in terms of reciprocal lattice vectors (\mathbf{G}) according to:

$$\psi_n(\mathbf{r}) = \sum c_{n,\mathbf{K}} e^{n\mathbf{K}r} = \sum c_{n,(k+\mathbf{G})} e^{n(k+\mathbf{G})r} \quad | \quad \mathbf{G} = m_1 b_1 + m_2 b_2 + m_3 b_3 \quad (2.15)$$

Where k and \mathbf{K} are wave vectors, m_n are integers and b_n are the reciprocal lattice vectors. The notation $k + \mathbf{G}$ can be interchanged with \mathbf{K} as vectors that differ by a reciprocal lattice vector are equivalent.

To represent any non-periodic densities in the cells, it takes a considerable number of planewaves, as planewaves fill up the space. However, in practice and below a certain scale, the wavefunction can be described as smoothly varying and the coefficients ($c_{n,(k+\mathbf{G})}$) become small for large values of $|k + \mathbf{G}|$. The cut-off point is referred to as the planewave kinetic energy limit and should be greater than or equal to those planewaves required to represent the kinetic energy in the system, at a minimum:

$$E_{cut} \geq \frac{1}{2} |k + \mathbf{G}|^2 \quad (2.16)$$

However, appropriate benchmarking calculations seeking energy convergence are performed to ensure an appropriate planewave kinetic energy cut-off is chosen for the system in use, i.e. supported Au cluster on MgO. The application of the planewave cut-off energy allows planewaves as basis sets to be widely used in solid state chemistry and other areas where periodicity is required⁸.

There is an additional problem with the use of planewaves as basis sets that needs to be resolved. Real wavefunctions are smooth in the regions where bonding occurs, however there are strong oscillations in the wavefunctions near the nucleus from its strong attractive

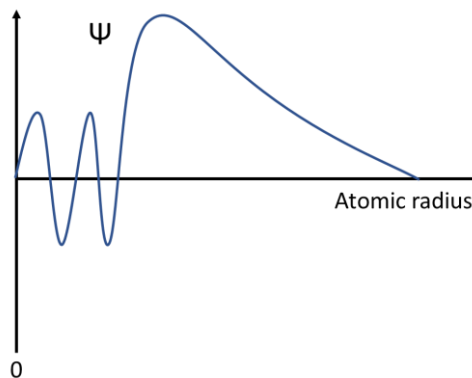


Figure 2.1: Schematic diagram representing how the wavefunction changes with atomic radius.

potential, as represented in Figure 2.1. This increases the number of planewaves needed to describe this region.

The so-called augmented planewave methods, e.g. projector-augmented wave (PAW),^{9,10} which is the method used for DFT calculations throughout this thesis, do not use planewave functions to describe the core regions but pseudopotentials. Whilst planewaves are still used to represent the bonding regions for most methods of this type, including PAW, the wavefunctions for the nuclei in the PAW approach are built from a modified pseudo wavefunction, these are used to model the nodal character of the core electrons wavefunctions.

Dispersion forces

Since DFT is a local electronic structure method. The long-range dispersion correction takes the form of a function of interatomic distances. It contains adjustable parameters that are fitted to conformational and interaction energies calculated using an accurate electronic structure method. In the calculations presented along this thesis, the DFT-D3 correction has been employed with the form:

$$E_{disp} = -\frac{1}{2} \sum_{i=1}^N \sum_{j=1}^N \sum_L \left(f_{d,6}(r_{ij,L}) \frac{C_6^{ij}}{r_{ij,L}^6} + f_{d,8}(r_{ij,L}) \frac{C_8^{ij}}{r_{ij,L}^8} \right) \quad (2.17)$$

This DFT-D3 is the third approach to dispersion by Grimme.^{11–13} The first two descriptions consider only pairs of atoms. D2 makes improvements to D by shortening electron correlation ranges overall and for the medium to large ranges, dampening the $\frac{C_6^{ij}}{r_{ij}^6}$ term. In a further improvement to the correction, D3 considers triplets of atoms to account for three-body effects. This is achieved in an almost *ab initio* fashion, using only two parameters, atom pairwise cut off distances r_0^{ij} and dispersion coefficients C_n^{ij} calculated for all chemically relevant elements.

Atomic charges

The fact that electrons are not localised in a system means there is an opportunity to measure the charge partitioning between atoms. Throughout this thesis, this is achieved using Bader charge analysis according to the Quantum Theory of Atoms in Molecules.¹⁴ The topology of the charge distribution is dominated by the force between the nuclei and the electrons causing the electron density to fluctuate in the region of space it occupies. Electron density will vary and reveal the atomic structure of the system. For example, the stationary

density points at which zero density gradients are observed can be used to distinguish the atomic contributions of the system.

Exploration of the potential energy surface (PES)

Generally, potential energy surfaces (PES) are representations of the potential energy as a function of the relative positions of the atoms in a system, as is the case here and seen in Figure 2.2.

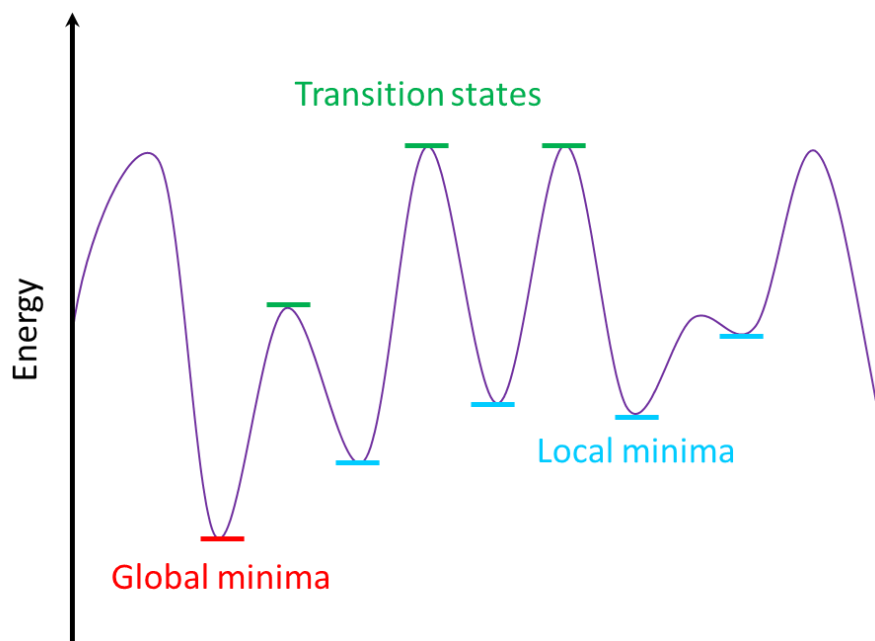


Figure 2.2: A schematic representation of a 2D potential energy surface (PES) showing the locations of the transition states (saddles points) in green, local minima in blue and global minima in red.

The process of global optimisation, as attempted for Au/MgO systems in this thesis, seeks to explore the PES in order to determine positions of the atoms that are particularly stable, ultimately revealing the most stable configuration of the system, at the bottom of a potential well, or the *global minima*. The PES also has high energy states between minima, meta stable states, known as transition states, or the stationary saddle points. Computation of these are also required to connect the minima and construct the PES.

Minimisation to the ground state

To obtain the ground state energy of a system, the species in the system, i.e. nuclei and electrons, must be in their lowest energy positions. Initially, the minimisation of the system's electronic configuration is undertaken to obtain the ground state where the ions are static. Then, the system will undergo a similar optimisation processes to find the lowest energy with regard to its ionic positions.

Minimisation to the ground state for a system is achieved when $E(\mathbf{r}_i)$, \mathbf{r}_i being a set of positions (\mathbf{r}), is at a local minimum. Algorithms utilise $E(\mathbf{r}_i)$ (the energy as a function of \mathbf{r}_i) and $\partial E/\partial \mathbf{r}_i$ (the derivative of the energy which respect to \mathbf{r}_i) to find the ground state. Algorithms that use the second derivatives can be more successful but are more computationally expensive.

The methods employed by the VASP package, and used in DFT calculations here for the minimisation, are the simple Davidson iteration scheme, the conjugate-gradients (CG) method and Residual Minimization scheme, direct inversion in the iterative subspace (RMM-DIIS, also known as quasi-Newton RMM-DIIS), all of which use gradients, $\partial E/\partial \mathbf{r}_i$ to calculate the next step.¹⁵

For an initial geometry, the electronic ground state is calculated using either the Davidson or the RMM-DIIS method. The Davidson scheme requires knowledge of other wavefunctions in the system, so is slower than the RMM-DIIS, but often more successful for convergence of the minimisation. The RMM-DIIS, does not require the additional wavefunction information, so is significantly faster. These algorithms can be used together, the first few steps performed using the Davidson algorithm, in order to get closer to the minima and then the subsequent steps use the RMM-DIIS algorithm to achieve faster convergence.

From the electronic ground state obtained for a particular geometry, the algorithms (CG or RMM-DIIS) subsequently evaluate the forces of on the ions to predict a new geometry. This process is iterative until convergence is reached. While the CG method can be used with a moderate guess at the positions of the ions at ground state, the RMM-DIIS algorithm can only be used when the initial set of positions (\mathbf{r}_i) are very close to the ground state positions. This is because the algorithm builds up an approximation of the Hessian matrix (the second derivative matrix of the system, which describes the local curvature of the function) for which, it requires very accurate forces, otherwise it will fail to converge.

Transition state (TS) methods

Figure 2.2 shows the position of transitions states on the PES. The minimum energy path (MEP) is from one minimum to another, connected through the TS, which is associated with the lowest energy cost. The energetic barriers associated with the MEP are calculated by determining the energy difference between the initial state and the potential energy maxima (the transition state) along the path. Finding the correct paths and the correct transition states can be complex and there are several methods used to find the them. Transition state

structures can be determined by searching for saddle points on the potential energy surface (PES). The saddle point is a position on the PES corresponding to a minimum in all directions except one (the reaction coordinate), that is having a single imaginary frequency along the reaction coordinate.

There are many methods used to determine saddle points. Some methods, e.g. DIMER^{16,17} attempt to find the TS with only the initial state and a presumed MEP (minimum energy path). Each step in these methods requires evaluation of the forces on the atoms so they are limited to rather small systems. The DIMER method¹⁶ does not use structures of initial or final minima's, but instead two very close snapshots on the PES are used to form a "dimer". This makes the method more applicable to reactions where the reaction coordinate is not accurately known. Additionally, the DIMER is suitable for use with systems where the calculation of second derivatives (as is the case with the other methods that require the use of a hessian matrix) is too difficult, as it only makes use of first derivatives of the potential energy. The created DIMER is moved uphill in energy from the starting position whilst being simultaneously rotated to find the direction of the lowest curvature. A translational step in the direction of the resulting net force moves the dimer towards a minimum. Thus, a modified force is employed where the force along the dimer axis is inverted, moving the dimer towards the saddle point instead.

Alternative methods use more than one point on the path taking both the initial and final states. The simplest example of these is the drag method, also known as the reaction coordinate method.^{18,19} Firstly, a subset of the coordinates in the system is used to define a progress variable, often this is a linear interpolation between the initial and final configurations. This drag coordinate is fixed while all other degrees of freedom are relaxed to minimise the total energy. Next, from initial state to final state (one minima to another) the drag coordinate is followed. Unfortunately, the drag method has a tendency to find discontinuous paths that do not lead to the correct TS.

Another alternative is the nudged elastic band (NEB) method. Determining the TS is achieved by taking "snapshots" of the system between the initial and final state, that is several configurations of the system between the initial and final state, along the MEP. In the NEB method¹⁹, images are created by constrained optimisations of a selected number of structures extrapolated between the initial and final states. The images are then linked by simulated spring forces, which are added to the internal forces in the structures producing equally spaced images of the path. There are two forces acting on each image, a force parallel

to the reaction path (following a vector (spring) to the next image) and a force perpendicular to that path. The extent of the perpendicular force determines how close the image is to the reaction path. If the image is correctly placed on the path, the perpendicular force should be zero. The only force acting on the image would be the one taking it along the reaction path i.e. the parallel force. The algorithm is used to assess the degree of the perpendicular force and amend the structure until this perpendicular force is zero. The spring forces are added to the parallel force to prevent all the images from falling into energy minima. Subsequent amendments to NEB's, e.g. climbing image NEB's,²⁰ have been made to obtain configurations nearer to the TS by driving the highest energy image nearer to the saddle point. This is accomplished by inverting its normal net force instead of the spring force. The forces on the image in the direction of the reaction coordinate increase in energy while being minimised in all other directions, rendering finding the TS easier. The requirement of an optimisation and an evaluation of the forces for each "snapshot" means that running the NEB method to find TS's can be computationally expensive.

Model description

Once the parameters for the electronic structure calculations and the determination of the PES have been determined, then, a model of the Au/MgO system is required. In the case of the present thesis, the model system is made up of surface atoms, Mg and O and adsorbed Au atoms, each atom having three coordinates (x , y and z) that describe its position in space. The greater the number of atoms in the system the greater the computational demand. In order to study supported Au clusters on MgO, the MgO support is modelled using a "slab".

Initially, the unit cell, the smallest possible repeating unit of MgO (see Figure 2.3), is replicated in all directions to simulate bulk MgO, also seen in Figure 2.3. An initial guess of the MgO lattice parameter was taken from experimental studies, (4.21 Å).^{21,22} This MgO cell was then optimised and the lattice parameter, 4.195 Å, obtained. As MgO has a simple cubic structure, $a = b = c = 4.195157 \text{ \AA}$ and $\alpha = \beta = \gamma = 90^\circ$. Following the modelling of the optimised bulk unit cell, to obtain the correct miller index at the surface, the slab is cut through the correct symmetry plane. The total number of atomic layers in the surface is also an important consideration particularly if the system has a specific stoichiometry that needs accommodating or is magnetic. Once the required surface has been created then a vacuum is fitted to the z direction, as shown in Figure 2.3, generating the slab model. This forms a periodic system in the xy plane but creates a space between surfaces large enough to accommodate the adsorption of atoms/molecules (in this case Au clusters) to the surface, without any interaction with the periodically repeated surface above. The size of the slab

model in the x and y direction is also important, to ensure that interactions between adsorbed clusters on the surface between lateral cells is avoided. The presence of the vacuum leads to two surfaces being produced (top and bottom). The bottom layers of atoms are fixed at the bulk lattice parameter to recreate the behaviour of the atoms were they part of the bulk, whilst the top layers of atoms are free to relax more. Benchmarking calculations finding energy convergence were performed to determine the number of layers allowed to relax and the thickness of the slab. This is to ensure that the surface is represented as accurately as possible whilst still managing a suitable level of computational demand.

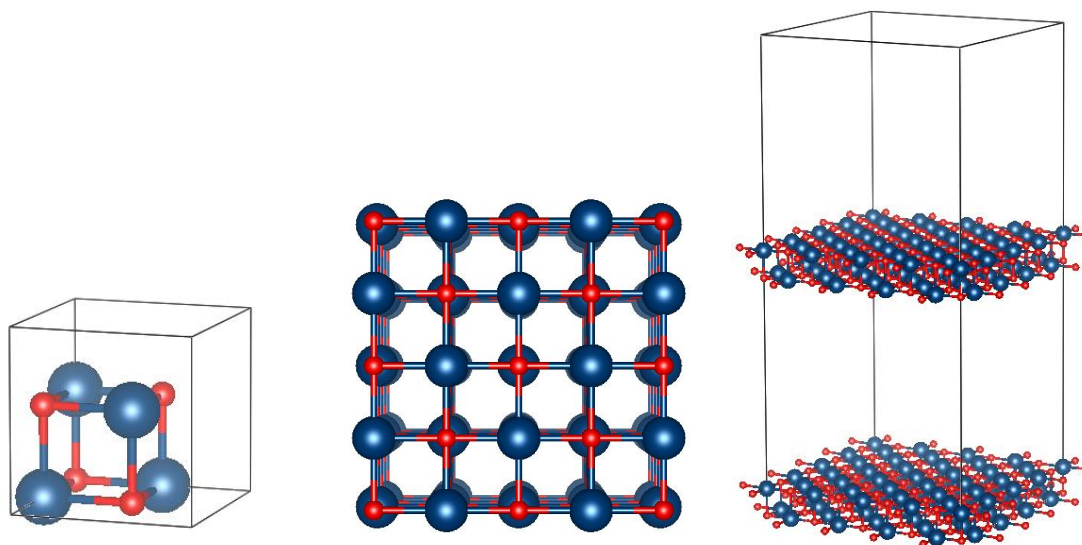


Figure 2.3: MgO models used in this work. a) shows the MgO unit cell, b) shows the MgO bulk and c) shows the MgO surface with a 10\AA vacuum. Mg atoms in blue, O atoms in red.

Characterisation

Band structures, Density of states (DOS) and Crystal Orbital Hamilton Population (COHP)

Whilst Bloch's theorem allows us to model an infinite system by only calculating a finite number of electronic wavefunctions, there is still an infinite number of k-points to consider as each electron occupies a definite k. Fortunately, in practice, we need only to choose a sample of k-points as the wavefunctions of nearby k-points will be nearly identical. Therefore, a region of k-space can be represented by the wavefunction at a single k-point. The Brillouin zone can be made irreducible by applying the point group symmetries of the lattice, leaving no k-points related by translational symmetry. Hence, the symmetry of the lattice can be used to reduce the number of k-points required even further.

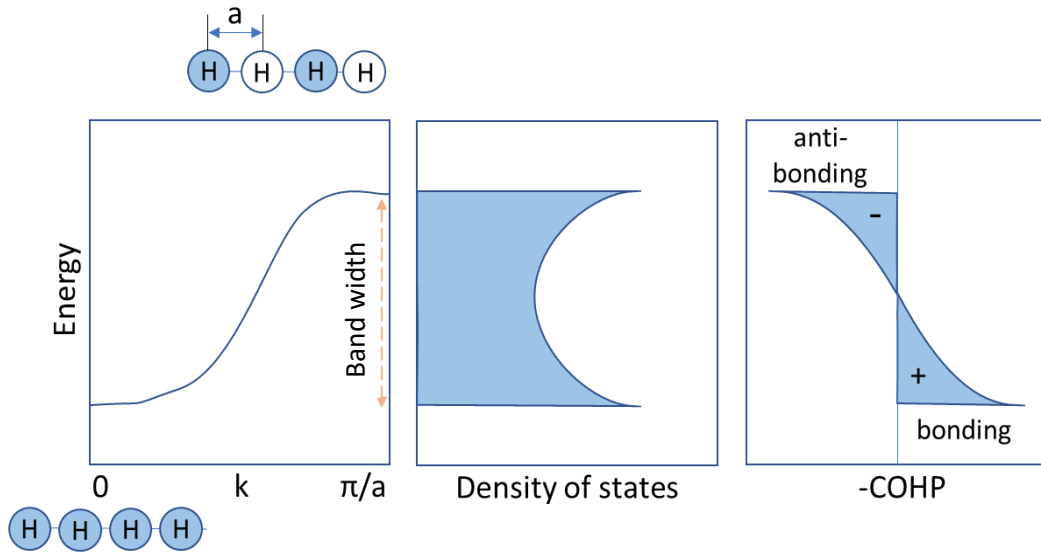


Figure 2.4: Graphical representation of the band structure, the DOS and the -COHP for a chain of hydrogen atoms in 1D. Where a refers to the lattice spacing, k is used here as an index which labels which irreducible representation the orbitals take up and the orange dashed arrow shows the width of the band.

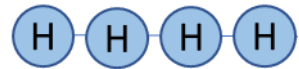
Coordinates in the reciprocal space are inversely proportional to those in the real space. Therefore, when the size of the unit cell is large in real space, then a smaller number of k -points are required. For example, where a vacuum is fitted to separate slabs in the z -direction, generally only a single k -point is used to sufficiently sample the Brillouin zone in that direction. Efficient k -point sampling schemes have been developed, such as the one utilised for the Au/MgO system here by Monkhorst and Pack.^{23,24}

Graphical plots of $E(k)$ vs k , are called band structures, and show the orbitals in a “band”, by making use of translational symmetry.²⁵ An example of a band structure for a chain of hydrogen atoms in 1D is shown in Figure 2.4, a chain of H atoms is chosen as it provides a very simple system with which to describe the concept, regardless of how unfeasible it is chemically. The orbital combinations for values of k can be calculated using Equation 2.18:

$$\varphi_k = \sum_n e^{ikna} \chi_n \quad (2.18)$$

For example, for the 1D chain of H atoms, where k has a value of 0:

$$\varphi_0 = \sum_n e^0 \chi_n = \sum_n \chi_n = \chi_0 + \chi_1 + \chi_2 + \chi_3$$



In this example, as the orbitals have all the same sign and are s orbitals, they are all in the same phase and as such the wavefunction has the most favourable bonding character. If the value for k for the same example system was π/a then:

$$\varphi_{\pi/a} = \sum_n e^{\pi in} \chi_n = \sum_n (-1)^n \chi_n = \chi_0 - \chi_1 + \chi_2 - \chi_3$$

The single line in the graph of energy versus values of k between 0 and π/a in Figure 2.4 represents a band. The band width (or



dispersion) is related to the degree of overlap between the orbitals and is shown by the orange dashed line in Figure 2.4. In a system more complex than a 1D chain of H atoms there would be a greater number of “bands” than the single one shown in Figure 2.4. The number of bands is related to the number of different types of orbitals governed by the species in the system. The position of the bands in relation to each other shows their relative energies and can help to determine the electronic properties of the system, e.g. if they conductors, semi-conductors or insulators.

The DOS for the 1D H chain system is also represented in Figure 2.4. The DOS is defined as the number of states occupied in a particular energy range. The steeper the gradient of the band, the fewer the number of states lie in a defined energy range and vice versa. In this way the shapes of DOS curves can be predicted from the band structure. On addition of the Fermi energy, the energy difference between the conduction and valence band of the DOS, more information about the system can be obtained. For example, the number of occupied states can be calculated by integrating the DOS curve up to the Fermi energy, also known as the valence band. The area above the Fermi energy is known as the conduction band and is where the bands for the unoccupied orbitals are found.

Information regarding the location of electron density can also be obtained by taking the sum of the electronic density contributions for each atomic orbital (AO) and distributing it over each occupied orbital. This is known as the Mulliken overlap population (Equation 2.19):

$$\text{Population} = 2c_i c_j S_{ij} \quad (2.19)$$

Where S is an overlap integral, between the atomic orbitals of i and j , and c_i and c_j are the coefficients of the basis functions for the molecular orbitals, i and j .

This is performed for several k -points in the Brillouin zone and is returned to real space by averaging over these. This results in partitioning of the total DOS (projected DOS), into the contributions from particular atoms or orbitals. An integration of the areas of density up to the Fermi energy gives the total electron density for that particular atom or orbital.

The greater the magnitude of the overlap integral (S_{ij}), the greater the area of shared electron density, and this scales with bond order. If the signs of c_i and c_j are the same then the interaction is bonding, if the signs are opposite then the interaction is anti-bonding. Therefore, the degree of bonding is defined by c_i , c_j and S_{ij} . By applying the Mulliken overlap

density to the DOS, an overlap population weighted density of states is obtained, otherwise known as the crystal orbital overlap population (COOP). The COOP is specified for a particular bond, for which the positive regions show bonding character and the negative regions show anti-bonding character, see Figure 2.4. The amplitude of the curve is defined by the number of states in the energy interval, the degree of orbital overlap (S_{ij}) and the magnitude of c_i and c_j . The integral of the COOP gives the total overlap population.

The COOP is closely related to the COHP, or crystal orbital Hamilton population, however, for COHP, the band structure energy is partitioned rather than the electron number. Instead of obtaining the sum of the electrons, as is the case when the COOP curve is integrated, when the COHP is integrated, an energy value is obtained that can give an indication of bond strength.

In order to make COHP plots read the same as COOP plots, they are plotted as negative COHP. This is because instead of a positive interaction leading to a bond, a bonding interaction leads to a negative difference in energy. Therefore, bonding states stay to the right (positive) and antibonding states stay to the left (negative).

References

1. House, J. E. *Fundamentals of quantum chemistry. Choice Reviews Online* **42**, (Elsevier Science, 2005).
2. Thomas, L. H. The calculation of atomic fields. *Math. Proc. Cambridge Philos. Soc.* **23**, 542–548 (1927).
3. Fermi, E. Statistical method to determine some properties of atoms. *Rend. Accad. Naz. Lincei* **6**, 602–607 (1927).
4. Dirac, P. A. M. Note on exchange phenomena in the Thomas atom. in *Mathematical Proceedings of the Cambridge Philosophical Society* **26**, 376–385 (Cambridge University Press, 1930).
5. Hohenberg, P. & Kohn, W. Inhomogeneous Electron Gas. *Phys. Rev.* **136**, B864–B871 (1964).
6. Kohn, W. & Sham, L. J. Self-Consistent Equations Including Exchange and Correlation Effects. *Phys. Rev.* **140**, A1133–A1138 (1965).
7. Springborg, M. & Joswig, J.-O. *Chemical modelling. Volume 14.* (Royal Society of Chemistry, 2018).
8. Dovesi, R., Orlando, R., Roetti, C., Pisani, C. & Saunders, V. R. The Periodic Hartree-Fock Method and Its Implementation in the Crystal Code. *Phys. status solidi* **217**, 63–88 (2000).
9. Blöchl, P. E. Projector augmented-wave method. *Phys. Rev. B* **50**, 17953–17979 (1994).
10. Kresse, G. & Joubert, D. From ultrasoft pseudopotentials to the projector augmented-wave method. *Phys. Rev. B* **59**, 1758–1775 (1999).
11. Grimme, S. Accurate description of van der Waals complexes by density functional theory including empirical corrections. *J. Comput. Chem.* **25**, 1463–1473 (2004).
12. Grimme, S. Semiempirical GGA-type density functional constructed with a long-range dispersion correction. *J. Comput. Chem.* **27**, 1787–1799 (2006).
13. Grimme, S., Antony, J., Ehrlich, S. & Krieg, H. A consistent and accurate *ab initio* parametrization of density functional dispersion correction (DFT-D) for the 94

- elements H-Pu. *J. Chem. Phys.* **132**, 154104 (2010).
14. Bader, R. F. W. & Nguyen-Dang, T. T. Quantum Theory of Atoms in Molecules—Dalton Revisited. *Adv. Quantum Chem.* **14**, 63–124 (1981).
 15. Pulay, P. Convergence acceleration of iterative sequences. the case of scf iteration. *Chem. Phys. Lett.* **73**, 393–398 (1980).
 16. Henkelman, G. & Jónsson, H. A dimer method for finding saddle points on high dimensional potential surfaces using only first derivatives. *J. Chem. Phys.* **111**, 7010–7022 (1999).
 17. Heyden, A., Bell, A. T. & Keil, F. J. Efficient methods for finding transition states in chemical reactions: Comparison of improved dimer method and partitioned rational function optimization method. *J. Chem. Phys.* **123**, 224101 (2005).
 18. Buendía, F. & Beltrán, M. R. THE EUROPEAN PHYSICAL JOURNAL D O 2 adsorption on Au n Rh n = 1–5 neutral and charged clusters. *Eur. Phys. J. D* **70**, (2016).
 19. Jonsson, H., MILLS, G. & JACOBSEN, K. Nudged elastic band method for finding minimum energy paths of transitions. in *Classical and Quantum Dynamics in Condensed Phase Simulations* 385–404 (1998). doi:10.1142/9789812839664_0016
 20. Henkelman, G., Uberuaga, B. P. & Jónsson, H. A climbing image nudged elastic band method for finding saddle points and minimum energy paths. *J. Chem. Phys.* **113**, 9901–9904 (2000).
 21. Madelung, O., Rössler, U. & Schulz, M. Magnesium oxide (MgO) crystal structure, lattice parameters, thermal expansion. in *II-VI and I-VII Compounds; Semimagnetic Compounds* (eds. Madelung, O., Rössler, U. & Schulz, M.) 1–6 (Springer Berlin Heidelberg, 1999). doi:10.1007/10681719_206
 22. Evarestov, R. A. *Quantum Chemistry of Solids: LCAO Treatment of Crystals and Nanostructures*. (Springer Berlin Heidelberg, 2013).
 23. Chadi, D. J. & Cohen, M. L. Special Points in the Brillouin Zone. *Phys. Rev. B* **8**, 5747–5753 (1973).
 24. Monkhorst, H. & Pack, J. Special points for Brillouin zone integrations. *Phys. Rev. B* **13**, 5188–5192 (1976).
 25. Hoffmann, R. How Chemistry and Physics Meet in the Solid State. *Angew. Chemie*

Int. Ed. English **26**, 846–878 (1987).

Chapter 3

Au_n/MgO cluster determination using DFT methods

Introduction

Many heterogenous catalysts take the form of metallic nanoparticles decorating the surface of a support. As described, the efficiency of supported catalysts is often related to structural properties such as particle size and shape. These properties are strongly influenced by the interactions between the support material and the metal particle.^{1,2} For catalytic applications, typical support materials include oxides of; main group elements (e.g. MgO, Al₂O₃, SiO₂), transition metals (e.g. TiO₂, ZrO₂, Fe₂O₃) or rare-earth metals (CeO₂) and carbon-based materials.

The choice of the support for a catalyst is generally based on screening of common and readily available materials rather than rational design, which requires not only an understanding on the desired properties of the catalyst but also a detailed knowledge regarding the effect that the support material has on these properties. To this end, quantum chemical calculations on model systems can offer detailed information under atomically controlled conditions on the structural and electronic properties of supported metal particles and their interaction with the support material. In this chapter, the support chosen reflects a single example of the typical supports considered for catalyst synthesis, magnesium oxide (MgO). MgO is a non-reducible metal oxide, which crystallises in a simple rock salt structure,^{3,4} and its most stable surface, MgO(001)⁵, can be prepared relatively defect free.⁶ It has been used extensively as support material for metal catalysts used in a wide range of applications,⁷⁻⁹ and it is used in areas such as surface science¹⁰ and electronics.^{11,12}

In terms of the active metal employed in the computer simulations of catalysts, Au clusters, have been investigated for their catalytic properties since the discovery of their excellent performance in reactions such as, the hydrochlorination of acetylene when supported on a carbon support,¹³ low temperature oxidation of CO when Au clusters are supported on a range of metal-oxide and activated carbon supports,¹⁴ oxidation of alcohols when supported

on a MgO support¹⁵ and perhaps most significant, with a carbon support, the activation of molecular oxygen.¹⁶ Valuable contributions such as these have spurred a wealth of research into the noble metals ability to catalyse various reactions and, in the quest for understanding the activity of supported Au catalysts, it has been concluded that activity is highly size-dependent.¹⁷ This has been evidenced by the work of other groups who have demonstrated decreasing activity for Au at particle sizes above 5 nm.^{18,19}

The reasons for this size-dependent activity have been comprehensively described in literature²⁰ as being due to the unique properties that particles exhibit at nanoscale. These include a high surface-to-bulk ratio, the availability of low-coordination atoms,²¹ and the presence of perimeter sites at the Au–support interface.²²

Methodology

Computational details

In the preparation of supported metal cluster calculations, a slab model of MgO was created as described in Chapter 2. A magnesia (001) slab, as (001) is determined to be the most stable surface,²³ was modelled for clusters with up to four Au atoms, by a four-layer supercell (2x2) slab of 32 magnesium and 32 oxygen atoms (surface area = 70.4 Å²). For Au cluster sizes greater than 4 atoms ($n > 4$), a two-layer slab supercell (4x4) consisting of 64 magnesium and 64 oxygen atoms (surface area = 281.6 Å²) was used. The size of the slab is increased in the xy plane to ensure that there are no cluster interactions in the x or y direction with increasing cluster size. Accordingly, the number of k-points was adjusted for slab size, i.e. a 11x11x1 Monkhorst-Pack k-point grid²⁴ was used for the smaller surfaces and a 3x3x1 Monkhorst-Pack k-point grid was determined appropriate for the larger surfaces.

An additional parameter considered was the degree of relaxation. How this is determined is described in Chapter 2. In order to ensure the correct surface-like and bulk-like behaviour of the atoms in the slab, the bottom layers of atoms in the slab are completely fixed in position to the lattice parameters obtained for bulk, in this way, they behave as they would in the bulk. The atoms in the top layers can move (relax) during the calculations. For the small slab (2x2), the bottom two layers have been fixed, for the larger slab (4x4), the bottom layer was fixed.

The slabs were separated by a 10 Å vacuum for up to six Au atoms and 20 Å for larger cluster sizes. A 10Å vacuum fitted in the z direction was ascertained on observation of the energy convergence to be sufficient to prevent interaction between slabs, for the naked surface and for small supported Au cluster sizes. However, the vacuum was increased with larger Au_n (n

> 6 atoms) cluster sizes to 20Å, in order to remove any possibility of interaction between slabs in the z direction with increasing metal cluster size.

Once these slabs had been created and optimised, they were then ready to have Au clusters added to them. Two methodologies employing density functional theory (DFT) were used to find the most stable (lowest energy) Au arrangements on MgO surfaces.

For these calculations, spin-polarised periodic plane-wave DFT calculations were performed with the Vienna Ab Initio Simulation Package (VASP 5).^{25–27} The density functional of Perdew, Burke, and Ernzerhoff (PBE)²⁸ was used to calculate exchange and correlation contributions. Dispersion interactions were implemented using Grimme’s empirical dispersion correction DFT-D3.²⁹ The electronic minimisation was performed using a mixture of the blocked Davidson iteration scheme and the residual minimization method direct inversion in the iterative subspace (RMM-DIIS) algorithm. The former is generally more robust and converges rapidly to the minimum structure whereas the latter is better when the structure is already close to that of a local minimum geometry. This reduces the risk of instabilities in the electronic minimisation that may occur by only using the RMM-DIIS but also balances the time cost associated with utilising the Davidson scheme. Projector-augmented wave (PAW) pseudopotentials^{27,30} as implemented in VASP, were used to describe the nodal character of the core electrons. A kinetic energy cut-off was set at 450 eV for the planewave basis set. Bader charges were calculated to assign partial charges to specific atoms.³¹

General methodology

Several structures of different shapes were created for each cluster size. Two different procedures were followed to generate the supported cluster configurations: i) a systematic build-up and ii) a genetic algorithm (GA). The latter reduces the bias and explores a large number of possible arrangements. For the build-up procedure, taking the previous optimised structure of a cluster, Au_n , an additional Au atom was placed in reasonable positions to create the structures for the next size cluster, Au_{n+1} . Sensible structures based on previous reports of supported Au clusters on the model support were also included in the search.

Measurements

Calculations of the energies of the optimised structures of Au clusters on the surface ($E_{Au_n/MgO}$), the energy of the optimised slab (E_S), and the energies of the Au clusters in the gas phase in the shape (E_{Au_n}) were undertaken. The isolated gas phase cluster energies (E_{Au_n}) were obtained by removing the support after optimisation of the Au_n/MgO system ($E_{Au_n/MgO}$) and running a single point calculation to obtain the energy of the cluster at that

fixed geometry. From these calculations, adsorption energies (E_{ads}) were calculated following Equation 3.1, where n is the number of atoms in the cluster.

$$E_{ads} = (E_S + E_{Au_n}) - E_{Au_n/MgO} \quad (3.1)$$

The adsorption energy is a measure for the strength of the interaction between the cluster and the surface. However, it does not include any deformation energy of the cluster from its most stable structure. Therefore, the binding energy per atom (E_b) of the clusters is also calculated using the gas phase energy of a single Au atom (E_{Au_1}).

$$E_b = \frac{(E_S + n \cdot E_{Au_1}) - E_{Au_n/MgO}}{n} \quad (3.2)$$

The binding energy is a combination of the adsorption energy and the cohesion energy (E_{coh}), which provides a measure of the interactions within the Au cluster, see Equation 3.3.

$$E_{coh} = \frac{n \cdot E_{Au_1} - E_{Au_n}}{n} = E_b - \frac{E_{ads}}{n} \quad (3.3)$$

The charge transfer between the surface and the cluster was evaluated from calculating the charges on each Au atom in the cluster (q_{Au_n}).

Results

MgO support

The naked MgO slabs, (2x2, 4 layers) and (4x4, 2 layers) were both optimised, as per the methodology described. The optimised Mg-O distance in the top and bottom layers was 2.098 Å, for the both the 2x2 and the 4x4 slab. The nearest neighbour O distance was 2.967 Å for all layers of both systems. Upon relaxation of the layers in the slab, the bond distances between the layers varied very slightly, (maximum 0.013 Å) between the two thicknesses, see Figure 3.1.

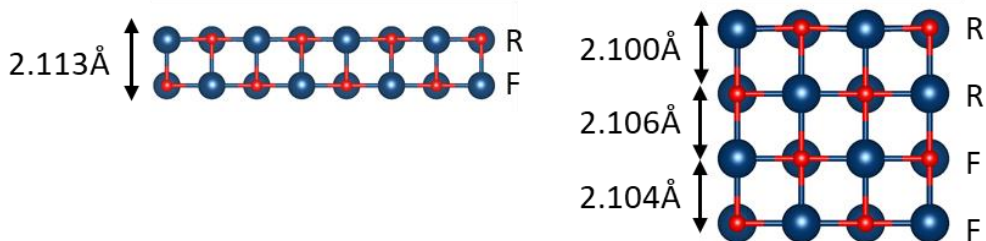


Figure 3.1: MgO slabs, (left) 4x4, 2 layers and (right) 2x2, 4 layers, showing the changes in the distances between the layers. R depicts the layer that have been allowed to relax and F represents the layers that are frozen. Blue = Mg and Red = O.

Structure of supported Au clusters

On the (001) surface of magnesia there are three stable non-equivalent sites for adsorption of a single Au atom, illustrated in Figure 3.2, these are, a position on top of an oxygen atom (T_o), on top a magnesium atom (T_{Mg}) and in the void between two magnesium and two oxygen atoms (H). Au atoms placed on a bridge site (B) between an oxygen atom and a magnesium atom leads to a position on top of the oxygen upon optimisation. The most stable site for a single Au atom adsorption on MgO is on top of the oxygen with an adsorption energy of 1.37 eV. This position is in agreement with previous computational work by Ferrando and Fortunelli³² and is also supported by experimental EPR spectra data produced by Yulikov *et al.*³³ The O top site is found to be 0.27 eV more stable than the next most stable site. The energy of adsorption in the void is found to be 1.09 eV and on top of an Mg atom found to be 0.89 eV, shown in Table 3.1. Further Au atoms are then added to the system, in the methods described above, followed by subsequent optimisation.

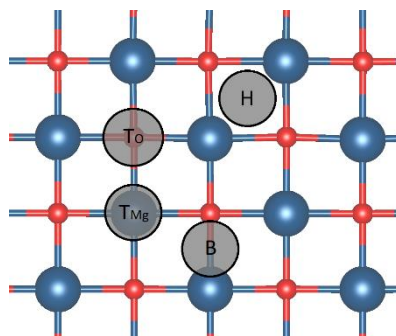


Figure 3.2: Illustration of the adsorption sites of Au on MgO. A site on top of an oxygen atom (T_o), on top of a magnesium atom (T_{Mg}), in the hollow between two magnesium and two oxygen atoms (H) and on a bridge site (B). Blue = Mg and Red = O.

The GA calculations produced a range of possible structures which were optimised using the same previously described method of DFT performed with the systematic build-up methodology. The GA calculations performed here were performed using the Birmingham cluster genetic algorithm package as presented by Shayeghi *et al.*³⁴ Initially, a pool of 20 random structures have their energies evaluated within VASP. The initial pool is then minimised and “parents” are chosen by applying a fitness function, in this case the energy of the structure is used a measure of “fitness”. Once the parents have been chosen, the degree of crossover from each parent is weighted (from pool) and random mutation operations are allowed occur at a rate of 0.1. This rate of mutation balances reduced efficiency from a higher rate, which would impede the mating rate of low energy parents and no mutation, which would reduce structural diversity. Full mutation would essentially make this method a basin hopping approach. If the new structures are lower in energy than those in the existing pool then they replace those structures and become parents. This procedure continues until

energy convergence is reached. For the Au_n/MgO ($3 \leq n \leq 5$) systems computed using GA, the stabilities of the structures produced were compared to the structures generated by the systematic build-up approach. It was found that the GA, whilst finding some new low energy structures, particularly for Au_5 , in the time frame allowed, was not always successful in finding the most stable configuration. The procedure was allowed to run for at least 9 days for each cluster size and energy convergence was not reached in this time. Additionally, the GA did not always find the lowest energy structures as found by the systematic method. As a result, the systematic build-up approach was deemed more suitable for the cluster sizes under analysis, and was the sole method used for determining low energy clusters where $n > 5$.

Tables 3.1 to 3.17 show a selection of low energy configurations obtained for each cluster size ($n = 2-19$). The energy difference between the configurations is calculated by the overall system energy ($E_{Au_n/MgO}$) for that cluster size (n) minus the overall system energy of the lowest energy system for that cluster size. The supported metal clusters are identified as $Au_n[A-B(-C)]X$ for a gold cluster with n atoms in which there are A gold atoms at the cluster-support interface, B in the next layer, and C in third layer growing perpendicular to the surface. The sub index X is added to distinguish clusters with otherwise identical names.

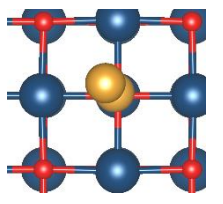
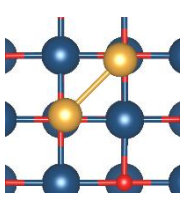
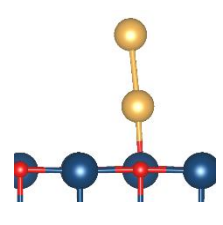
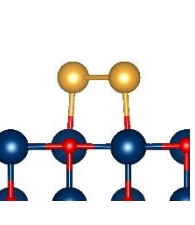
Table 3.1: Schematic representation of on Au on MgO (001), i.e. Au_1/MgO . Au is represented in yellow, O in red and Mg in blue.

	$Au_1[1]_a$	$Au_1[1]_b$	$Au_1[1]_c$
Top			
Side			
ΔE (eV)	0.00	+0.47	+0.27

On addition of a second atom to the first Au atom, using the build-up approach previously described, the cluster preferentially adopts a perpendicular arrangement, where the second atom sits directly on top of the first one. The $Au_2[1-1]$ cluster is 0.46 eV more stable than the

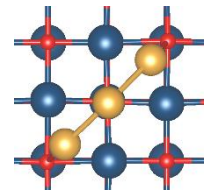
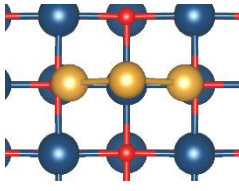
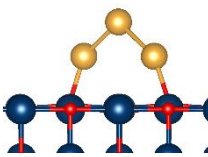
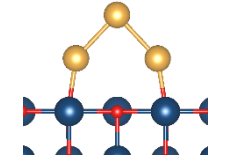
alternative parallel planar structure, where the first Au atom sits on top of two adjacent oxygen atoms ($\text{Au}_2[2-0]$), see Table 3.2.

Table 3.2: Schematic representation of two Au on MgO (001), i.e. Au_2/MgO . Au is represented in yellow, O in red and Mg in blue.

	$\text{Au}_2[1-1]$	$\text{Au}_2[2-0]$
Top		
Side		
ΔE (eV)	0.00	+0.46

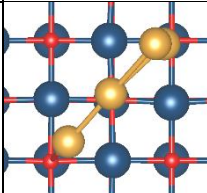
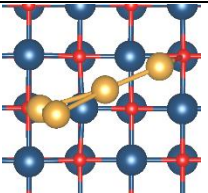
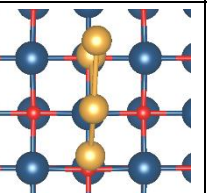
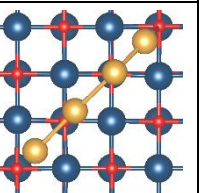
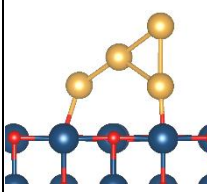
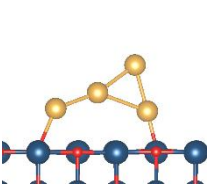
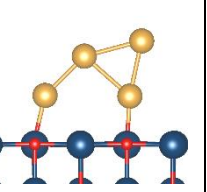
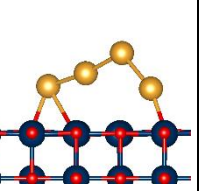
When the cluster grows to accommodate a third atom, the points of contact with the support increases from one to two, both of which are with an oxygen atom. These are bridged by the third Au atom. All structures produced are of a similar geometry, the energy increase being < 0.008 eV. This energy difference is very small, smaller than DFT computational accuracy, producing no discernible energetic difference between the Au_3 structures. While $\text{Au}_3[2-1]_b$ was found using both the build-up and the GA methodology, $\text{Au}_3[2-1]_a$ was not found with GA, this result supported the decision to utilise only the systematic build-up methodology for Au_6 onwards.

Table 3.3: Schematic representation of three Au on MgO (001), i.e. Au₃/MgO. Au is represented in yellow, O in red and Mg in blue.

	Au ₃ [2-1] _a	Au ₃ [2-1] _b
Top		
Side		
ΔE (eV)	0.00	+0.008

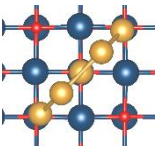
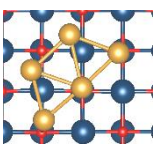
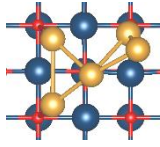
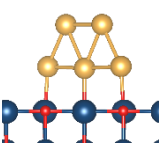
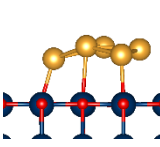
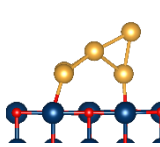
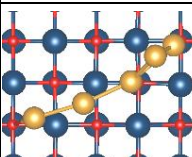
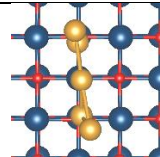
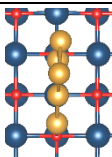
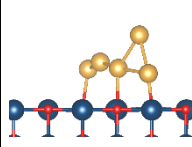
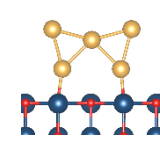
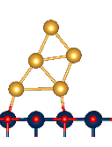
As shown in Table 3.4, the most stable configuration for an Au₄ cluster is a planar, Y-shaped structure, perpendicular to the surface (Au₄[2-2]_a), which was found using only the build-up method. Au₄[2-2]_b was the lowest energy structure found using the GA. Whilst the Au₄[2-2]_b structure was also created by the build-up procedure, it was not determined lower in energy than Au₄[2-2]_a. Structure Au₄[2-2]_c was only found by the GA calculation.

Table 3.4: Schematic representation of four Au on MgO (001), i.e. Au₄/MgO. Au is represented in yellow, O in red and Mg in blue.

	Au ₄ [2-2] _a	Au ₄ [2-2] _b	Au ₄ [2-2] _c	Au ₄ [3-1]
Top				
Side				
ΔE (eV)	0.00	+0.06	+0.10	+0.72

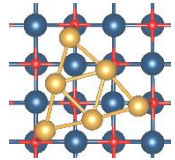
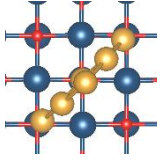
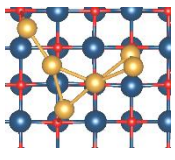
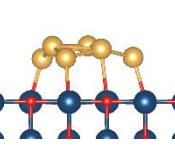
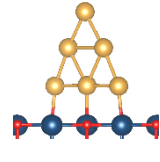
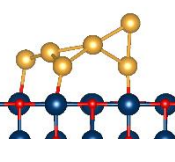
At Au_5 , the lowest energy shape adopted is a trapezium shaped cluster that sits perpendicular to the surface ($Au_5[3-2]_a$). Again, this structure was not found using GA. Structure $Au_5[3-2]_b$ was established to be the lowest in energy from the many structures analysed by the GA method, followed by structure $Au_5[2-2-1]$.

Table 3.5: Schematic representation of five Au on MgO (001), i.e. Au_5/MgO . Au is represented in yellow, O in red and Mg in blue.

	$Au_5[3-2]_a$	$Au_5[5]$	$Au_5[3-1-1]$
Top			
Side			
ΔE (eV)	0.00	+0.03	+0.06
	$Au_5[4-1]$	$Au_5[3-2]_b$	$Au_5[2-2-1]$
Top			
Side			
ΔE (eV)	+0.26	+0.33	+0.50

The GA method was not successful in finding the lowest energy structures for Au_n/MgO where ($n = 3-5$) from the computational time given. Therefore, from Au_6 onwards, structures were only produced via the systematic build-up method. As shown in tables 3.3-3.5, for clusters up to 5 atoms, the perpendicular planar structures are more stable than their parallel planar counterparts. From Au_6 the parallel planar structures become more stable, Figure 3.3. The Au_6 cluster adopts a triangular shaped parallel planar structure as its lowest configuration, see Table 3.6. The perpendicular structure of the same triangular shape being seen to be 0.37 eV less stable.

Table 3.6: Schematic representation of six Au on MgO (001), i.e. Au₆/MgO. Au is represented in yellow, O in red and Mg in blue.

	Au ₆ [6]	Au ₆ [3-2-1]	Au ₆ [4-1-1] _a
Top			
Side			
ΔE (eV)	0.00	+0.37	+0.52

The parallel planar structures persist as the most stable configurations up to Au₁₉, shown in Tables 3.7 to 3.17. Results regarding the energetic and structural properties of the lowest energy clusters for each size are shown in Table 3.18.

Table 3.7: Schematic representation of seven Au on MgO (001), i.e. Au₇/MgO. Au is represented in yellow, O in red and Mg in blue.

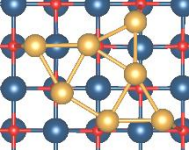
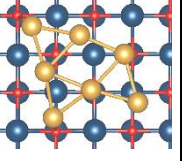
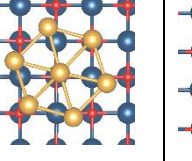
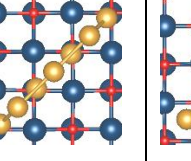
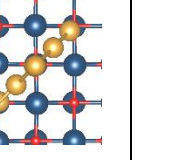
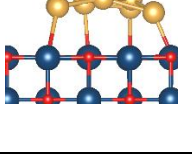
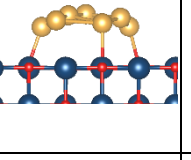
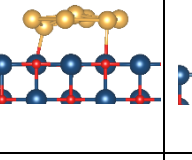
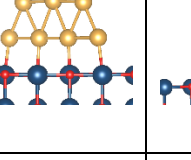
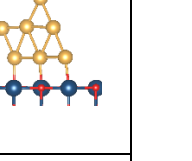
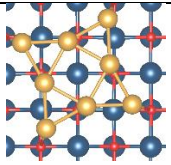
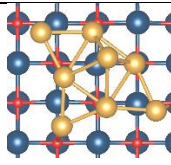
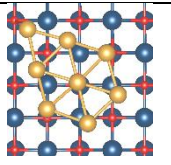
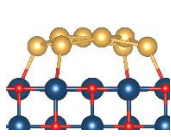
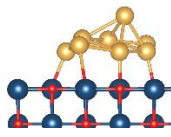
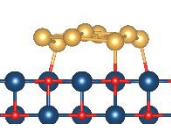
	Au ₇ [7] _a	Au ₇ [7] _b	Au ₇ [7] _c	Au ₇ [4-3]	Au ₇ [3-3-1]
Top					
Side					
ΔE (eV)	0.00	+0.05	+0.32	+0.56	+0.76

Table 3.8: Schematic representation of eight Au on MgO (001), i.e. Au₈/MgO. Au is represented in yellow, O in red and Mg in blue.

	Au ₈ [8] _a	Au ₈ [7-1]	Au ₈ [8] _b
Top			
Side			
ΔE (eV)	0.00	+0.56	+0.63

From Au₈, the perpendicular planar structures are much higher in energy (> 1 eV), therefore, they are not included in the following tables of low energy structures.

Table 3.9: Schematic representation of nine Au on MgO (001), i.e. Au₉/MgO. Au is represented in yellow, O in red and Mg in blue.

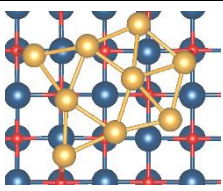
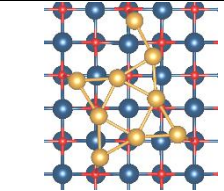
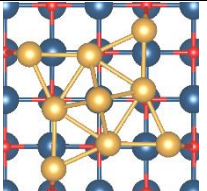
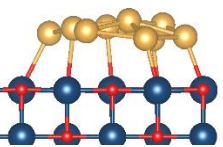
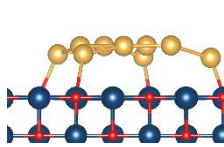
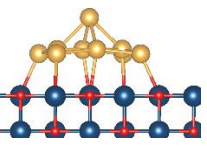
	Au ₉ [9] _a	Au ₉ [9] _b	Au ₉ [8-1]
Top			
Side			
ΔE (eV)	0.00	+0.27	+0.31

Table 3.10: Schematic representation of ten Au on MgO (001), i.e. Au₁₀/MgO. Au is represented in yellow, O in red and Mg in blue.

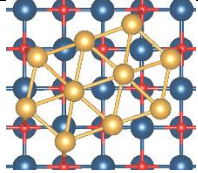
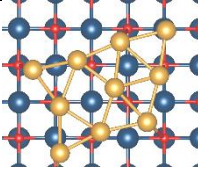
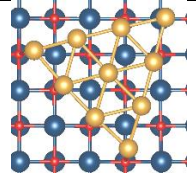
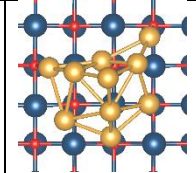
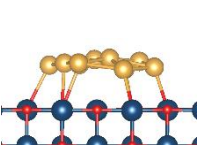
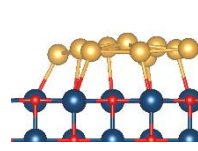
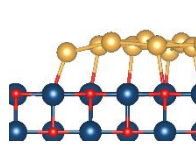
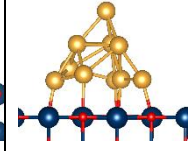
	Au ₁₀ [10] _a	Au ₁₀ [10] _b	Au ₁₀ [10] _c	Au ₁₀ [6-3-1]
Top				
Side				
ΔE (eV)	0.00	+0.36	+0.61	+0.95

Table 3.11: Schematic representation of eleven Au on MgO (001), i.e. Au₁₁/MgO. Au is represented in yellow, O in red and Mg in blue.

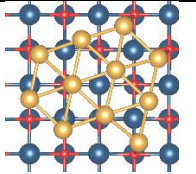
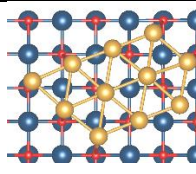
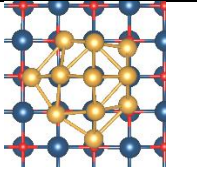
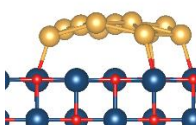
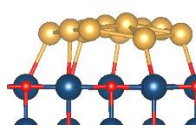
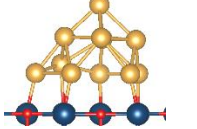
	Au ₁₁ [11] _a	Au ₁₁ [11] _b	Au ₁₁ [6-4-1]
Top			
Side			
ΔE (eV)	0.00	+0.20	+0.90

Table 3.12: Schematic representation of twelve Au on MgO (001), i.e. Au₁₂/MgO. Au is represented in yellow, O in red and Mg in blue.

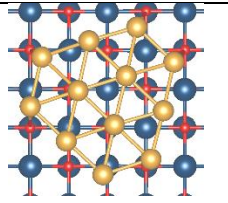
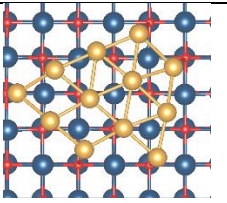
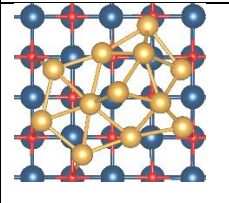
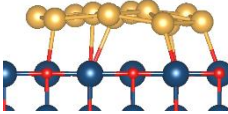
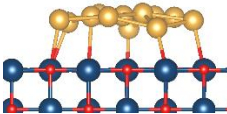
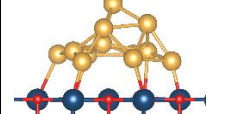
	Au ₁₂ [12] _a	Au ₁₂ [12] _b	Au ₁₂ [9-3]
Top			
Side			
ΔE (eV)	0.00	+0.44	+0.99

Table 3.13: Schematic representation of thirteen Au on MgO (001), i.e. Au₁₃/MgO. Au is represented in yellow, O in red and Mg in blue.

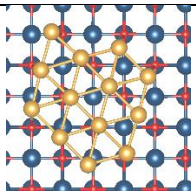
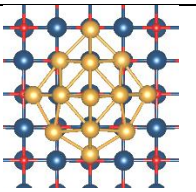
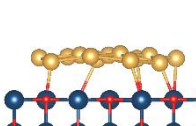
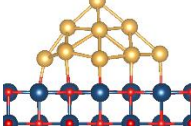
	Au ₁₃ [13]	Au ₁₃ [8-4-1]
Top		
Side		
ΔE (eV)	0.00	+0.49

Table 3.14: Schematic representation of fifteen Au on MgO (001), i.e. Au₁₅/MgO. Au is represented in yellow, O in red and Mg in blue.

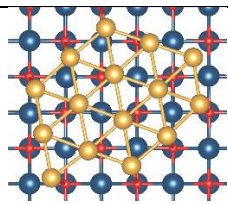
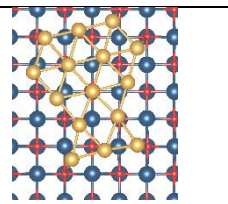
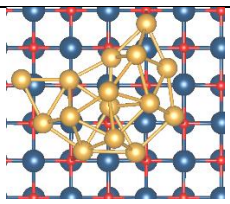
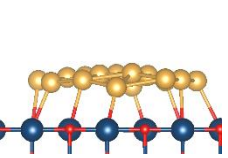
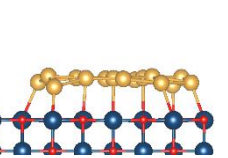
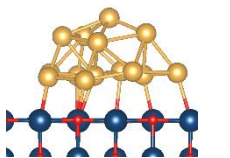
	Au ₁₅ [15] _a	Au ₁₅ [15] _b	Au ₁₅ [10-4-1]
Top			
Side			
ΔE (eV)	0.00	+0.26	+0.88

Table 3.15: Schematic representation of sixteen Au on MgO (001), i.e. Au₁₆/MgO. Au is represented in yellow, O in red and Mg in blue.

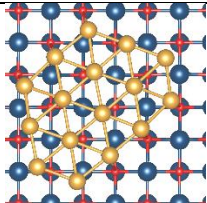
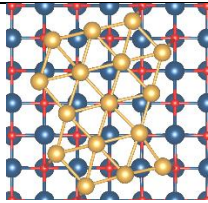
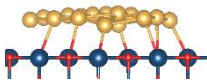
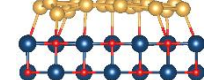
	Au ₁₆ [16] _a	Au ₁₆ [16] _b
Top		
Side		
ΔE (eV)	0.00	+0.51

Table 3.16: Schematic representation of seventeen Au on MgO (001), i.e. Au₁₇/MgO. Au is represented in yellow, O in red and Mg in blue.

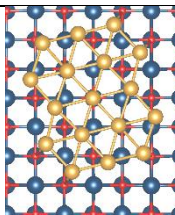
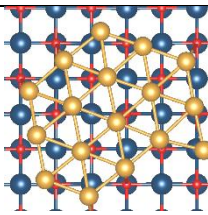
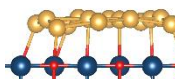
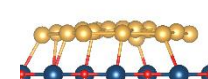
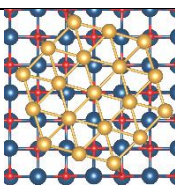
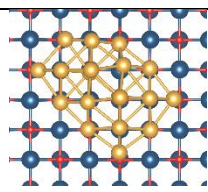
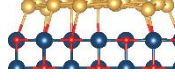
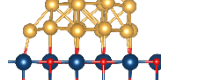
	Au ₁₇ [17] _a	Au ₁₇ [17] _b
Top		
Side		
ΔE (eV)	0.00	+0.14

Table 3.17: Schematic representation of nineteen Au on MgO (001), i.e. Au₁₉/MgO. Au is represented in yellow, O in red and Mg in blue.

	Au ₁₉ [19]	Au ₁₉ [11-6-2]
Top		
Side		
ΔE (eV)	0.00	+1.10

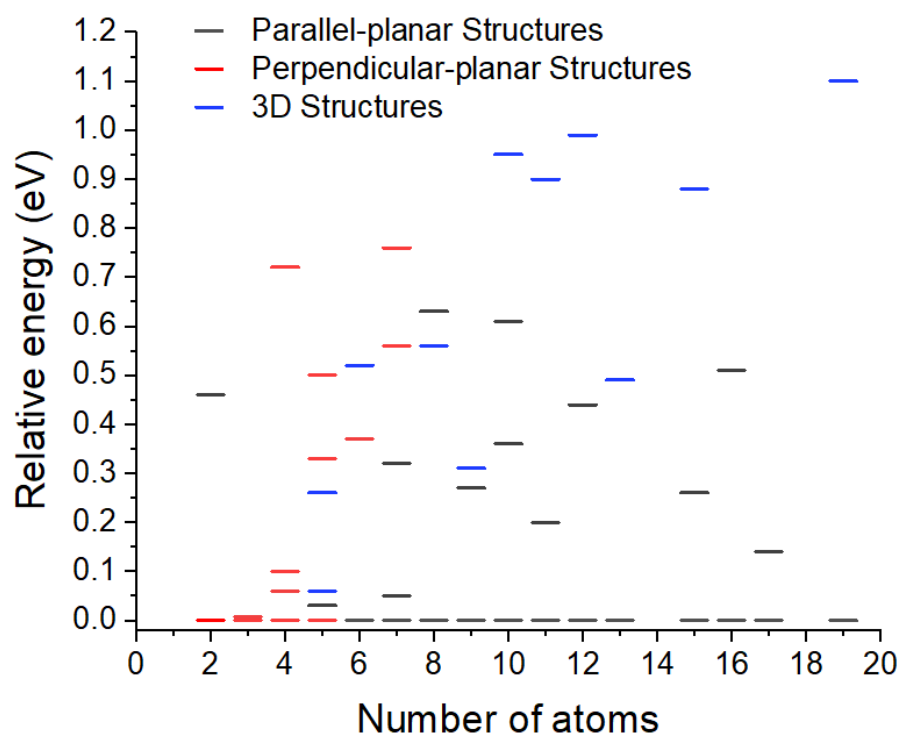


Figure 3.3: Graphical plot of all the Au_n/MgO structures ($n < 20$) found in the tables, by structure type. The relative energy is with respect to the most stable of that size.

Table 3.18: Energetic and structural parameters obtained for the lowest energy Au_n/MgO ($n = 1-19$) systems, where $d\overline{Au - Au}$ is the average Au-Au distance, $d\overline{Au_{n_i} - S}$ is the average interface Au to surface distance and n_i is the number of interface atoms (that is atoms in direct contact with the support). Au interface atoms not close enough to form a bonding interaction until $Au_n = 5$.

n	n_i	$d\overline{Au - Au}$ (Å)	$d\overline{Au_{n_i} - S}$ (Å)	$d\overline{Au - Au}$ at interface (Å)	E_{ads} (eV/atom)	E_{coh} (eV/atom)	E_b (eV/atom)
1	1		2.310		1.37	0.00	1.37
2	1	2.522	2.226		0.83	1.15	1.98
3	2	2.597	2.213		0.94	1.20	2.13
4	2	2.663	2.218		0.87	1.50	2.36
5	3	2.719	2.388	2.773	0.67	1.66	2.33
6	6	2.716	2.705	2.716	0.66	1.89	2.54
7	7	2.708	2.672	2.708	0.67	1.85	2.52
8	8	2.710	2.680	2.710	0.66	1.99	2.65
9	9	2.748	2.71	2.748	0.64	1.98	2.62
10	10	2.746	2.733	2.746	0.60	2.08	2.68
11	11	2.736	2.735	2.736	0.61	2.08	2.69
12	12	2.744	2.752	2.744	0.58	2.17	2.75
13	13	2.743	2.763	2.743	0.58	2.16	2.74
15	15	2.749	2.779	2.749	0.59	2.20	2.79
16	16	2.750	2.788	2.750	0.58	2.24	2.82
17	17	2.751	2.772	2.751	0.58	2.24	2.81
19	19	2.756	2.791	2.756	0.57	2.29	2.86

Structural trends of the lowest energy Au_n structures.

Structural trends of the growing supported Au clusters are determined from calculating the average height difference between the Au clusters and the top layer of the support

$(\overline{dAu_{n_i} - S})$ as well as the average distances between neighbouring atoms within the cluster ($\overline{dAu - Au}$). See Table 3.18 and Figure 3.4.

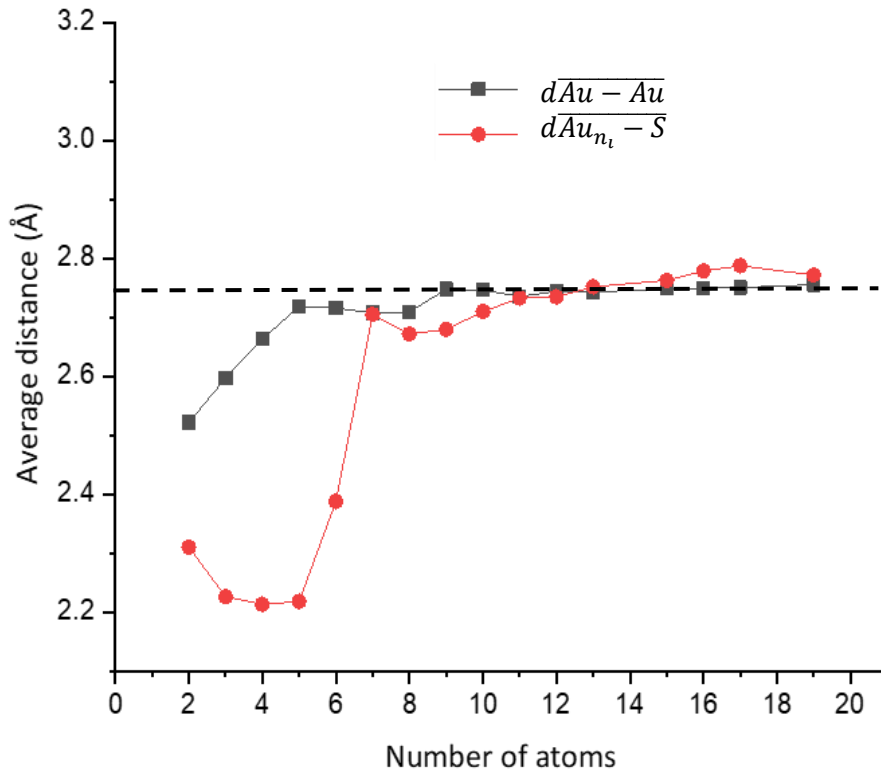


Figure 3.4: Average cluster-support distance and Au-Au distance as a function of the cluster size (n) in Au_n/MgO . The dashed black line represents the Au-Au distance found in an Au-Au monolayer for comparison.

The analysis of structural parameters shows that the cluster-support distance ($\overline{dAu_{n_i} - S}$) of a single Au atom to the support (on top an oxygen) is 2.310 Å, this decreases to 2.20 Å for the Au dimer as shown by Figure 3.4. After Au_5 , the $\overline{dAu_{n_i} - S}$ distance increases and converges to a value between 2.71 Å and 2.79 Å when the arrangement of the cluster changes from perpendicular to parallel to the surface of the support. All Au atoms are at the interface in these clusters and as the number of atoms in contact with the surface (interface

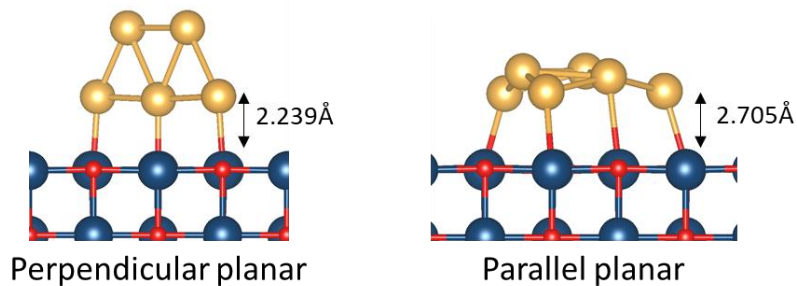


Figure 3.5: Representation of how average cluster-surface distance ($\overline{dAu_{n_i} - S}$) changes with cluster size. Au_5 (left) where the most stable cluster is perpendicular to the surface and Au_6 (right), the most stable structure being parallel to the surface.

atoms) increases. Therefore, the interaction of the cluster with the surface (E_{ads}) is spread across a wider area (interaction with individual Au atoms decreases) and the average cluster surface distance drastically increases, as shown in Figure 3.5.

Generally, when the cluster size increases, the $d_{\text{Au-Au}}$ decreases, as the Au-Au interactions increase and bond lengths decrease. As the cluster grows, the average Au-Au distance tends to the value of an isolated Au monolayer (2.74 \AA). However, the average distance for Au_8 does not follow this trend but the result can be explained by a unique feature of the Au_8 cluster. The most stable structure for Au_8 is shown in Figure 3.6 and displays the (001) facet of the gold atoms in the centre, rather than the typical (111) arrangement seen for all other clusters. When this configuration is adopted it creates slightly shorter bonds between the Au atoms and results in a slightly lower $d_{\text{Au-Au}}$ average.

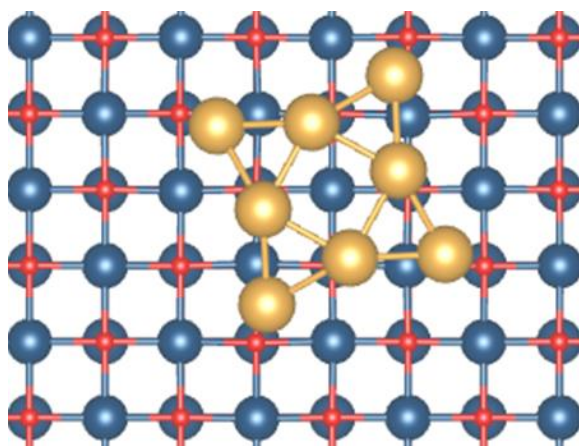


Figure 3.6: Schematic representation of the most stable Au_8 geometry showing the (001) Au configuration unique to this cluster size.

When the planar clusters grow in a (111) hexagonal pattern, this creates what is known as lattice mismatch between the cluster and the surface. Lattice mismatch is where the symmetry of surface is not replicated at the interface of the cluster. Whilst the mismatch would cause strain in the cluster, the adopted (111) motif is still energetically favourable, due to the difference in the surface energies of Au ($\gamma_{(111)} < \gamma_{(001)}$). Greater discussion regarding mismatch can be seen in Chapter 5.

Adsorption, cohesion and binding energies

In terms of the energetic interactions in the Au_n/MgO system, calculations of adsorption energy, binding energy and cohesion energy have been undertaken in line with equations 3.1, 3.2 and 3.3. Starting with single Au atom adsorption on MgO, the adsorption energy was calculated with inclusion of dispersion correction, as 1.37 eV. As many of the previous studies of Au/MgO quote adsorption energy without the use of dispersion correction, the calculation

of single atom adsorption was also performed without dispersion correction for comparison. The value obtained without this correction was 0.81 eV and is similar to values obtained in previous studies, e.g. 0.81 eV by Tada *et al.*,³⁵ 0.87 eV by Jeon *et al.*³⁶ and 0.78 eV by Coquet *et al.*³⁷ with the same GGA functionals used.

In terms of trends observed in adsorption energies, as the cluster size increases, generally the adsorption energy (E_{ads}) of Au clusters on magnesia decreases. The adsorption energy declines rapidly from 1.37 eV (for Au₁) and converges around 0.57 eV, see Figure 3.7. The planar growth of the Au clusters is reflected in convergence of the adsorption energy. Each atom added to the cluster joins to the corner of the existing Au cluster and is in contact with the support, therefore the adsorption energy decreases fairly linearly with cluster growth.

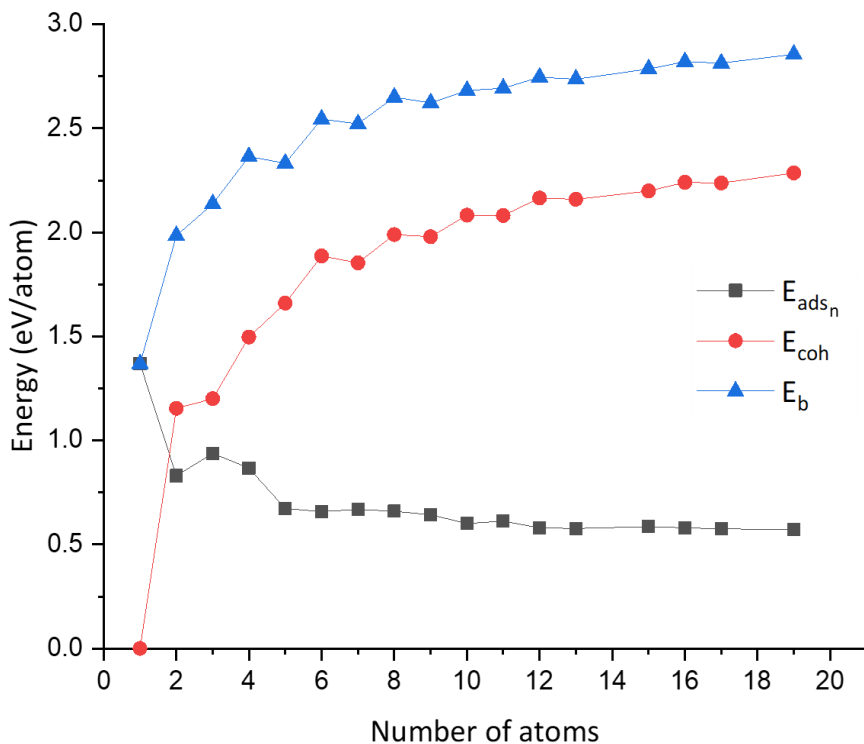


Figure 3.7: Graph to show adsorption energy per atom (E_{ads_n}), binding (E_b) and cohesion (E_{coh}) energies of Au clusters with number of atoms (n) on MgO(001).

Both the cohesion energy (E_{coh}) and the binding energy (E_b) increase with the number of Au atoms on the magnesia, displaying an opposite trend to that of the E_{ads} . With increasing cluster size, the cohesion energy (E_{coh}) increases toward the bulk cohesive energy of gold, calculated as 3.63 eV/atom. This value is similar to that found experimentally (3.81 eV/atom)³⁸ and computationally (3.73 eV/atom) for bulk gold.³⁹ The Au₂ cluster has a measured cohesion energy of 1.15 eV, this is comparable to the experimental cohesion

energy of 1.16 eV quoted by Kittel,³⁸ and the computationally calculated one (1.16 eV) using a correlation-consistent basis set in DFT (rather than plane-waves) obtained by Bun *et al.*³⁹

The results in Figure 3.7 supports the conclusion that as the cluster grows, the interactions within the cluster increase while the cluster-support interaction decreases. Supported clusters with high cohesion energy have a morphology close to their optimum structure in the gas phase. This means that the structures are either weakly influenced by the support, or the interaction is weakened by the mismatch, i.e. difference in the atomic distances and symmetry between the cluster and the surface adsorption sites. Despite the symmetry mismatch between the square magnesia surface and the hexagonal Au cluster, addition of Au atoms to the cluster does not affect the average strength of the interaction of the Au atoms with the surface, while the cohesion energy does not indicate any significant distortion of the metal cluster. Therefore, planar arrangements of the Au atoms are stabilised on MgO. These structures are also stable in gas phase according to different computational studies, but only for cluster sizes up to around 13⁴⁰ or 15⁴¹ atoms.

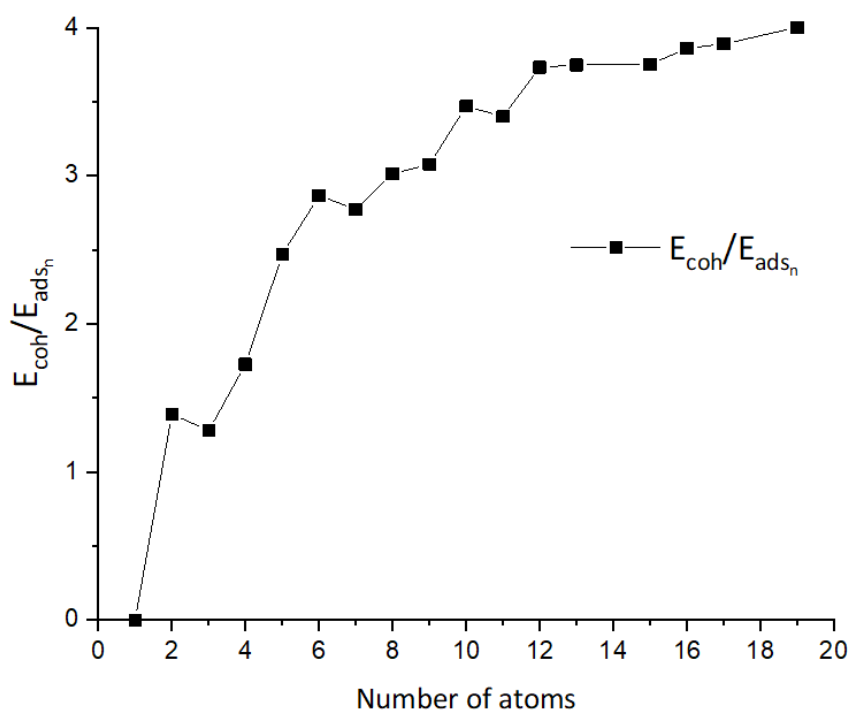


Figure 3.8: Graph to show ratio of cohesive (E_{coh}) and adsorption per atom (E_{ads_n}) energies.

The ratio of cohesion energy (E_{coh}) to adsorption energy per atom has been calculated to help ascertain which interactions are dominant in the system, see Figure 3.8. A high ratio denotes that the cluster structure is controlled by the Au-Au interactions, while a low ratio indicates a stronger interaction of Au atoms with the surface than to each other. The

dominance of E_{coh} , indicates that while small Au clusters are more influenced by the cluster-support interactions, having a lower E_{coh}/E_{ads_n} ratio as seen in Figure 3.8, the larger the cluster size, the greater the influence of the E_{coh} . However, when the E_{coh}/E_{ads_n} ratio was compared to Au clusters on another support such as carbon,⁴² this ratio is relatively low and partially explains the planar nature of the structures.

Electronic charge analysis

Bader charges

A strong adsorption of metal clusters on supports is commonly associated with a distortion in their electronic structure, e.g. subtracting or adding electrons into the metal band structure. These distortions have implications for the cluster morphology and stability, as well as the catalytic activity. Therefore, changes in the electronic structure were analysed and electron transfer between the cluster and the surface was investigated using the Bader population (atoms in molecules) analysis.

Table 3.19: Summary of the average charge analysis on the Au_n/MgO system.

n	Charge transfer (e per atom)	n	Charge transfer (e per atom)
1	-0.24	10	-0.08
2	-0.13	11	-0.09
3	-0.15	12	-0.08
4	-0.12	14	-0.08
5	-0.12	15	-0.08
6	-0.11	16	-0.08
7	-0.10	17	-0.08
8	-0.09	19	-0.07
9	-0.09		

The results from the charge analysis showed a reduction (gain of electrons) of the Au clusters on the magnesium oxide surface. The degree of charge transfer per atom generally decreases with increasing cluster size. The biggest charge transfer per Au atom was found for a single Au ad-atom with a negative partial charge of -0.24 e. This is primarily taken from the oxygen atom at the interface, which shows a charge difference of $+0.19$ e compared to the surrounding oxygen atoms. The average charge of the Au atoms decreases to -0.13 e for the Au dimer and in this case, the Au atom at the interface is only charged by -0.05 e, significantly less than the second Au atom on top of the interface atom, which has a charge of -0.20 e. This is dissimilar to the observations Au_3 , where the interface atoms are more negatively

charged with -0.18 e and -0.19 e. The top Au atom only showing a charge of -0.07 e, the average for Au_3 being a charge of -0.15 e. There is a weaker interaction of the Au cluster with the surface as the cluster grows, resulting in increasing cluster size decreasing the average charge of the Au atoms to -0.07 e, as seen in the case of Au_{19} . As the clusters get bigger, the interactions between Au atoms are stronger (E_{coh}) than the interaction formed by the adsorption of the gold to the surface (E_{ads}). This results in a reduction in the charge transfer from the surface to the Au cluster. Additionally, the charge of specific Au atoms within a cluster is mainly dependent on the number of neighbouring Au atoms, i.e. atoms at the corners and edges of the cluster with lower coordination are more negatively polarized than highly coordinated atoms in the centre of the cluster. It is of note, that there is no distinct correlation between the height of the cluster from the surface and the partial charges on the Au atoms as previously described by Paccioni.⁴³

Density of states (DOS) and Crystal Orbital Hamilton Populations (COHP)

Density of states (DOS), have been used to characterise electronic properties, and in particular, orbital interactions that lead to bonding interactions between the Au and MgO in Au/MgO systems. DOS have been used in combination with a Crystal Orbital Hamilton

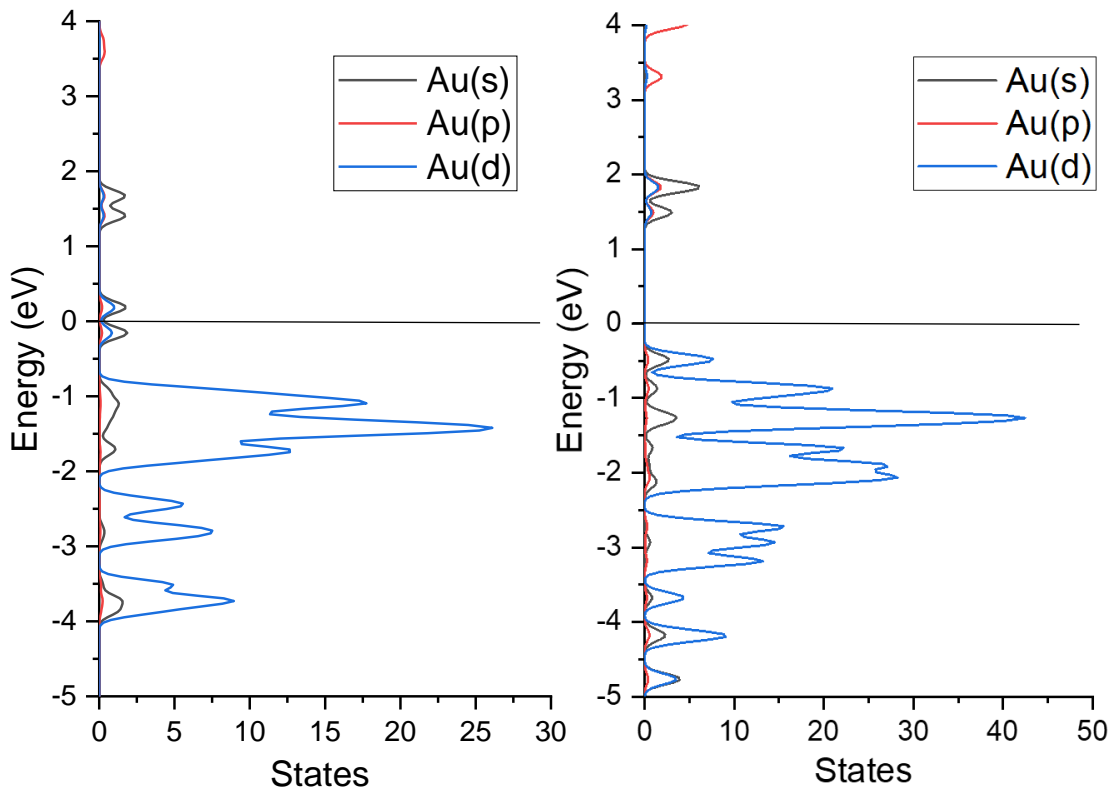


Figure 3.9: Projected DOS of unsupported Au_3 (right) and Au_6 (left) clusters, Energy relative to the Fermi energy, marked by the black line.

Population analysis (COHP) to help distinguish the states contributing to the stabilization of the structure.⁴⁴

Initially, the electronic structure of unsupported, isolated Au clusters was analysed in order to apply the results to the discussion of the supported cluster structures. The cluster sizes chosen for analysis were Au₃ and Au₆, as these sizes provide information relating to both odd and even numbered clusters. The frontier bands (highest occupied and lowest unoccupied) in the isolated Au clusters, Au₃ and Au₆, have s,d hybrid orbital character, evident from the mixing of the peaks in the DOS, as seen in Figure 3.9. In odd-numbered clusters, e.g. Au₃, the highest occupied band is dominated by contributions from the s states of the Au atoms, whereas the occupied orbitals below are dominated by d contributions. Even-numbered clusters have a d-dominated occupied band while the lowest unoccupied band is s-dominated.

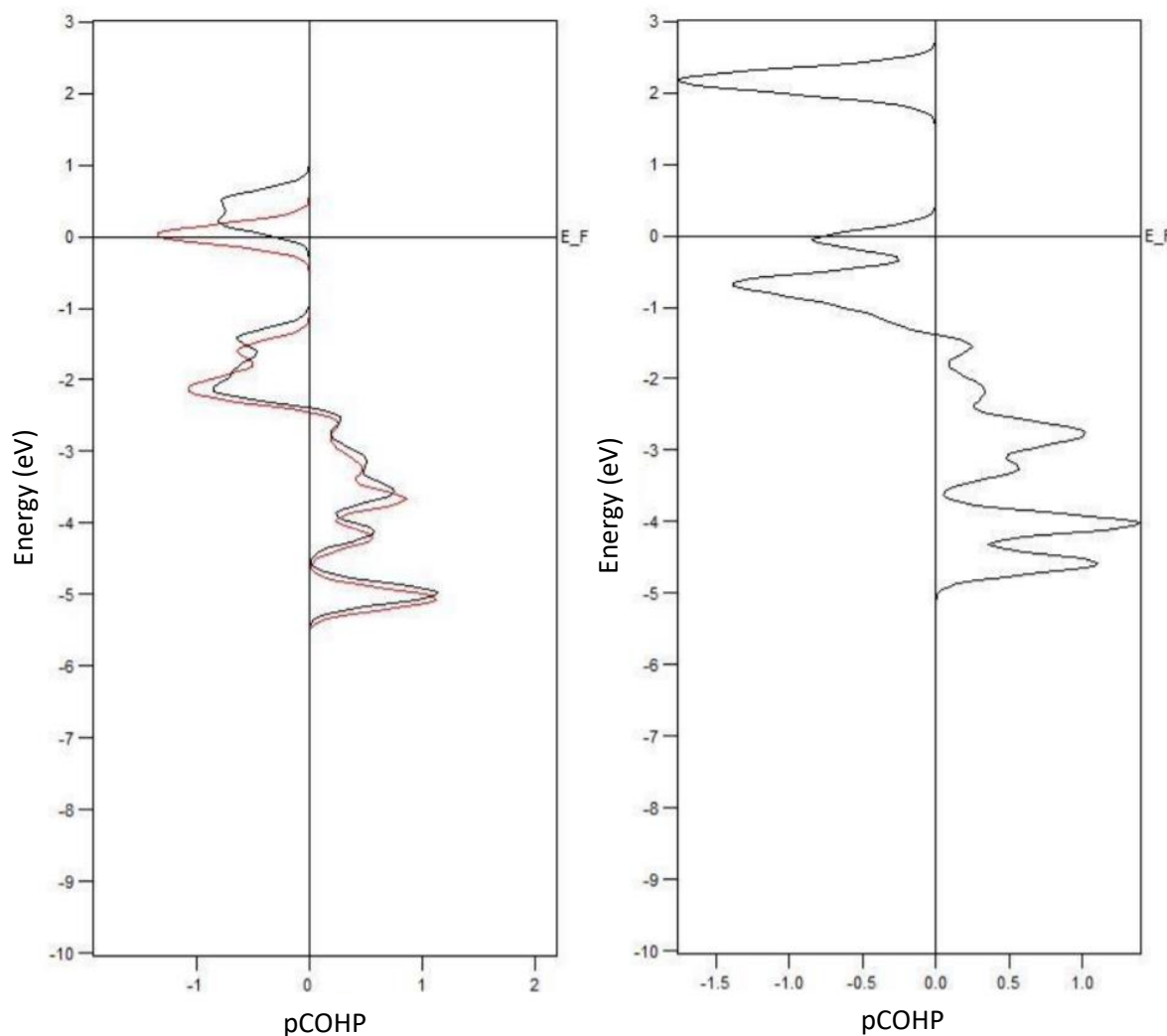


Figure 3.10: (left) Average pCOHP (Au-Au) for Au₃; spin1 (red) and spin 2 (black), (right) Average pCOHP (Au-Au) for Au₆

Considering the electron configuration of Au ($[\text{Xe}] 4f^{14} 5d^{10} 6s^1$), the d-orbitals will be occupied, and the s-orbitals will be half occupied. Therefore, as seen in Figure 3.10 by the pCOHP of unsupported Au clusters, most of the antibonding states are occupied.

The density of states (DOS) of the naked MgO surface is shown in Figure 3.11 and reveals that the valence band has predominantly O 2p character, with very little mixing of Mg states. This indicates the electronic density is donated into the O p orbitals in the formation of the bond and displays the ionic character of this bond. The magnesia band gap, the energy difference between the valence and the conduction band, is approximately 3.3 eV, which is a typical value obtained with DFT computational methods.⁴⁵ This value is consistent with its nature as an insulative material but is smaller than the value expected from experiment (7.7 eV).⁴⁶ The conduction band consists of Mg 2s and 2p states with little mixing of O 2p states. The pCOHP (Mg-O), Figure 3.11, indicates bonding character for the entire valence band and antibonding character for the complete conduction band.

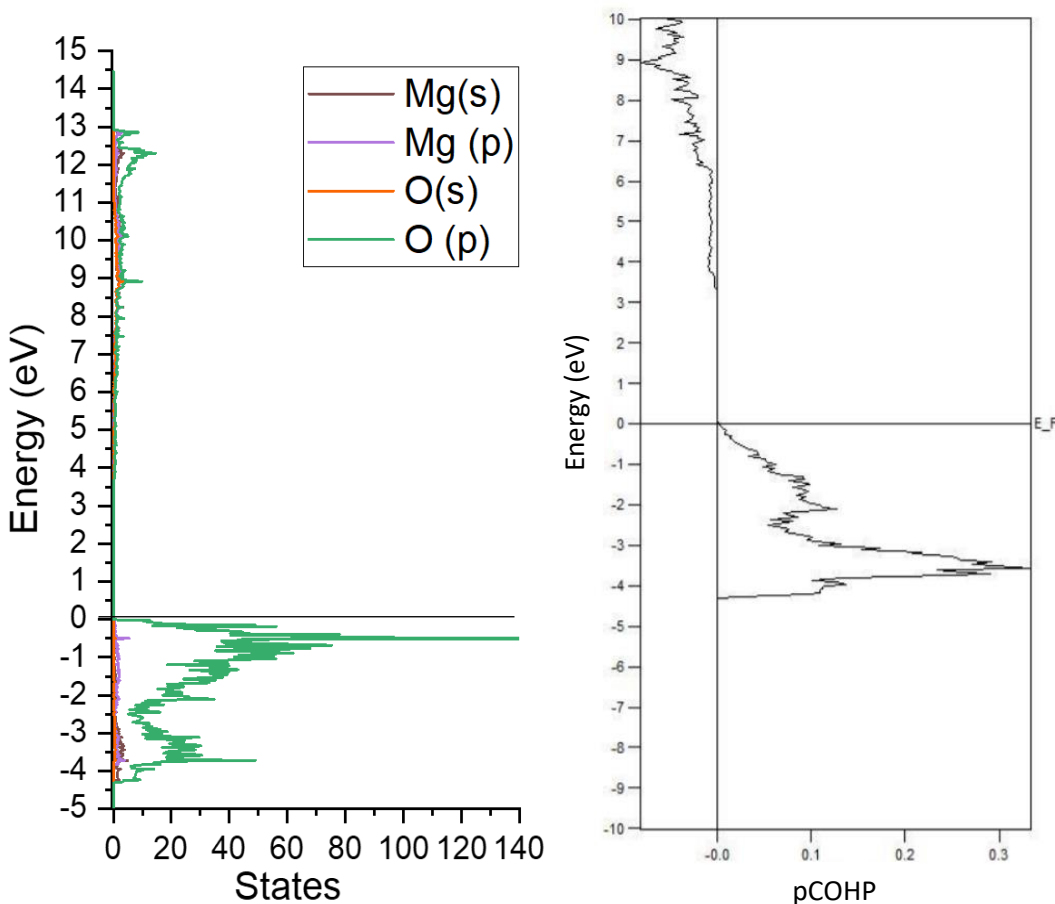


Figure 3.11: (left) pDOS of MgO(001); Mg(s) orbitals (red), Mg(p) orbitals (black), O(s) orbitals (blue), O(p) orbitals (yellow). (right) Average pCOHP (Mg-O) of MgO; pairs within 3.0 Å.

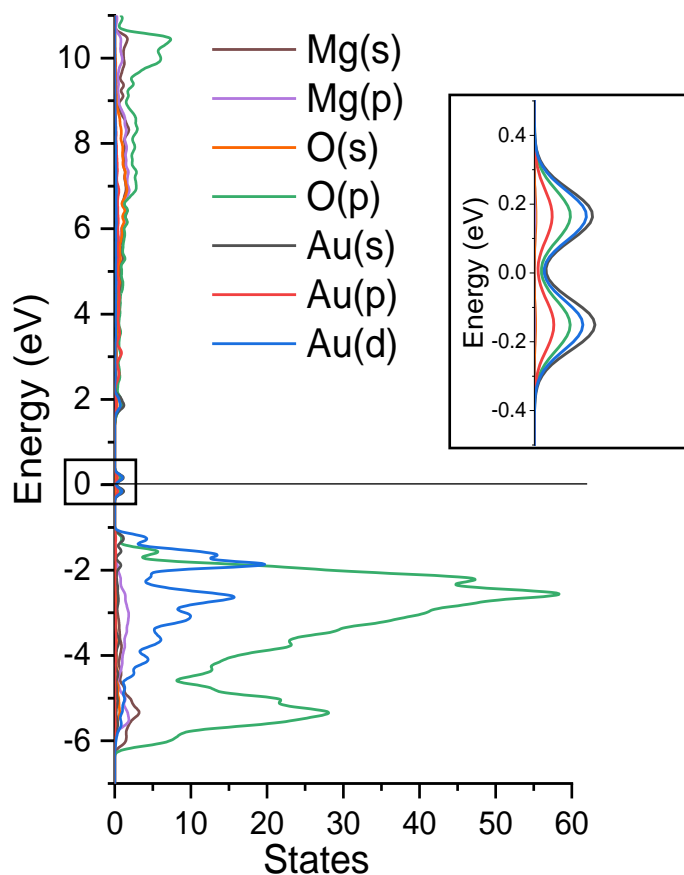


Figure 3.12: pDOS of Au_3/MgO , Energy relative to fermi energy, marked with a black line (0eV), inset shows the state around the Fermi level (-0.4 to 0.4 eV)

In the pDOS (projected DOS) of the Au_3/MgO system, Figure 3.12, the Au d-states are mainly below the Fermi energy indicating that they are occupied, whilst there are small peaks associated with Au s-states both sides of the Fermi energy, indicating that the Au s-states are partially occupied. The band gap is reduced to 1 eV with the emergence of an Au states at the Fermi energy, with both s and d-orbitals mixing implying hybridisation. There is overlap in the valence band between mainly the d-states of the Au and the O p-states, showing some bonding interaction between Au and O. While this indicates that the formation of Au–O bonds is favoured, the pCOHP (Figure 3.13) implies that many antibonding Au–O and Au–Au states are populated. As a result of the bonding, electron density is shifted from the p-orbitals of the surface oxygen atoms into the new bands giving a net transfer of charge from the surface to the cluster.

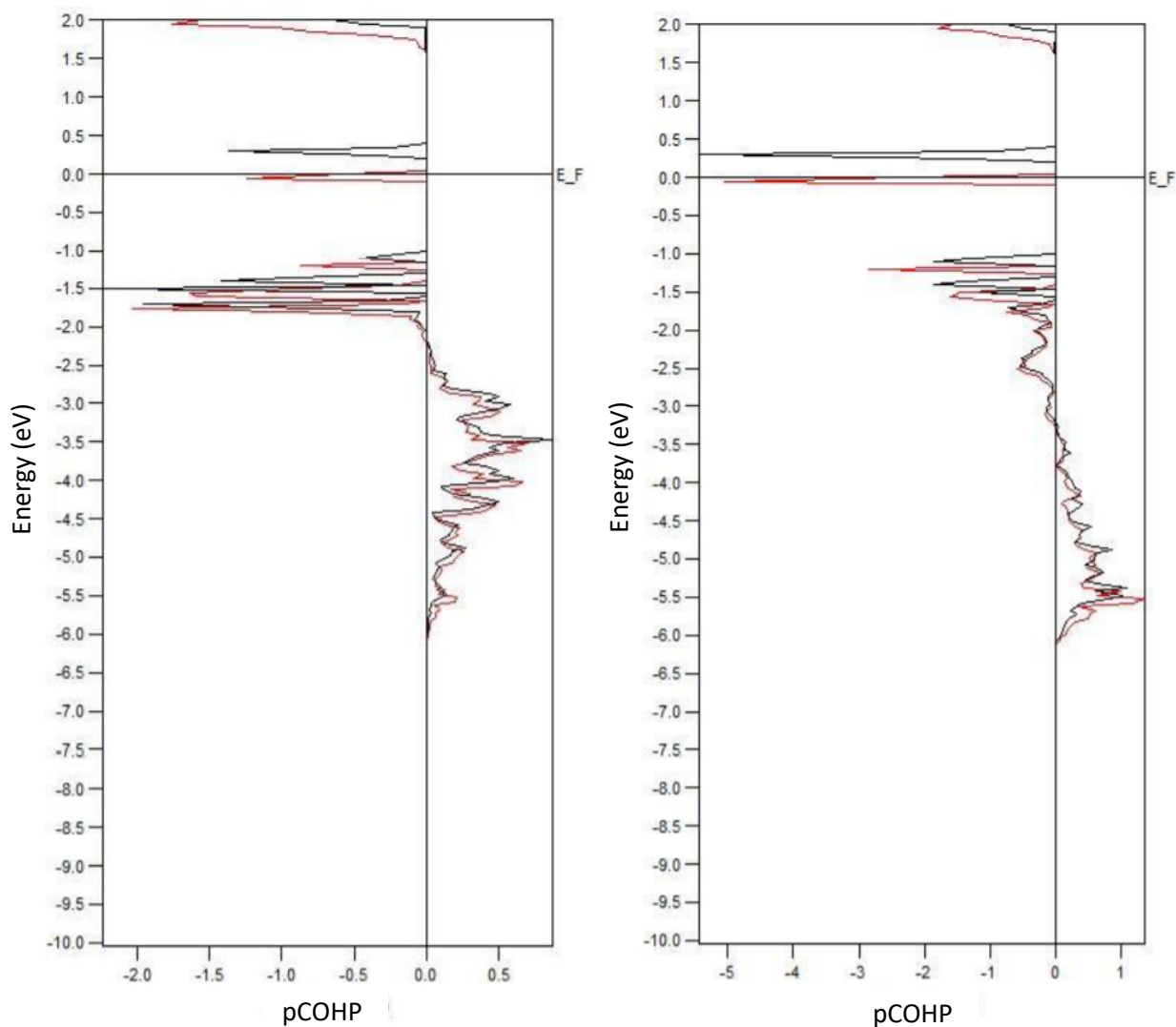


Figure 3.13: Average pCOHP (Au-Au, within 4Å) for Au₃/MgO, (right) Average pCOHP (Au-O, within 4Å) for Au₃/MgO; spin 1 (red) and spin 2 (black)

As in the case of an isolated Au₃ cluster, the highest occupied orbital has larger contribution from the Au 6s orbitals than the 5d orbitals of the Au atoms. According to the pCOHP calculation, these states are antibonding with respect to the Au-O as well as the Au-Au interactions. This indicates that the magnesia surface can offer only limited stabilisation for odd-numbered Au clusters compared with the isolated clusters and explains the odd-even oscillation of the stability retained for the adsorbed species, this is discussed further in Chapter 4.

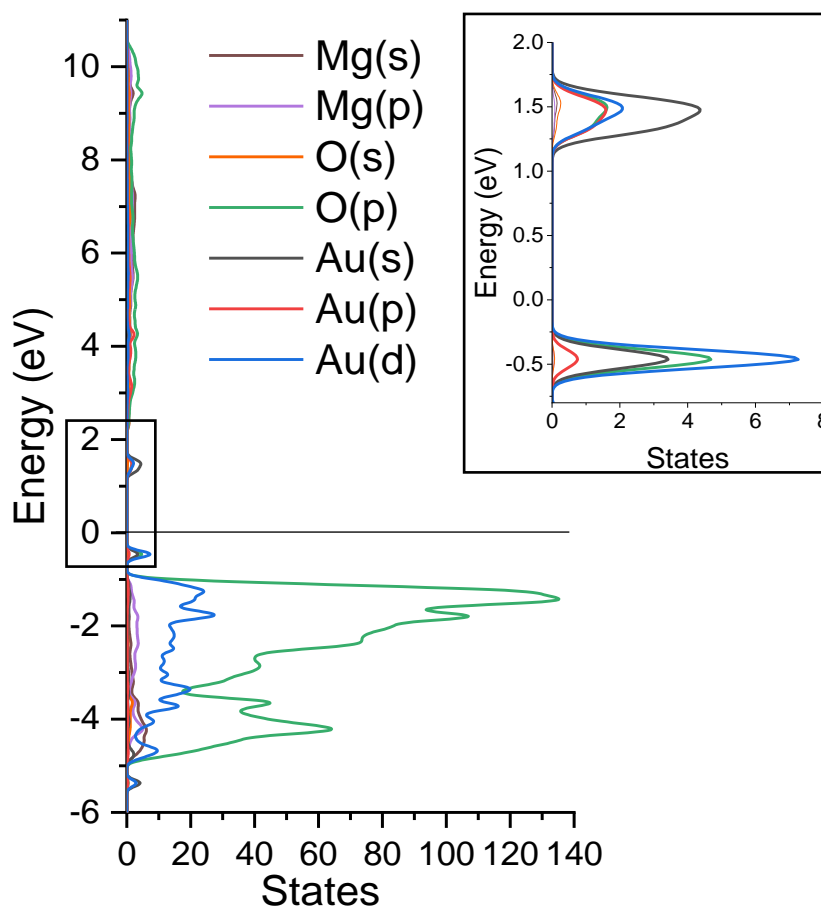


Figure 3.14: pDOS of Au_6/MgO ; Energy relative to Fermi energy, marked by the black line (0eV), inset shows the density of the orbitals between -1.0 and 2.0 eV.

Similar conclusions can be made when analysing $Au_6/MgO(001)$, Figure 3.14 and 3.15. The valance band mainly consists of O p states and Au d-states, however, the highest occupied state in the DOS, 0.6 eV below the Fermi energy, is made up of Au s and d-states, and the lowest unoccupied peak consists of mainly Au s-states, showing that less of the s-states are occupied. This suggests pairing interactions induced in the even number cluster. The shift downwards in energy for the highest occupied peak is also consistent with this conclusion, as the pairing would reduce the energy of the orbital. As seen for Au_3/MgO , they are strongly antibonding with respect to the Au-Au and Au-O interactions.

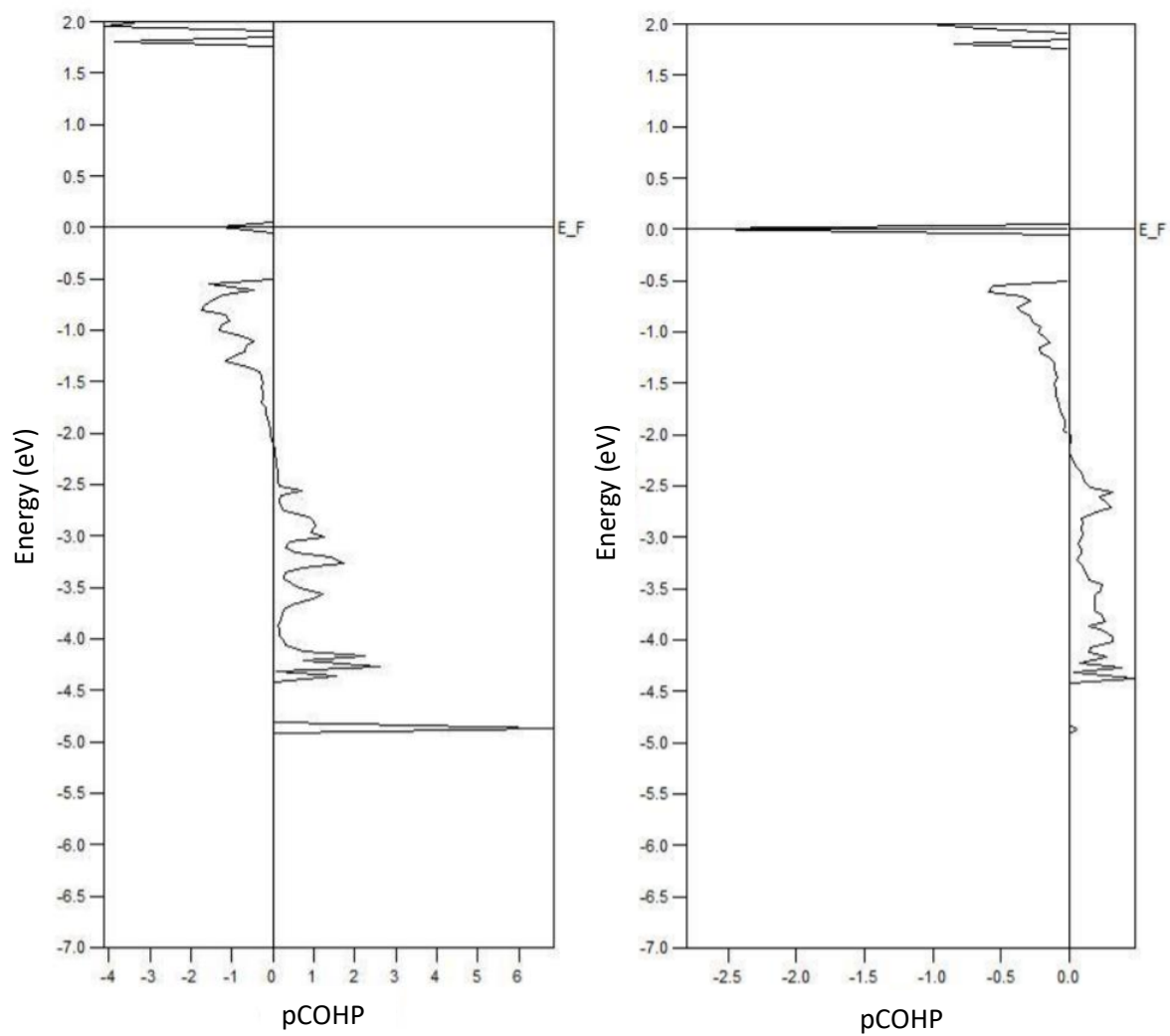


Figure 3.15: (left) Average pCOHP (Au-Au, within 4\AA) for Au_6/MgO , (right) Average pCOHP (Au-O, within 4\AA) for Au_6/MgO .

Conclusions

In conclusion, a systematic DFT study on Au_n nanoparticles ($n = 1-19$) supported on MgO (001) was carried out to determine the shapes and position of the most stable Au_n/MgO systems. The results showed that the most stable clusters below 6 atoms are planar and sit perpendicular to the support, above 6 atoms the lowest energy structures are planar and parallel to the support. The structural and electronic properties of supported Au nanoparticles are highly influenced by the MgO support. The effect of the support on cluster shape is exhibited by the (001) features of clusters of Au_7/MgO and Au_8/MgO , showing that surface interactions lead to distortion in the shape of the Au cluster. This results in changes to the cluster geometry to accommodate the interactions with the oxide support. However, as cluster size increases the interaction between the cluster atoms and the surface weakens (lower E_{ads}), while the interactions between Au atoms in the cluster strengthen (higher E_{coh}). The stronger cohesion between Au atoms as the cluster grows is also shown by the reduced anti-bonding character of the Au-Au bonds in Au_6/MgO when compared with the Au_3/MgO system. This decreasing E_{ads} and increased E_{coh} results in the interfacial layer of the cluster retaining a (111) epitaxy and hexagonal Au structure, while cluster growth is still on the interface. The charge distribution analysis found that the Au clusters on magnesia have negative partial charges which stabilises planar Au clusters. That being said, the shape of the metal clusters in general, may be dependent on more than only the relative strength of the metal-metal interactions and the metal-surface interactions. Additional considerations include cluster-surface mismatch and surface energies, further discussed in Chapter 5.

References

1. Berg, R. van den *et al.* Structure sensitivity of Cu and CuZn catalysts relevant to industrial methanol synthesis. *Nat. Commun.* **7**, 20457–20465 (2016).
2. Frost, J. C. Junction effect interactions in methanol synthesis catalysts. *Nature* **334**, 577–580 (1988).
3. Chang, K. J. & Cohen, M. L. High-pressure behavior of MgO: Structural and electronic properties. *Phys. Rev. B* **30**, 4774–4781 (1984).
4. Jian-Zhou, Zhao, Lai-Yu Lu, Xiang-Rong Chen, Y.-L. First-principles calculations for elastic properties of the rocksalt structure MgO. *Phys. B Condens. Matter* **387**, 245–249 (2007).
5. Watson, G. W., Kelsey, E. T., De Leeuw, N. H., Harris, D. J. & Parker, S. C. Atomistic simulation of dislocations, surfaces and interfaces in MgO. *J. Chem. Soc* **92**, 433–438 (1996).
6. Henry, C. R. Surface studies of supported model catalysts. *Surf. Sci. Rep.* **31**, 231–325 (1998).
7. Julkapli, N. M. & Bagheri, S. Magnesium oxide as a heterogeneous catalyst support. *Rev. Inorg. Chem.* **36**, 1–41 (2016).
8. Tomska-Foralewska, I., Zieliński, M., Pietrowski, M., Przystajko, W. & Wojciechowska, M. Iridium supported on MgF₂–MgO as catalyst for CO oxidation. *Catal. Today* **176**, 263–266 (2011).
9. Wu, M. *et al.* Catalytic Performance of MgO-Supported Co Catalyst for the Liquid Phase Oxidation of Cyclohexane with Molecular Oxygen. *Catalysts* **7**, 155 (2017).
10. Bajdich, M., Nørskov, J. K. & Vojvodic, A. Surface Energetics of Alkaline-Earth Metal Oxides: Trends in Stability and Adsorption of Small Molecules. *Phys. Rev. B* **91**, 155401 (2015).
11. Cho, Y. *et al.* First-principles study on secondary electron emission of MgO surface. *J. Appl. Phys.* **101**, 083710 (2007).
12. Wu, P., Cao, G., Tang, F. & Huang, M. Electronic and magnetic properties of transition metal doped MgO sheet: A density-functional study. *Comput. Mater. Sci.* **86**, 180–185 (2014).

13. Hutchings, G. Vapor phase hydrochlorination of acetylene: Correlation of catalytic activity of supported metal chloride catalysts. *J. Catal.* **96**, 292–295 (1985).
14. Haruta, M. Gold as a novel catalyst in the 21st century: Preparation, working mechanism and applications. *Gold Bull.* **37**, 27–36 (2004).
15. Wang, Z., Xu, C. & Wang, H. A Facile Preparation of Highly Active Au/MgO Catalysts for Aerobic Oxidation of Benzyl Alcohol. *Catal. Letters* **144**, 1919–1929 (2014).
16. Hughes, M. D. *et al.* Tunable gold catalysts for selective hydrocarbon oxidation under mild conditions. *Nature* **437**, 1132–1135 (2005).
17. Zhou, X., Xu, W., Liu, G., Panda, D. & Chen, P. Size-Dependent Catalytic Activity and Dynamics of Gold Nanoparticles at the Single-Molecule Level. *J. Am. Chem. Soc.* **132**, 138–146 (2010).
18. Schubert, M. M., Venugopal, A., Kahlich, M. J., Plzak, V. & Behm, R. J. Influence of H₂O and CO₂ on the selective CO oxidation in H₂-rich gases over Au/ α -Fe₂O₃. *J. Catal.* **222**, 32–40 (2004).
19. Hvolbaek, B. *et al.* Catalytic activity of Au nanoparticles. *Nanotoday* **2**, (2007).
20. Medford, A. J. *et al.* From the Sabatier principle to a predictive theory of transition-metal heterogeneous catalysis. *J. Catal.* **328**, 36–42 (2015).
21. Lopez, N. *et al.* On the origin of the catalytic activity of gold nanoparticles for low-temperature CO oxidation. *J. Catal.* **223**, 232–235 (2004).
22. Cargnello, M. *et al.* Control of Metal Nanocrystal Size Reveals Metal-Support Interface Role for Ceria Catalysts. *Science* (80-.). **341**, 771–773 (2013).
23. Zhang, D.-N., Zhao, L., Wang, J. & Li, Y.-L. Electronic structures and the stability of MgO surface: Density functional study. *Surf. Rev. Lett.* **22**, 1550037 (2015).
24. Monkhorst, H. & Pack, J. Special points for Brillouin zone integrations. *Phys. Rev. B* **13**, 5188–5192 (1976).
25. Kresse, G. & Hafner, J. *Ab initio* molecular dynamics for liquid metals. *Phys. Rev. B* **47**, 558–561 (1993).
26. Kresse, G. & Furthmüller, J. Efficient iterative schemes for *ab initio* total-energy calculations using a plane-wave basis set. *Phys. Rev. B* **54**, 11169–11186 (1996).
27. Kresse, G. & Joubert, D. From ultrasoft pseudopotentials to the projector

- augmented-wave method. *Phys. Rev. B* **59**, 1758–1775 (1999).
28. Perdew, J., Burke, K. & Ernzerhof, M. Generalized Gradient Approximation Made Simple. *Phys. Rev. Lett.* **77**, 3865–3868 (1996).
 29. Grimme, S., Antony, J., Ehrlich, S. & Krieg, H. A consistent and accurate ab initio parametrization of density functional dispersion correction (DFT-D) for the 94 elements H-Pu. *J. Chem. Phys.* **132**, 154104–1007 (2010).
 30. Blöchl, P. E. Projector augmented-wave method. *Phys. Rev. B* **50**, 17953–17979 (1994).
 31. Tang, W., Sanville, E. & Henkelman, G. A grid-based Bader analysis algorithm without lattice bias. *J. Phys. Condens. Matter* **21**, 084204 (2009).
 32. Ferrando, R. & Fortunelli, A. Diffusion of adatoms and small clusters on magnesium oxide surfaces. *J. Phys. Condens. Matter* **21**, 264001 (2009).
 33. Yulikov, M., Sterrer, M., Risse, T. & Freund, H.-J. Gold atoms and clusters on MgO(100) films; an EPR and IRAS study. *Surf. Sci.* **603**, 1622–1628 (2009).
 34. Shayeghi, A., Götz, D., Davis, J. B. A., Schäfer, R. & Johnston, R. L. Pool-BCGA: a parallelised generation-free genetic algorithm for the ab initio global optimisation of nanoalloy clusters. *Phys. Chem. Chem. Phys.* **17**, 2104–2112 (2015).
 35. Tada, K., Koga, H., Okumura, M. & Tanaka, S. Estimation of spin contamination error in dissociative adsorption of Au₂ onto MgO(0 0 1) surface: First application of approximate spin projection (AP) method to plane wave basis. *Chem. Phys. Lett.* **701**, 103–108 (2018).
 36. Jeon, J., Yu, B. D. & Hyun, S. Surface strain effects on the adsorption and the diffusion of Au atoms on MgO(001) surfaces. *J. Korean Phys. Soc.* **69**, 1776–1780 (2016).
 37. Coquet, R., Hutchings, G. J., Taylor, S. H. & Willock, D. J. Calculations on the adsorption of Au to MgO surfaces using SIESTA. *J. Mater. Chem.* **16**, 1978–1988 (2006).
 38. Kittel, C. *Introduction to solid state physics*. (Wiley, 2005).
 39. Chan, B. & Yim, W.-L. Accurate Computation of Cohesive Energies for Small to Medium-Sized Gold Clusters. *J. Chem. Theory Comput.* **9**, 1964–1970 (2013).
 40. Xiao, L., Tollberg, B., Hu, X. & Wang, L. Structural study of gold clusters. *J. Chem.*

Phys. **124**, 114309 (2006).

41. Xiao, L. & Wang, L. From planar to three-dimensional structural transition in gold clusters and the spin-orbit coupling effect. *Chem. Phys. Lett.* **392**, 452–455 (2004).
42. Engel, J., Francis, S. & Roldan, A. The influence of support materials on the structural and electronic properties of gold nanoparticles – a DFT study. *Phys. Chem. Chem. Phys.* **21**, 19011–19025 (2019).
43. Pacchioni, G. Electronic interactions and charge transfers of metal atoms and clusters on oxide surfaces. *Phys. Chem. Chem. Phys.* **15**, 1737–1757 (2013).
44. Dronskowski, R. & Blöchl, P. E. Crystal orbital Hamilton populations (COHP): energy-resolved visualization of chemical bonding in solids based on density-functional calculations. *J. Phys. Chem.* **97**, 8617–8624 (1993).
45. Nourozi, B. *et al.* The electronic and optical properties of MgO mono-layer: Based on GGA-mBJ. *Results Phys.* **12**, 2038–2043 (2019).
46. Roessler, D. M. & Walker, W. C. Electronic spectrum and ultraviolet optical properties of crystalline MgO. *Phys. Rev.* **159**, 733–738 (1967).

Chapter 4

Growth of Au_n on MgO surfaces – Ostwald ripening

Introduction

This chapter presents a DFT computational study investigating the Ostwald ripening mechanism of Au clusters on a MgO(001) support. Commonly, the efficacy of heterogeneous catalysts is determined by the composition, size and shape of the potential active sites under reaction conditions.¹⁻⁵ Often built by late transition metal nanoparticles (NPs), the active phase varies depending on the application of the catalysts, but they must generally possess a large exposed area of active sites and be highly resilient, i.e. resistant to changes induced by reaction conditions. Processes that lead to changes in the shape, size, or number of these sites instigate the deactivation of the catalyst, causing a decrease in catalyst productivity and/or selectivity.

As described in the introduction, one of the most important deactivation processes, is sintering. Sintering leads to the loss of active surface area by agglomeration of the metal nanoparticles, which is exacerbated by thermal effects. When this process does occur, often from heat treatment during catalyst synthesis methods or reaction conditions, the small active NPs aggregate to form larger, more stable and usually less active NPs.⁶⁻⁹ With an increase in size of the metal NP's comes a reduction in available active sites, as more atoms make up part of the bulk of a nanoparticle, rather than the surface. There is also a loss of specific sites, often noted as being particularly reactive, i.e. step, corner or edge atoms. The sintering process is difficult to reverse and the cost of replacing inactive catalysts can be very high, not only because of the cost of late transition metals generally involved, but also in the process of replacing them. It is possible that, if sintering rates and mechanisms are better understood, then this deactivating process can be more successfully minimised or reversed by redispersion (or digestion) of the metal on the catalyst surface.¹⁰

Two principal ripening mechanisms have been established to contribute to sintering processes: crystallite and atomic detachment.¹¹ During crystallite detachment,¹² a whole cluster will migrate, collide with another particle and coalesce to form a single, larger nanoparticle. This is also known as Smoluchowski ripening or coalescence. During atomic detachment, a single atom breaks off (digests) from the less stable structure (known as Ostwald digestion) and diffuses toward other NPs where it is enveloped onto the new, commonly larger and more stable structure (known as Ostwald ripening).¹³ These processes are driven by reduction of the surface-bulk ratio and therefore increases stability.¹⁴

Ostwald ripening

The migration of a single building block (here metal atoms) to and from metal clusters is often termed Ostwald ripening, an illustration of which is shown in Figure 4.1.

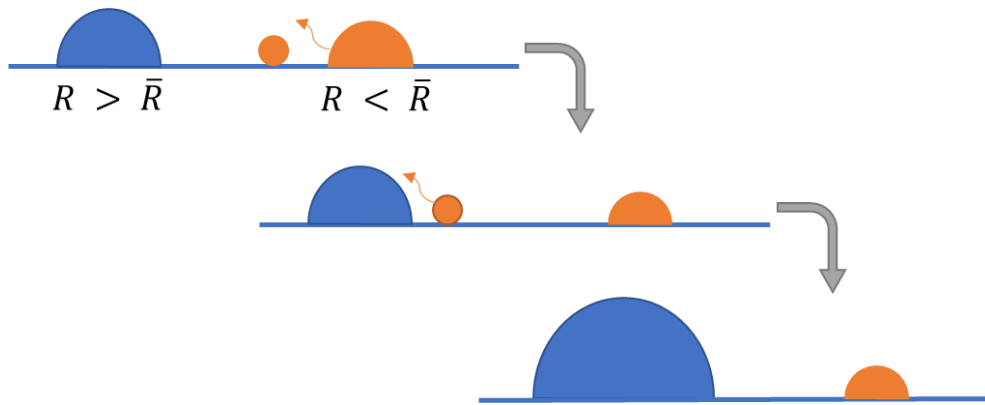


Figure 4.1 Ostwald ripening mechanism. \bar{R} is the diameter of a particle of average size.

The rate of change for cluster size by Ostwald ripening can be determined if the average size of the particle is obtained using Equation 4.1.⁹ A ratio < 0 indicates particles will shrink and > 0 will grow. \bar{R} being the radius of the average sized particle.

$$\frac{dR}{dt} = \frac{1}{R} \left[\frac{R}{\bar{R}} - 1 \right] \quad (4.1)$$

Smoluchowski ripening or Coalescence

Coarsening via the Smoluchowski, or coalescence mechanism, occurs by the diffusion of small clusters of atoms rather than single atoms, followed by the subsequent merging to other clusters, as described by Equation 4.2. Coalescence of supported NP's, involves the mobility of particles in a Brownian-like motion on the support surface, with subsequent merging with another cluster leading to nanoparticle growth.¹¹



Where k is the probability (or rate) of a merge. The mean size of the particle goes from being $\frac{(a)+(b)}{2}$ to $a + b$.

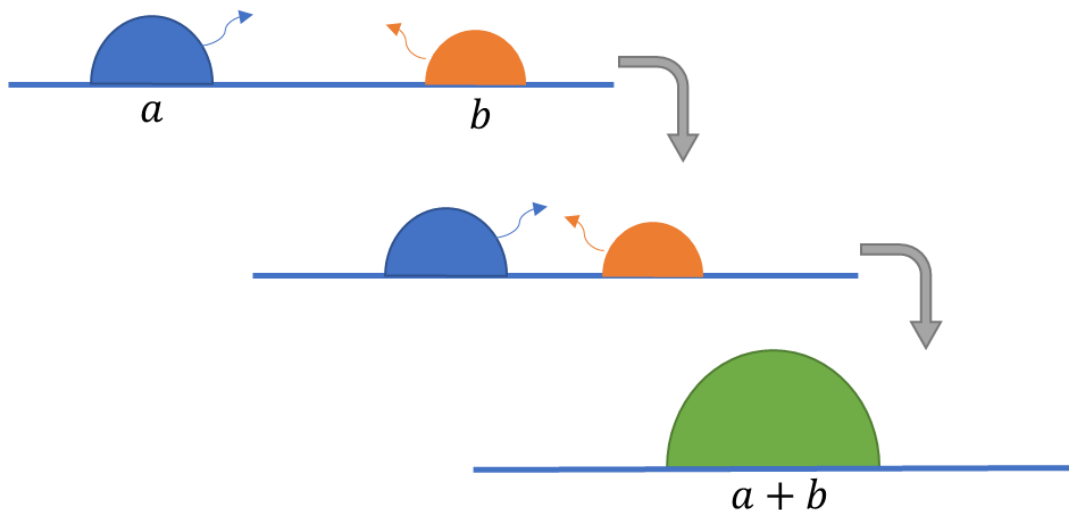


Figure 4.2: Schematic representation of the Coalescence ripening mechanism of supported clusters.

Ostwald or Smoluchowski ripening?

There is some argument regarding the dominant mechanism under particular conditions. Considerations such as, metal dispersion, particle size and strength of adsorption to the surface have been discussed.^{11,15}

It is argued that where dispersion of the metal species is high, the probable mechanism would be Ostwald ripening. The reason suggested for this is that whole particle diffusion would require more energy, so would be unlikely at longer distances. However, when dispersion is lower, and metal clusters have smaller distances to travel over, coalescence may occur more frequently. Additionally, when the dispersion is high, smaller clusters are more likely to contain less atoms, from which, it would be easier for a single atom to detach than from a larger cluster. Thus, the system may undergo Ostwald ripening. Over time or when metal dispersion is lower, the number of small clusters will decrease, and so the mechanism may switch to favour coalescence.¹¹

The strength of the interaction between the metal cluster and the support (E_{ads}) can also influence which type of growth mechanism occurs.¹⁶ For example, if the metal species has a strong interaction with the surface, then diffusion of the species would require more energy, limiting the system to single atom diffusion and coalescence would be disfavoured. The lower the adsorption energy the more likely diffusion of clusters becomes. With this in mind, it

must also be considered that the interactions of atoms within the metal cluster would make a difference to the growth mechanism operated. The stronger the bonds between metal atoms the greater the energy required for single atom detachment, thus, Ostwald ripening may be less prevalent, particularly at lower temperatures.

The idea that one mechanism is chosen over another may be too simplified, and the co-existence of both mechanisms working simultaneously should be considered. There have been research groups that have been dedicated to eluding the dominant mechanism for particular systems. To this end, a typical method is measuring particle density distribution.^{11,17} The success of this method comes from the fact that the particle density will be reduced immediately if ripening proceeds via coalescence, whilst if the predominant mechanism is Ostwald ripening, the particle density will be retained for longer, as the clusters will shrink in size before disappearing completely. However, for the very small cluster sizes described in this thesis (< 1 nm), it has been suggested that using this method may not yield reliable results. Even if ripening only occurred via Ostwald ripening such small particles would disappear very quickly, making it difficult to observe the process. Additionally, this method is only successful as long as the clusters are detectable, which becomes more difficult at smaller sizes. Therefore, other methods of determining the dominant mechanism must be sought for systems such as Au_n/MgO (n =1-10).

It is implied from the literature that high metal dispersion would mean a dominant Ostwald ripening mechanism. Thus, the modelling of the Ostwald ripening performed here is justified by the very high metal dispersion modelled. Moreover, modelling Smoluchowski ripening is much more demanding. The difficulty in modelling the coalescence mechanism comes from the fact that the method of migration of the small clusters is less predictable and adding more atoms to the diffusion increases its complexity. The diffusion may involve some form of leapfrogging of the particles, rocking, rolling or walking motions.¹⁸ All variants of these movements would need to be modelled and would exponentially increase the computational demands in comparison to modelling single atom diffusion.

Methodology

In order to study the Ostwald ripening process, the Au_n/MgO, Au_{n+1}/MgO and Au_{n+1}/MgO systems were modelled using the same computational methodology as was described in the determination of low energy clusters (Chapter 3). The PBE density functional of Perdew, Burke, and Ernzerhoff¹⁹ was used to calculate the exchange and correlation contributions. Dispersion interactions were calculated using the Grimme's empirical dispersion correction

DFT-D3.²⁰ Projector-augmented wave (PAW) pseudopotentials^{21,22} as implemented in VASP were used to describe the core electrons. A kinetic cut-off was set at 450 eV and a 3×3×1 Monkhorst-Pack k-point grid was used after benchmarking for the Brillouin zone integration.

The reaction coordinate in relation to ripening processes (Au_{n+1}/MgO to Au_{n+1}/MgO) for the single Au atom diffusion and attachment to an Au cluster have been studied, see Figure 4.4. The Au_n/MgO systems were taken directly from the calculations performed in Chapter 3 and further modelling was performed to produce Au_{n+1}/MgO systems, which consist of a cluster of size n and a single atom within the same unit cell, both supported on the surface. An example of these systems, where the initial ($Au_2 + 1$), TS and final states (Au_3) from single atom attachment (Ostwald ripening) is shown in Figure 4.3.

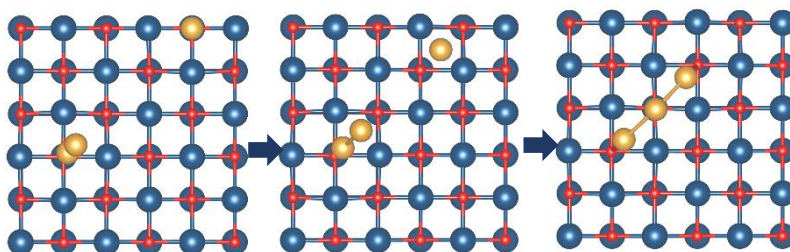


Figure 4.3: Single atom attachment to an Au_2 cluster to form Au_3 on MgO. Blue = Mg, Red = O and Gold = Au. Initial (left), Transition state (centre) and final (right) structures.

Once the initial (Au_{n+1}) and final (Au_{n+1}) systems were modelled, then a static path technique was used to identify the transition states (TS) associated with atomic attachment of Au atoms to Au clusters on magnesia. In this technique, several structures (in this case 10) were taken from between the initial (Au_{n+1}/MgO) and final systems (Au_{n+1}/MgO) along the reaction coordinate and optimised, using a quasi-newton method. The structure determined to be closest to the highest energy point on the PES had its bond frequencies analysed. TS's positioned on the PES that correspond to minima in all directions except one and were confirmed from observing a single normal mode associated with an imaginary frequency along the reaction path. If a TS is not found, the structure undergoes further optimisation to move the structure in the correct direction along the coordinate path, until a single imaginary frequency is found.

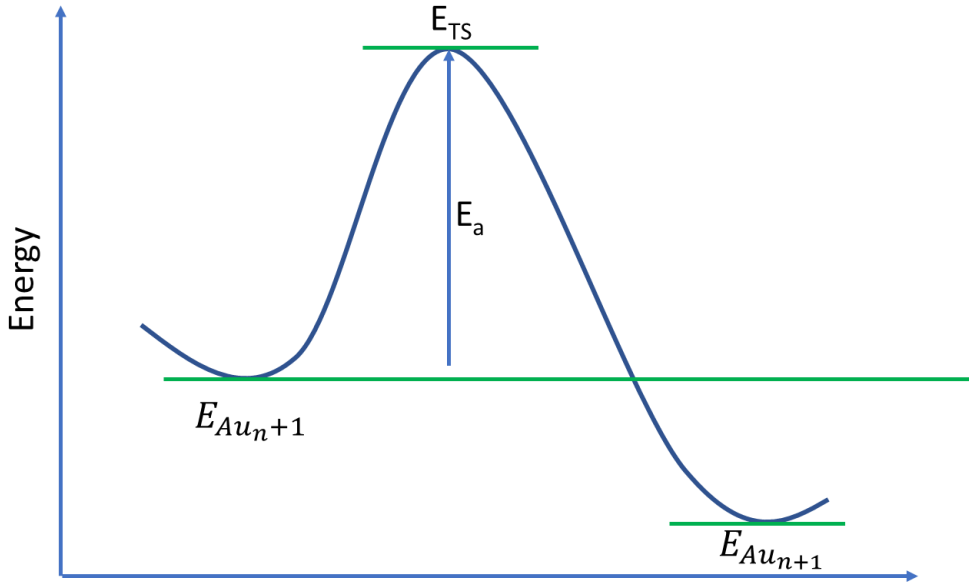


Figure 4.4: Represents the reaction profile for a single atom attachment along the reaction coordinate to a supported Au cluster (Au_{n+1}). E_{TS} is the energy of the transition state structure, E_a is the migration barrier and E_r is the stability of the $E_{Au_{n+1}}$ system compared to the initial $Au_n + 1$ system.

The energy barriers (E_a) to ripening are calculated as follows, by Equation 4.3:

$$E_a = E_{TS} - E_{Au_{n+1}} \quad (4.3)$$

Where the $E_{Au_{n+1}}$ is the energy of the system before attachment of the single atom to the cluster with it on the same surface as the cluster, and E_{TS} is the energy at the transition state of the attachment. Reaction energies (E_r) are also calculated according to Equation 4.4.

$$E_r = E_{Au_{n+1}} - E_{Au_{n+1}} \quad (4.4)$$

Microkinetic methodology

Microkinetic modelling is employed from the DFT results within a TST framework and the effect of temperature and Au coverage (θ) is included. Microkinetic modelling is a method whereby the process of interest is broken down into its elementary reaction steps. This allows for a discussion of reaction dynamics and rates based on the partition function of each individual system. For study of Ostwald ripening processes, the elementary steps are the diffusion, attachment and detachment of single atoms.

Many characteristics of a system can be studied using the partition function. An example of these is the probability (P) of finding the system in a state with energy ϵ_i at a given temperature (T), where g_i is the state degeneracy, by using the following equation:

$$P_i = \frac{e^{-\frac{\epsilon_i}{k_B T}}}{\sum_{i=0}^{\infty} g_i e^{-\frac{\epsilon_i}{k_B T}}} \quad (4.5)$$

Where the partition function is the denominator. Another example is the average energy of a system ($\bar{\epsilon}$) and as described by the equation below.

$$\bar{\epsilon} = k_B T^2 \frac{\partial \ln Q}{\partial T} \quad (4.6)$$

The distribution of systems at given conditions is described by the Maxwell-Boltzmann distribution, where the partition function gives a summation of the states of a system. This description permits combination with transition state theory allowing a derivation of numerically obtained observables at the macroscopic level.

The equation for determining the partition function is as follows:

$$Q \equiv \sum_{i=0}^{\infty} g_i e^{-\frac{\epsilon_i}{k_B T}} \quad (4.5)$$

Where g_i is the state degeneracy to account for all available states even if they are the same energy, ϵ_i is the energy of the state i , k_B the Boltzmann constant and T the temperature. It is through the sum of all energy levels that the partition function is used to determine all the properties of a system, including the average energy and free energy.

Q , the total partition function is the product of all the individual partition functions for all indistinguishable particles (q^N):

$$Q \equiv q^N$$

$$q = q_{trans} q_{rot} q_{vib} q_{elec} \quad (4.6)$$

The translational partition function (q_{trans}) relates to the species ability to move in certain dimensions, i.e. volume (3D) or area (2D). The rotational partition function (q_{rot}) relates to the number of rotational degrees of freedom that a species has. In the microkinetic simulation of Ostwald ripening on the surface, the translational and rotational partition functions equal to one, as the movement and rotation of the gold atoms and clusters are frustrated by their adsorption to the surface. The partition function of the Au_n/MgO systems are then defined by the vibrational (q_{vib} : Equation 4.7) and electronic (q_{elec} : Equation 4.8) partition functions where the natural vibration modes are obtained through frequency calculations and the electronic contribution considers only the ground state electrons degeneration.²³ The electronic partition function for the Au system is dependent upon the number of Au atoms in the systems as this dictates the number of electronic states (Au electronic configuration is $[Xe] 4f^{14} 5d^{10} 6s^1$).

$$q_{vib} = \prod_i \frac{1}{1 - e^{-\frac{h\nu_i}{k_B T}}} \quad (4.7)$$

$$q_{elec} = g_{e0} e^{-\frac{\epsilon_0}{k_B T}} \quad (4.8)$$

Where g_{e0} represents the degeneracy of the electronic ground state ϵ_0 . The electronic excited states are determined to be too high in energy for this process, and their contributions to q_{elec} are negligible at the temperatures considered in this simulation (up to 510 K).

Many thermodynamical variables can be defined from the partition function. For instance, the total partition function (Q) can also be used to describe entropy (S), at temperature T :

$$S = \frac{\partial}{\partial T} [k_B T \ln(Q)] \quad (4.9)$$

Enthalpy (H) can also be calculated using the partition function, as a combination of the energy calculated by DFT calculations (E_{DFT}), the zero-point energy (ZPE), and an integration of the specific heat capacity with respect to temperature (C_p), which is another thermodynamic variable found from Q .

$$H = E_{DFT} + ZPE + \int_{T=0}^T C_p \partial t \quad (4.10)$$

$$ZPE = \frac{1}{2} \sum_i h\nu_i$$

$$C_p = T \left. \frac{\partial S}{\partial T} \right|_{(N,P)}$$

When both the entropic and enthalpic contributions have been calculated, Gibbs free energy can be obtained through the following relationship:

$$G = H - TS \quad (4.11)$$

Subsequently, once the Gibbs free energies have been calculated for all the systems this enables the calculation of reaction rates. The constant rate (k) of each elementary surface step is commonly computed using the transition state theory approximation of Eyring and Polanyi²⁴. To describe the rate of a process, k :

$$k = A e^{-\Delta G/k_B T} \quad (4.12)$$

$$A = \frac{k_B T}{h} \frac{Q_{TS}}{Q_R}$$

Where the h is the Plank constant, k_B is the Boltzmann constant and T the temperature. The calculated partition function for the transition state (Q_{TS}) and the reactants (Q_R) is used to calculate the pre-exponential factor (A). The reaction activation energy (ΔG) is calculated from the Gibbs free energies of the TS and the reactants. Once the rate constant has been determined for all processes, e.g. the single atom diffusion and attachment to an increasingly larger gold cluster, then the rate of conversion between states is calculated at specific temperatures and Au loadings.

Transition state theory (TST) has been used for many years to help identify the energy required to overtake transition states along a reaction path. It does so by treating reacting systems as rigid spheres without internal degrees of freedom as in collision theory. However, limitations to TST include a disregard for short-lived intermediates and failure at high temperatures, due to the assumption that the reaction system passes over the lowest energy saddle point on the potential energy surface.²⁵ One of the additional weaknesses associated with TST is its representation of quantum tunnelling effects. In order to improve our method, tunnelling of the activation barriers is considered by applying the Wigner correction to the energy²⁶ using Equation 4.13. At typical higher reaction temperatures tunnelling effects do not play an important role and this correction is negligible and disappears while at low temperatures it goes to the zero-point energy correction.²⁷

$$E_{tunnel} = -k_B T \ln \left[\frac{\frac{\prod_i \sinh(v_i^{init})}{v_i^{init}}}{\prod_i \sinh(v_i^{TS})/v_i^{TS}} \right] \quad (4.13)$$

Metal dispersion

The metal dispersion for the Au_n/MgO system in this thesis is calculated for the purposes of understanding how the modelled system compares to that of an experimentally created catalyst. By calculating the area of the unit cell, the number of atoms (N_m) per unit cell area (a^2 , where a is 1.678×10^{-9} m for this system) is calculated from the following equation:

$$\text{Atoms per unit area} = \frac{N_m}{a^2} \quad (4.14)$$

One Au atom is present per unit cell and the MgO unit cell area is $2.816 \times 10^{-18} \text{ m}^2$. This leads to the calculation of $3.552 \times 10^{17} \text{ Au atoms m}^{-2}$, which is equivalent to $1.16 \times 10^4 \text{ g}_{Au} \text{ m}^{-2}$.

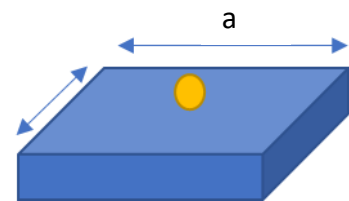


Figure 4.3: Schematic of Au_n/MgO system, where a is the lattice constant (16.780 \AA).

Finally, the metal dispersion is calculated as $8608.44 \text{ m}^2\text{g}_{\text{Au}}^{-1}$. Experimentally, the metal dispersion of prepared catalysts varies depending on the catalyst and its preparation method. For example, a 12 wt% Ni/Al₂O₃ catalyst used for hydrogenation reactions has a metal dispersion of around $150 \text{ m}^2\text{g}^{-1}$,²⁸ in 1-20wt% Cu in CuO/Al₂O₃-ZrO₂ catalysts for the synthesis of biofuel 2-methylfuran, the metal dispersion ranges between $180\text{-}536 \text{ m}^2\text{g}^{-1}$,²⁹ while a 1 wt% Au-SiO₂ catalyst has been reported with metal surface area of $18 \text{ m}^2\text{g}^{-1}$,³⁰ which is increased to $101 \text{ m}^2\text{g}^{-1}$ when alloyed with Pd.

From comparison to these values, it can be seen that the Au has a much higher dispersion metal in the microkinetic simulation (almost 20x) than is typical for catalyst produced experimentally. As described previously, it has been argued that with low metal dispersions, growth proceeding by the Ostwald ripening mechanism is much more likely than growth from coalescence. This supports the choice to model the Ostwald ripening mechanism for this system.

Results and Discussion

The structural and energetic properties of the lowest energy clusters (Au_n, n = 1-10) were described in Chapter 3. Calculations of the adsorption, binding and cohesion energies of the system were undertaken alongside a Bader charge analysis and observation of the spin magnetisation of the clusters. From examination and discussion of these parameters, it was concluded that an increase in the cluster size results in the increase of the cohesion energy (E_{coh}) and a decrease adsorption energy (E_{ads}) per cluster atom toward Au bulk values. The overall interaction is expressed by the binding energy (E_{b}), which shows an overall increase in stability of the Au_n/MgO system with increasing cluster size. This finding is in line with the accepted idea that particle size will increase to minimise the surface to bulk ratio³¹ and was also supported by the decrease in charge transfer per Au atom to the support from the charge analysis.

Migration mechanism

The first process analysed was diffusion, for this, single atom migration across the MgO(001) surface was evaluated. Initially, calculations were made to determine the most stable adsorption site for a single Au atom on MgO(001). As previously described, three stable positions were found, a top an O atom, a top an Mg atom and in the hollow. The most stable of these positions with an adsorption energy of 1.37 eV is on top an O atom. This compares to a value of 0.89 eV for adsorption a top a Mg atom and 1.09 eV in the hollow site.

From this, the most favourable migration path was determined. Due to the symmetry of the support, there are two possible diffusion pathways from the most stable O top position to an adjacent equivalent one: i) The path in a straight line crossing a hollow site and ii) the pathway across a magnesium atom. The energy barrier for the process across the hollow was measured to be 0.29 eV, while across the Mg is 0.22 eV higher. Therefore, the path across the hollow has a lower migration barrier and is more favourable. See Figure 4.4 for the images of these paths.

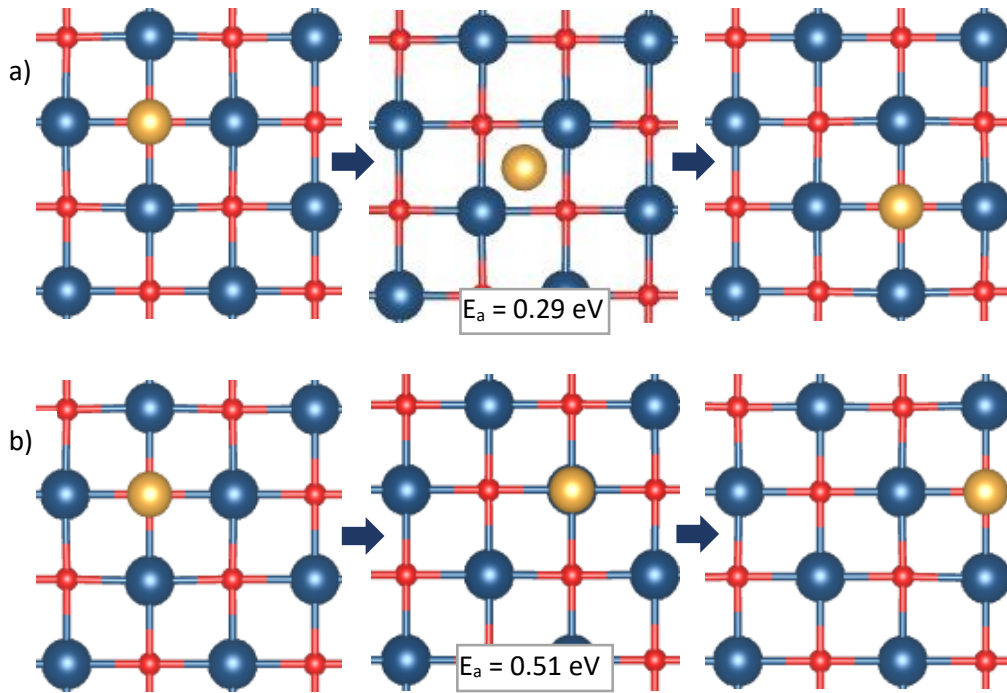


Figure 4.4: Diagrams representing the initial (left), transition (centre) and final (right) states of the two migration pathways: a) the path across the hollow and b) the path across the Mg. Mg = blue, O = red, Au = yellow.

The movement of the Au atom across the MgO surface is related to its surface diffusion coefficient (D) at temperature (T). The surface diffusion is given by Equation 4.15.

$$D = \frac{\Gamma a^2}{z} \quad (4.15)$$

Here $a = nd^2$, where n is equal to the number of jumps, therefore $n=1$ for a single jump and d is the distance travelled per jump, which here is equal to the distance between O adsorption sites (2.97\AA). z is the dimensionality of the motion, according to the surface symmetry = 4, i.e. 2 perpendicular directions, both forward and backwards, for 2D diffusion. Γ is the hopping rate, defined in Equation 4.16:

$$\Gamma = \nu \exp\left(-\frac{E_a}{K_B T}\right) \quad (4.16)$$

where ν describes the frequency taken from the vibrational frequency of the atom. The essential feature of this equation is the dependence of Γ on the diffusion energy barrier. It is important to note that these equations hold true for when $E_a \gg k_bT$, when E_a approaches k_bT the barrier becomes too small to be considered important, this is known as mobile diffusion.

For the Au₁/MgO system, at 300K, the surface diffusion (D) is calculated as $3.20 \times 10^{-9} \text{ cm}^2 \text{ s}^{-1}$. This value is comparable to the calculated diffusion at 300 K of Cu on a Cu(100) surface of $2.39 \times 10^{-12} \text{ cm}^2 \text{ s}^{-1}$ performed by Yildirim *et al.*³² which had to overcome a higher diffusion barrier of 0.5 eV.

Ostwald Ripening mechanism

Once the barrier to single atom diffusion across the MgO(001) support was obtained, calculations of the energy barriers (E_a) associated with attaching a single atom to clusters of increasing size (the ripening process) were undertaken, these barriers are associated with the more favourable path determined by the analysis of the migration mechanism (the path across the hollow) as seen in Figure 4.5.

The migrating atom starts on top of an O site around 0.6 nm away from the cluster position, approximately two oxygen distances away, this ensures that the migrating atom is on a stable position far enough away from the cluster to avoid interaction. Larger distances were tried and no energy differences were measured, whilst a starting distance nearer the cluster does not allow the atom to sit upon a stable position without bonds being formed with the cluster during optimisation. The atom then crosses the hollow toward the cluster to another O site and merges with the cluster, as seen in Figure 4.5. Energetic and structural information relating to the single atom attachment at each cluster size can be found in Table 4.1. From

the system energy calculations, the reaction energies (E_r) associated with attachment of the single atom and the barriers (E_a) toward the ripening process are derived.

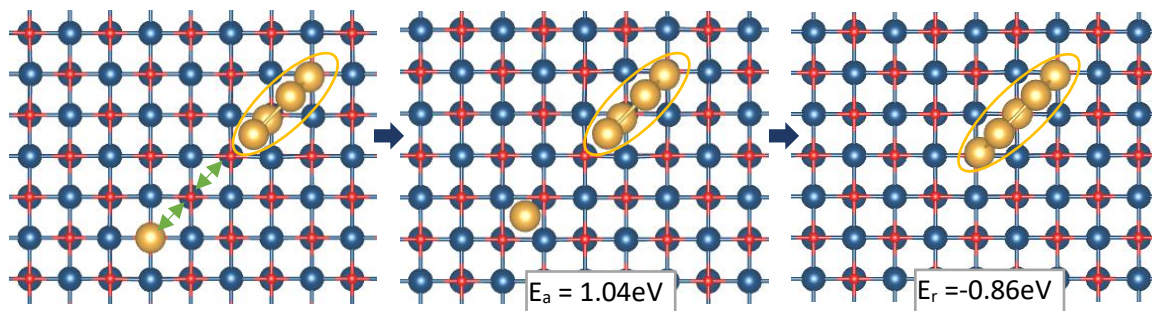


Figure 4.5: Representation of a single atom attachment path to an Au_4 cluster leading to Au_5 . Blue = Mg, red = O and gold = Au. The oval encompasses the atoms contained in the Au_4 cluster. The green arrow represents the path of the migrating atom, the atom moves from a distance of around 0.6 nm.

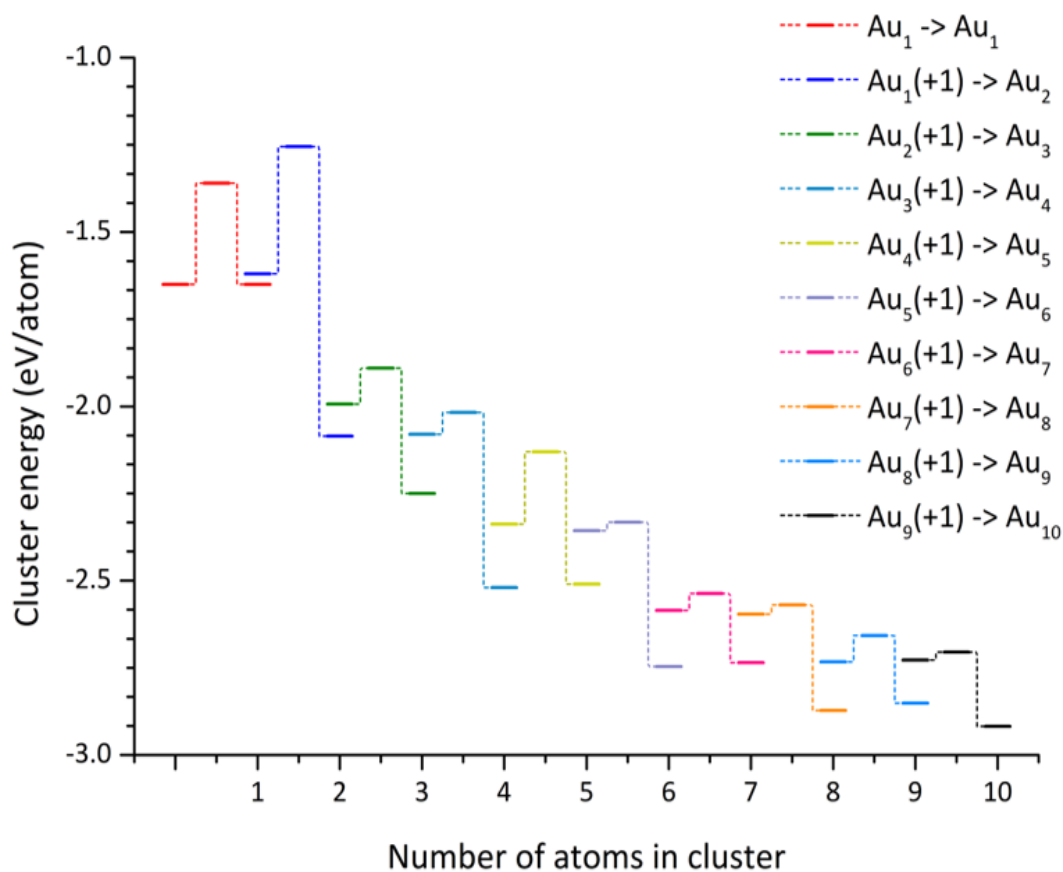


Figure 4.6: Relative energies of gold clusters (Au_n and Au_{n+1}) on MgO. The energy difference between systems of the same cluster size is due to the addition of a single atom in the unit cell as well as rearrangement of the cluster configuration for some systems.

Table 4.1: Shows the ripening barrier (E_a), attachment reaction energy (E_r), average surface to cluster distance ($\overline{dAu_{n_i} - S}$), where Au_{n_i} is cluster atoms in contact with the support (at the interface), average cluster gold-gold distance ($\overline{dAu - Au}$), the magnetisation of the Au_{n+1} system (m_s).

Initial cluster size (Au_n)	Final cluster size (Au_{n+1})	E_a (eV)	E_r (eV)	$\overline{dAu_{n_i} - S}$ (Å)	$\overline{dAu - Au}$ (Å)	$Au_{n+1} m_s$ (μ_B)
1	2	0.73	-0.93	2.198	2.516	0.0
2	3	0.31	-0.77	2.292	2.596	1.0
3	4	0.25	-1.76	2.207	2.654	0.0
4	5	1.04	-0.86	2.239	2.712	0.9
5	6	0.14	-2.34	2.705	2.716	0.0
6	7	0.34	-1.05	2.695	2.740	0.5
7	8	0.21	-2.21	2.676	2.710	0.0
8	9	0.68	-1.06	2.710	2.793	0.2
9	10	0.23	-1.90	2.731	2.746	0.0

The attachment of the single gold atom in the formation of all larger clusters (Au_{n+1}) leads to more stable systems (negative E_r) and supports ripening as a thermodynamically favourable process. The activation barriers associated with single atom attachment in all systems are relatively small (< 1.05 eV) and implies a fairly high mobility of gold atoms on the MgO support,³³ which is in part due to the lack of defects in the MgO or other surfactants that may help to stabilise metal structures on the surface.³⁴ Although the reaction energies are all negative, the formation of an even number cluster is associated with a larger negative reaction energy (E_r) than the formation of an odd numbered cluster and illustrates that even clusters are more stable than odd clusters, due to electron pairing. This is exhibited in Figure 4.6, plotting the cluster energy according to Equation 4.18.

$$Cluster\ energy = \frac{E_{Au_n/MgO} - E_S}{n} \quad (4.18)$$

Where $E_{Au_n/MgO}$ is the optimised system energy, E_S is the energy of the pristine optimised slab and n is the number of atoms in the Au cluster.

Odd number clusters have an odd number of gold atoms with unpaired electrons; therefore, the cluster has overall spin, away from zero, rendering the creation of an odd numbered cluster from attachment of a migrating atom less favourable (formation of an odd numbered cluster has a higher E_a and a less negative E_r). For even cluster sizes, there is an even number of atoms in the cluster, the attachment of a single atom to an odd numbered cluster results in pairing of the unpaired electrons of gold, leading to no spin of the cluster overall. Consequently, the ripening barriers E_a are smaller and reaction energies E_r are more negative, resulting from the formation of a more stable system. This pairing interaction is evidenced by the cluster magnetisation of the system as shown in Table 4.1 and the images shown in Figure 4.7. The analysis of the energies of the different systems supports the conclusion that the formation of the even number clusters (whilst the clusters are non-metallic in nature, i.e. distinguishable energy states, rather than bands) is more beneficial to stabilise the unpaired electrons in the system.

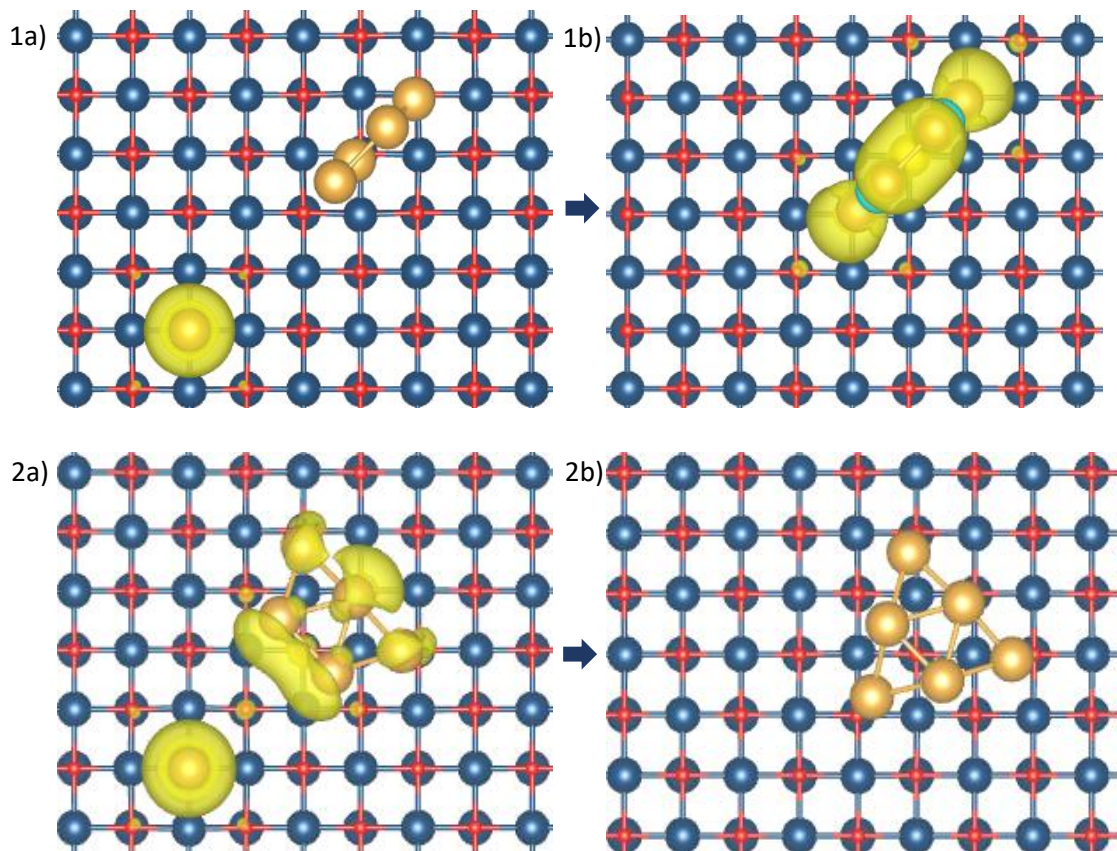


Figure. 4.7: Representation of the odd-even spin magnetisation trend. 1a) $Au_4 + 1$ and 1b) Au_5 cluster systems showing a) the spin centred on the single atom whilst the even size cluster has no magnetisation and b) the spin delocalised over the Au_5 cluster. 2a) The $Au_5 + 1$ and 2b) Au_6 cluster systems showing a) the magnetisation on the Au_5 cluster as well as the single atom, an b) the cluster magnetisation going to 0 on formation of the Au_6 even size cluster. Isosurface level = $0.001 e/\text{\AA}^3$. Blue = Mg, red = O and gold = Au.

Additional to the odd-even overall trend in the energies of cluster formation, the values of E_a for the formation of an Au_6 and Au_8 clusters are unexpectedly low and the E_r values are more negative than anticipated. These values imply increased stability of clusters at these sizes, but may also point to lower stability of Au_5 and Au_7 leading to an increased favourability of ripening processes to form Au_6 and Au_8 .

Microkinetic modelling

The information regarding barriers and reaction energies was integrated in microkinetic models to simulate two processes: cluster ripening and cluster digestion. The application of the microkinetic model described shows the distribution of the species in the system at specific temperature (T) and time (t) with particular initial conditions. θ_i is defined as the initial occupation of cells containing only Au_x ($x = 1$ for ripening and 10 for digestion) at the beginning of the experiment ($t = 0$ s). Hence, in the ripening experiment, θ_1 is indicating that all unit cells contain Au_1 .

In the ripening microkinetic simulations, three initial occupations (θ_i) were used ($\theta_{0.1}$, $\theta_{0.5}$ and $\theta_{0.9}$), giving 10% 50% and 90% of the maximum number of cells with Au_n . This corresponds to a metal dispersion of $86084 \text{ m}^2 \text{ g}_{Au}^{-1}$ at the minimum and $9564 \text{ m}^2 \text{ g}_{Au}^{-1}$ at the maximum.

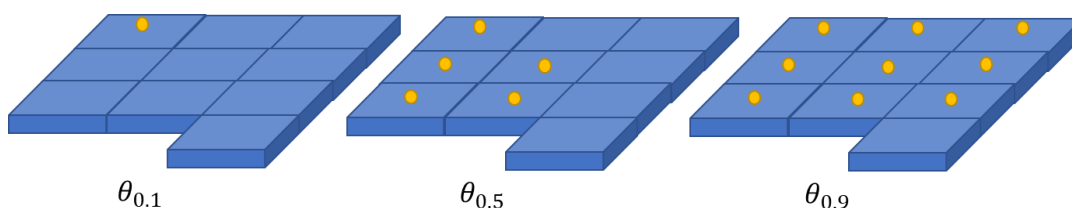


Figure 4.8: Diagrammatic representation of 10 times the area of the slab ($2.816 \times 10^{-18} \text{ m}^2$) with the initial occupancy of cells θ_i . The yellow circles representing clusters size Au_1 .

The dispersion of gold modelled here is significantly higher than typically achieved for heterogeneous catalysts. It is expected that for a typical catalyst, with lower metal dispersions, the rate of change of the system would be accelerated. How the fraction of occupied cells with particular cluster sizes (χAu_n) changes over the simulation time frames at specific temperatures has been plotted (Figures 4.9 to 4.17). These are fractions of the number of occupied cells, stated by θ_i . For example, if the χAu_1 is 0.9, then 90% of the initial occupied cells contain a single Au atom (Au_1). If the starting occupation was $\theta_{0.1}$ then, 9 out of 100 cells (9%) would contain a single atom and if the starting occupation was $\theta_{0.9}$, then 81 of 100 cells would be occupied (81%).

Ripening

The time limits for the microkinetic simulation were set at 60 s and 1 s. For the 60 s simulations a 1 s timestep was used. For the simulations set at a maximum of 1 s, the time step was 0.02 s. The temperature increases from 10 K to 510 K, ramping by 50 K.

It can be seen from Figure 4.9, that the gold remains as Au₁ on the MgO surface below 160 K independently of initial content. This indicates that the diffusion barrier of 0.29 eV is enough to prevent movement of the gold atoms across MgO surfaces. At 250 K, it takes a second for the atoms to agglomerate, e.g. starting fraction of Au₁ (with $\theta_{0.9}$) on the surface decreases to approximately 0.85, i.e. 85% of the original starting content. Single gold atoms begin to diffuse into other unit cells, creating a large fraction of cells with two individual atoms in a 7 x 7 MgO supercell (Au₁₊₁) as shown in Figure 4.11. All the Au₁ ($\theta_{0.1}$, $\theta_{0.5}$ and $\theta_{0.9}$) ripening systems then sees a quick transition to the biggest cluster considered (Au₁₀) in the simulation.

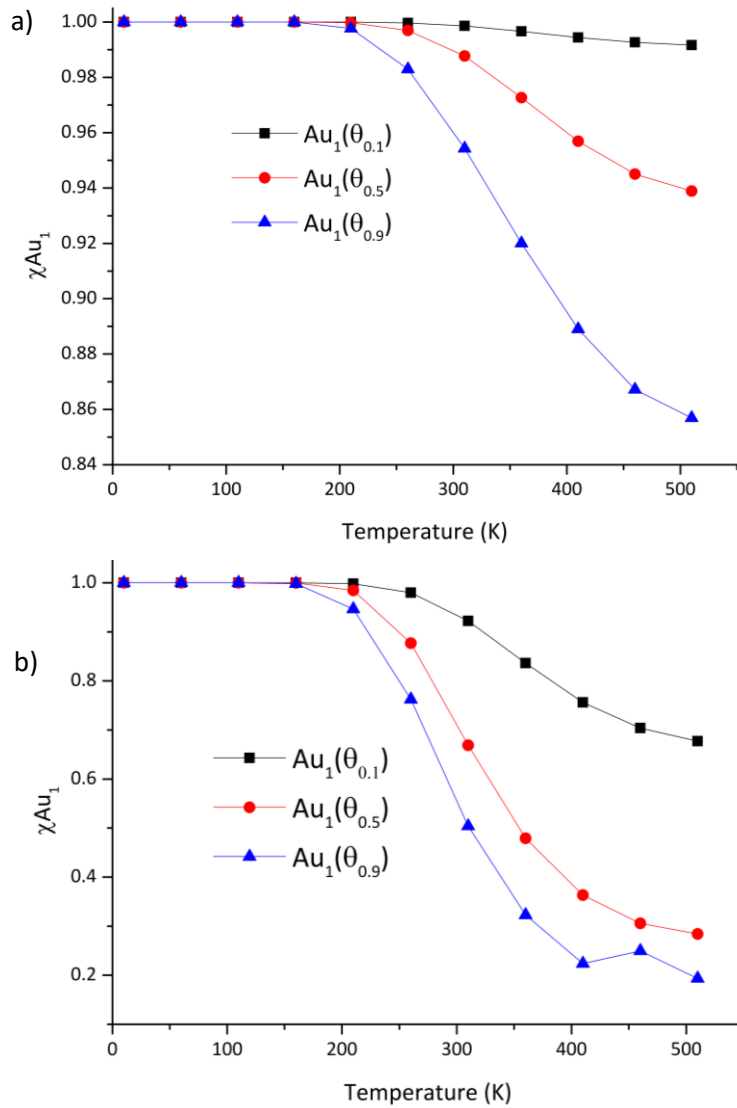


Figure 4.9: The χ_{Au_1} , after a) 1 second and b) 60 seconds at the temperatures on the x-axis from $\theta_{0.1}$, $\theta_{0.5}$ and $\theta_{0.9}$ of Au_1 .

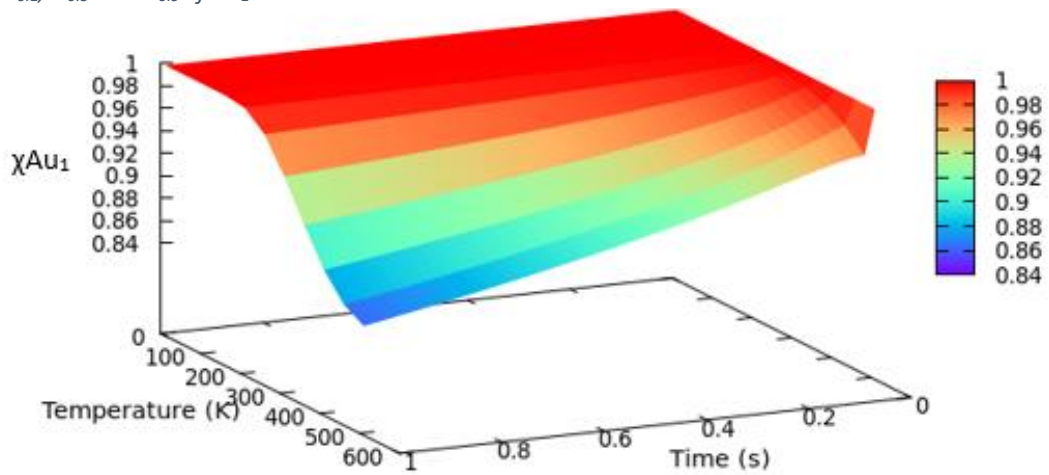


Figure 4.10: Graph to show the change in χ_{Au_1} over a 1 second time frame at temperatures 10 K – 510 K.

The initial drop in χ_{Au_1} in the first 0.02 s at the higher temperatures (410 K – 510 K), as seen in Figure 4.10, can be explained by the conversion into Au_{1+1} systems, shown in Figure 4.11.

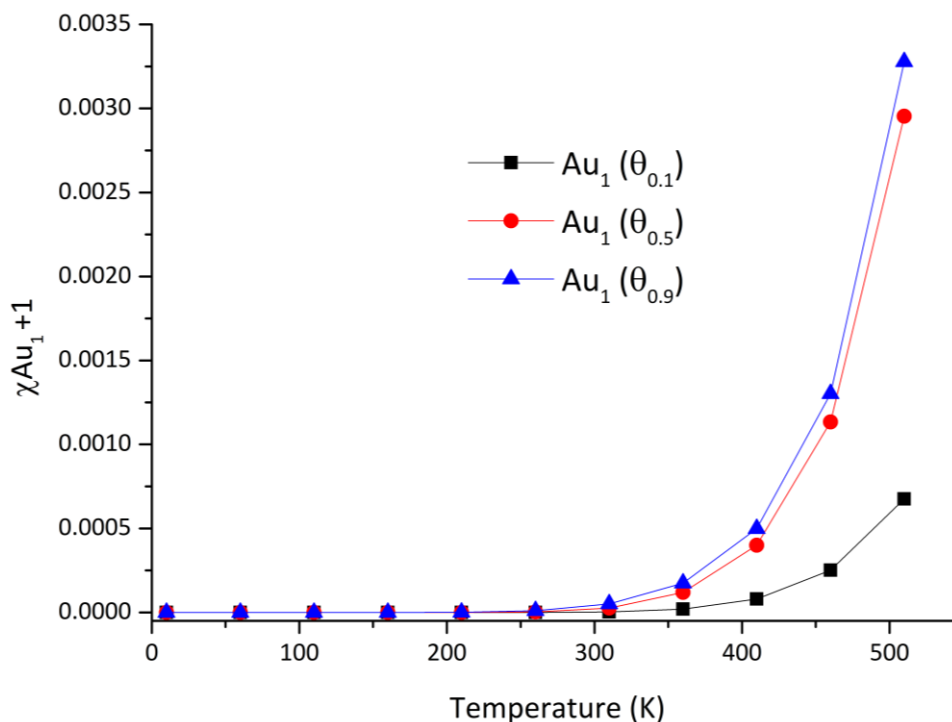


Figure 4.11: Graph shows the coverages of $\chi_{Au_{1+1}}$ after 0.02s at the temperatures on the x-axis with the Au_1 starting content of $\theta_{0.1}$, $\theta_{0.5}$ and $\theta_{0.9}$.

The energy barrier of conversion into a system with two single atoms of Au (Au_{1+1}) from a singly occupied system (Au_1) depends only on the diffusion of a single atom into the super cell. A steadier decline in the χ_{Au_1} fraction from 0.02 s onwards is associated with the attachment of the single atoms to each other and subsequent single atom attachment to clusters. The barriers for these processes (shown in Table 4.1) are very small and, as expected, the transition from single atoms to 10 atom clusters is very fast.

As a result of these very small barriers and the increasingly negative E_r 's, the other Au clusters ($Au_2 - Au_9$) are observed only in very small quantities, at any time and temperature, Figure 4.12. The lifetime of $Au_2 - Au_9$ clusters on the surface is cut short as more atoms attach to form larger sizes very quickly. Interestingly, and in agreement with previous observations,^{35,36} the fractions of clusters on the MgO surface of the even numbered clusters (Au_4 and Au_8 in particular) are higher than for odd numbered clusters, showing that even-numbered clusters are more stable than odd ones. The Au_2 can be seen to be rising particularly fast, this is due to the ease of creating an Au_{1+1} system, rendering formation of Au_2 more likely than other cluster sizes.

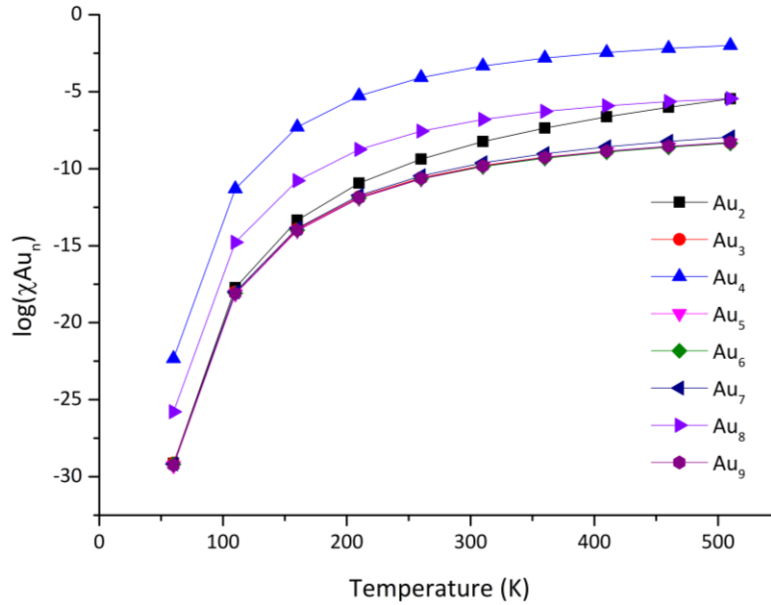


Figure 4.12: Comparative coverages of χAu_n clusters on the surface with $\theta_{0.5}$ after 1 second for the ripening experiment.

The lower fractions of the total occupied cells attributed to an Au_{n+1} system also points to a lack of stability in comparison to the merged clusters. This implies that a single gold atom within the same unit cell of a cluster will proceed to attach itself to that cluster as the energy barrier offers very little resistance to the growth process on the pristine MgO(001) surface. A plot of χAu_n , with both Au_n and Au_{n+1} , can be seen in Figure 4.13 for a comparison. As Au_n clusters grow, their retention time on the surface is relative to their stability. As Au_4 is particularly stable, it is harder to overcome the energy barrier forming larger clusters. For this reason, χAu_4 is larger than χAu_6 , while χAu_8 is again higher as the equilibrium is shifted toward it.

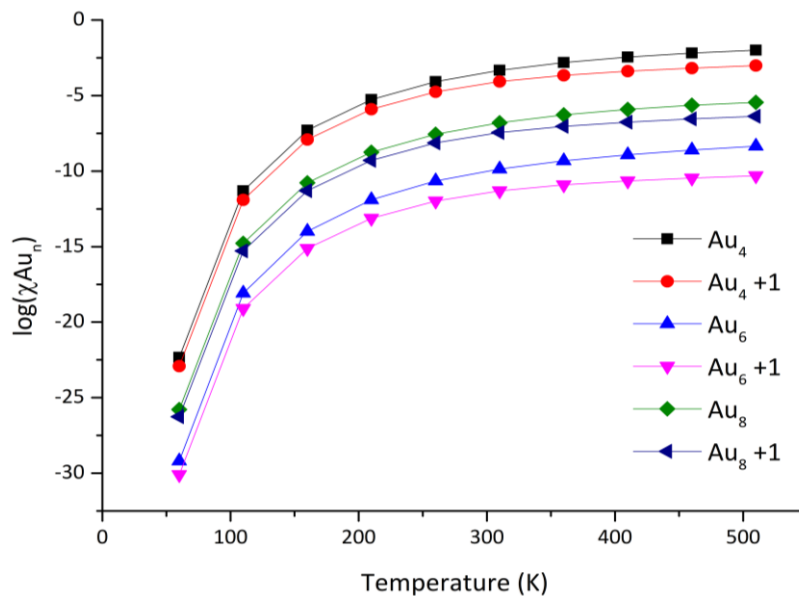


Figure 4.13: Graph showing the greater stability of the χAu_n clusters to the χAu_{n+1} clusters by displaying their comparative fractions from a $\theta_{0.5}$ starting content

Out of all the cluster sizes, the conversion is greatest to the Au₁₀ cluster, regardless of starting cell occupations of Au₁ ($\theta_{0.1}$, $\theta_{0.5}$ and $\theta_{0.9}$). This is because Au₁₀ is the most stable (and largest) cluster size in the simulation. However, in terms of the relationship between the nature of the species on the surface and the initial Au₁ coverage, the general trend is the greater the starting coverage, the quicker the ripening (higher gradient in the plots), both from single gold atoms and to all other species. This is illustrated by Figure 4.14, at a starting Au₁ gold occupation of $\theta_{0.1}$, the conversion to Au₁₀ after 1 s at 410 K is 0.268%, with a coverage of $\theta_{0.5}$ it is 3.87% and with $\theta_{0.9}$ it is 10.6% of the initial Au₁ amount.

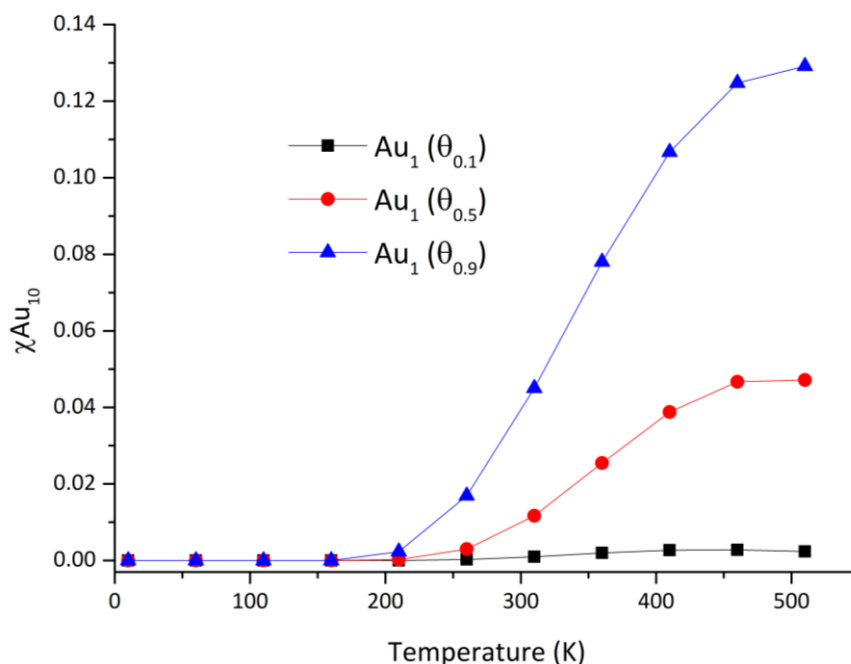


Figure 4.14: Graph to show the resulting Au₁₀ coverage after 1 second from Au₁ ($\theta_{0.1}$, $\theta_{0.5}$ and $\theta_{0.9}$) and at various temperatures.

Digestion

The digestion of supported metal Au clusters was also studied, where the surface was decorated with the largest, most stable structures and the fractions of the cluster sizes at different temperatures was measured, over the same time frame as the ripening experiments. As described in the introduction, redispersion techniques are used to reverse the effects of ripening. It is beneficial to look at the digestion process alongside ripening to help understand the kinetics of how clusters “re-disperse” to reduce the need to replace inactive catalysts.

To simulate the digestion process, i.e. forming isolated atoms or smaller clusters from big clusters, the microkinetic experiment started from an Au₁₀ cluster on the same MgO surface, with the same temperatures and time frames as set for the ripening experiment. From an

initial $\theta_{0.1}$ starting occupation of Au_{10} , almost all Au is present in an Au_{10} cluster. However there is some reduction at 160 K after 1 second, as presented in Figure 4.15. The $\chi_{\text{Au}_{10}}$ at 510 K, after 1 second, did not change, implying that almost all the occupied cells continue to contain an Au_{10} cluster. Very low conversion of Au_{10} clusters to any other cluster size implies the relative high stability of Au_{10} over all the other sizes permitted in the experiment.

The reduction of Au_{10} at 160 K is due to the presence of Au_8 and Au_9 clusters formed from single atom detachments, illustrated in Figure 4.16, which are energetically available at this temperature. The increase in the Au_{10} coverage after 160 K can be explained by the increased energy in the system providing greater movement and returning the atoms to the most stable cluster size available in the experiment (Au_{10}).

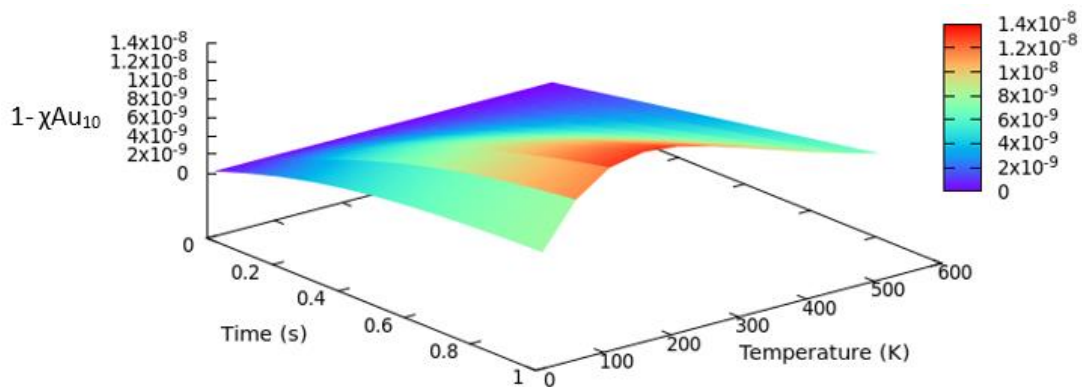


Figure 4.15: $1 - \chi_{\text{Au}_{10}}$ over a 1 second time frame with temperatures between 10 K and 510 K from $\theta_{0.1}$ of Au_{10} .

The conclusion that Au_{10} digests at 160 K to Au_9 and Au_8 is supported by the presence of peaks at temperatures between 100 K and 200 K for Au_8 and Au_9 , when the Au_{10} coverage is at its lowest, as seen in Figure 4.16. The χ_{Au_9} has the larger fraction ($6.69 \times 10^{-7} \%$ at 160 K, compared to $7.49 \times 10^{-11} \%$ for χ_{Au_8}). In addition to the increased fractions of Au_9 and Au_8 , an increase in the presence of Au_1 is also seen at these temperatures. Whilst there are peaks for Au_n clusters at 100K to 200 K, there are no Au_{n+1} species present, as they are not stable enough to remain on the surface, and the single atom attaches to the clusters.

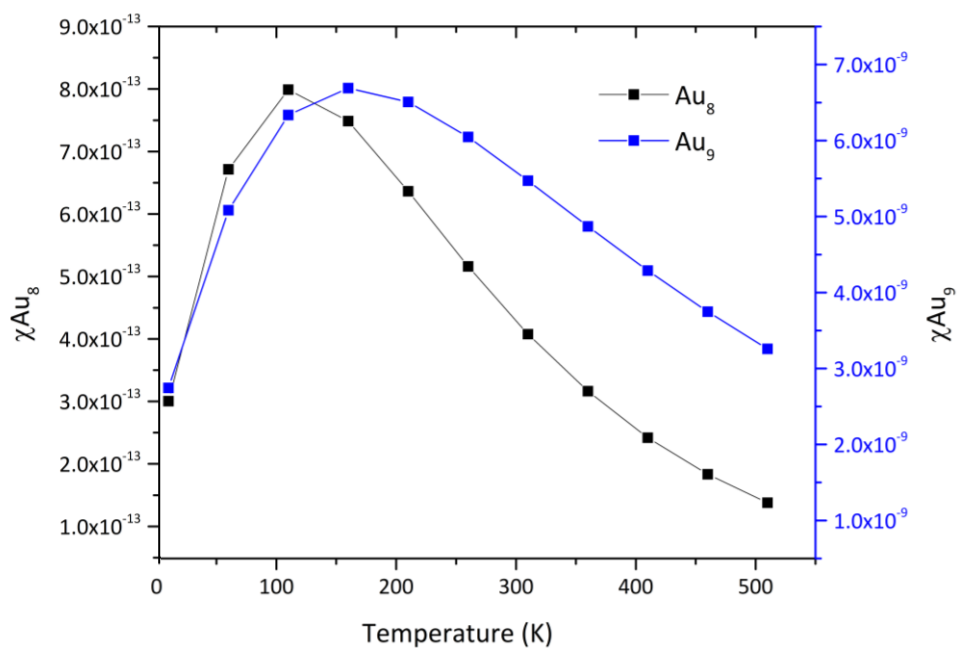


Figure 4.16: χ_{Au_8} and χ_{Au_9} at 1 second from Au_{10} , peaks are seen at 160 K (the temperatures at which $\chi_{Au_{10}}$ is at its lowest.)

After 1 second at the temperatures modelled, there is an increased presence of Au_2 at 410 K, illustrated in Figure 4.17. The peak for χ_{Au_2} is a consequence of aggregation of the single atoms that detach from the Au_{10} clusters, as at medium temperatures (> 350 K) there is enough energy supplied for the single atoms to diffuse widely enough across the surface to aggregate with other single atoms.

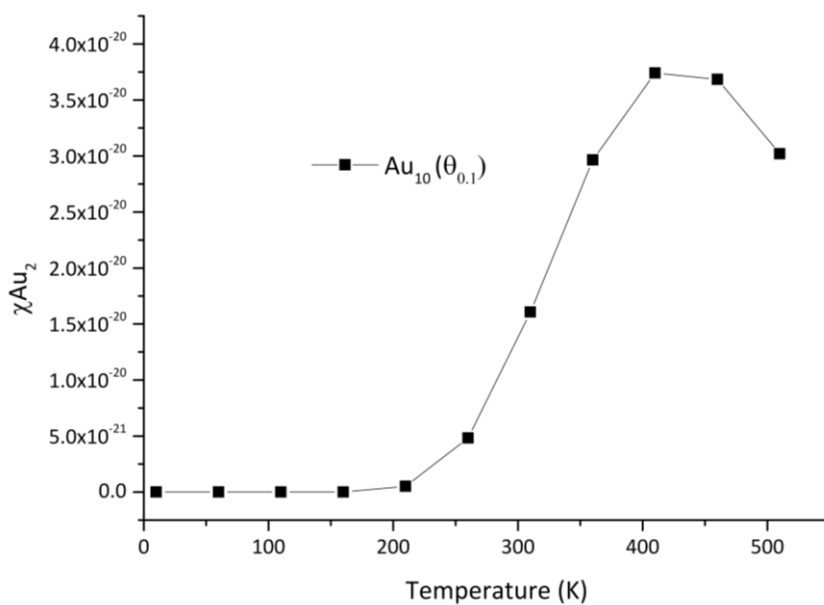


Figure 4.17: χ_{Au_2} from $Au_{10}(\theta_{0.1})$ after 1 second with temperature (K)

The low conversion from Au₁₀ clusters implies that the Au_n/MgO systems is at its most stable when the Au₁₀ clusters are retained. That being said, there are changes to the system over the time frames that show that the system is still dynamic and digestion processes occur leading to varying cluster sizes.

Conclusions

We have employed a combination of DFT and microkinetic simulations to unravel the Ostwald ripening and digestion of Au NPs on MgO(001) for cluster sizes 1 to 10 atoms. From calculated adsorption, binding, cohesion energies and charge transfer analyses, it is established that the growth of Au NPs leads to increasing interactions between the metal atoms and reduced interactions of the metal cluster with the surface.

It can be concluded from the DFT data presented that the Ostwald ripening processes on pristine MgO(001), with no capping agents or other stabilising factors, have low energy barriers (>1.05 eV), which aids subsequent cluster formation, leading to increased stability of the system.

Furthermore, although the greatest stability is found in the form of Au₁₀ clusters, the energetic barriers to form larger clusters are not linear, resulting in the observation of odd/even trends. This suggests that even numbered clusters are more favourable than odd numbered clusters, which are more prone to single atom attachment. This is due to the stabilisation of the unpaired charge from single atom.

During the ripening simulation, at lower initial occupations ($\theta_{0.1}$), the single atoms remain for longer on the surface, being less likely to aggregate in the time frames. For all initial occupations, up to temperatures of 160 K the system is stable and single atoms are retained in the time frames given. At temperatures higher than 160 K, there is enough energy in the system for the atom to overcome the ripening barrier and diffuse across the surface, entering into the unit cells of other gold atoms, creating Au₁₊₁ systems. As this process has a low barrier (0.29 eV), it occurs quickly (within the first 0.02 s) and it then takes a bit more time (a further few milliseconds) for the atoms to diffuse further and for aggregation to follow. The rapid change to Au₁₀ systems is due to the increasing stability of larger cluster sizes. Driven by thermodynamics, the atoms continue to diffuse and aggregate, changing the state of the system to the one most stable in this simulation – one with Au₁₀ clusters.

When we start the digestion simulation with the most stable species within the confines of the system studied - the Au₁₀ cluster, the data shows the surface to be dynamic, whereby at certain temperatures, detachment and diffusion processes come into play. The data shows

at temperatures between 100 and 200 K detachment occurs, producing Au₉ and Au₈ clusters. As the temperature of the system increases, diffusion processes become more widespread and the detached atoms now move further across the surface to meet other atoms with which they aggregate to form smaller clusters and help to re-form Au₁₀ clusters.

It is hoped that by studying the stability of small clusters on magnesia at suitable temperatures and dispersions, an understanding of growth processes for gold on this surface will elude to more ideas to retain their stability. Further research should aim for a more in depth study of the effects of a wider range of temperatures and coverages, as well as the impact of stabilising influences such as surface defects,³⁷ or surface adsorbates³⁸ particularly those that have been utilised by experimental groups. It would also be of great importance to simulate sintering processes involving the attachment of small clusters, as well as single atoms, to simulate the coalescence mechanism of sintering. An attempt at modelling the coalescence ripening mechanism should also be made to better understand how the ripening mechanisms might compete under various conditions.

References

1. Mostafa, S. *et al.* Shape-Dependent Catalytic Properties of Pt Nanoparticles. *J. Am. Chem. Soc.* **132**, 15714–15719 (2010).
2. Wang, Y. *et al.* Shape-controlled synthesis of Pt particles and their catalytic performances in the n-hexadecane hydroconversion. *Catal. Today* **259**, 331–339 (2016).
3. Berg, R. van den *et al.* Structure sensitivity of Cu and CuZn catalysts relevant to industrial methanol synthesis. *Nat. Commun.* **7**, 20457–20465 (2016).
4. Haruta, M. Size-and support-dependency in the catalysis of gold. *Catal. Today* **36**, 153–166 (1997).
5. Fu, Q., Weber, A. & Flytzani-Stephanopoulos, M. Nanostructured Au–CeO₂ catalysts for low-temperature water–gas shift. *Catal. Letters* **77**, (2001).
6. Wynblatt, P. & Gjostein, N. A. Particle growth in model supported metal catalysts—I. Theory. *Acta Metall.* **24**, 1165–1174 (1976).
7. Baldan, A. Review Progress in Ostwald ripening theories and their applications to nickel-base superalloys Part I: Ostwald ripening theories. *J. Mater. Sci.* **37**, 2171–2202 (2002).
8. Campbell, C. T. *et al.* The Effect of Size-Dependent Nanoparticle Energetics on Catalyst Sintering. *Science (80-.)*. **298**, 811–814 (2002).
9. Campbell, C. T. The Energetics of Supported Metal Nanoparticles: Relationships to Sintering Rates and Catalytic Activity. *Acc. Chem. Res.* **46**, 1712–1719 (2013).
10. Bartholomew, C. H., Fuentes, G. A. (Gustavo A. . & International Symposium on Catalyst Deactivation (7th : 1997 : Cancún, M. *Catalyst deactivation 1997 : proceedings of the international symposium, Cancun, Mexico, October 5-8, 1997.* (Elsevier, 1997).
11. Hansen, T. W., DeLaRiva, A. T., Challa, S. R. & Datye, A. K. Sintering of Catalytic Nanoparticles: Particle Migration or Ostwald Ripening? *Acc. Chem. Res.* **46**, 1720–1730 (2013).
12. Elofsson, V. *Nanoscale structure forming processes.* (Linköping University Electronic Press, 2016).

13. Ostwald ripening. in *IUPAC Compendium of Chemical Terminology* (IUPAC). doi:10.1351/goldbook.O04348
14. Ratke, L. & Voorhees, P. W. *Growth and Coarsening : Ostwald Ripening in Material Processing*. (Springer Berlin Heidelberg, 2002).
15. Su, Y.-Q., Liu, J.-X., Filot, I. A. W. & Hensen, E. J. M. Theoretical Study of Ripening Mechanisms of Pd Clusters on Ceria. *Chem. Mater.* **29**, 9456–9462 (2017).
16. Campbell, C. T. & Sellers, J. R. V. Anchored metal nanoparticles: Effects of support and size on their energy, sintering resistance and reactivity. *Faraday Discuss.* **162**, 9 (2013).
17. Datye, A. K., Xu, Q., Kharas, K. C. & McCarty, J. M. Particle size distributions in heterogeneous catalysts: What do they tell us about the sintering mechanism? *Catal. Today* **111**, 59–67 (2006).
18. Barcaro, G. & Fortunelli, A. Structure and diffusion of small Ag and Au clusters on the regular MgO (100) surface. *New J. Phys.* **9**, 22–22 (2007).
19. Perdew, J., Burke, K. & Ernzerhof, M. Generalized Gradient Approximation Made Simple. *Phys. Rev. Lett.* **77**, 3865–3868 (1996).
20. Grimme, S., Antony, J., Ehrlich, S. & Krieg, H. A consistent and accurate ab initio parametrization of density functional dispersion correction (DFT-D) for the 94 elements H-Pu. *J. Chem. Phys.* **132**, 154104–1007 (2010).
21. Blöchl, P. E. Projector augmented-wave method. *Phys. Rev. B* **50**, 17953–17979 (1994).
22. Kresse, G. & Joubert, D. From ultrasoft pseudopotentials to the projector augmented-wave method. *Phys. Rev. B* **59**, 1758–1775 (1999).
23. Chorkendorff, I. (Ib) & Niemantsverdriet, J. W. *Concepts of modern catalysis and kinetics*. (Wiley-VCH, 2007).
24. Eyring, H. & Polanyi, M. Concerning simple gas reactions. *ZEITSCHRIFT FUR Phys. CHEMIE-ABTEILUNG B-CHEMIE DER Elem. AUFBAU DER Mater.* **12**, 279–311 (1931).
25. Ptáček, P., Šoukal, F. & Opravil, T. Introduction to the Transition State Theory. in *Introducing the Effective Mass of Activated Complex and the Discussion on the Wave Function of this Instanton* (InTech, 2018). doi:10.5772/intechopen.78705

26. Wigner, E. The transition state method. *Trans. Faraday Soc.* **34**, 29 (1938).
27. Henkelman, G., Arnaldsson, A. & Jónsson, H. Theoretical calculations of CH₄ and H₂ associative desorption from Ni(111). Could subsurface hydrogen play an important role? *J. Chem. Phys.* **124**, 044706 (2006).
28. Geyer, R. *et al.* Methods for Determining the Metal Crystallite Size of Ni Supported Catalysts. *Chemie Ing. Tech.* **84**, 160–164 (2012).
29. Guggilla Vidya Sagar, Pendyala Venkat Ramana Rao, Chakravartula S. Srikanth, A. & Chary*, K. V. R. Dispersion and Reactivity of Copper Catalysts Supported on Al₂O₃–ZrO₂. *J. Phys. Chem. B* **110**, 13881–13888 (2006).
30. Bönnemann, H. *et al.* An SiO₂-Embedded Nanoscopic Pd/Au Alloy Colloid. *Eur. J. Inorg. Chem.* **2000**, 819–822 (2000).
31. Peng, Y. *et al.* Two-step nucleation mechanism in solid–solid phase transitions. *Nat. Mater.* **14**, 101–108 (2015).
32. Yildirim, H., Kara, A., Durukanoglu, S. & Rahman, T. S. Calculated pre-exponential factors and energetics for adatom hopping on terraces and steps of Cu(100) and Cu(110). *Surf. Sci.* **600**, 484–492 (2006).
33. Damianos, K. & Ferrando, R. Determination of the structures of small gold clusters on stepped magnesia by density functional calculations. *Nanoscale* **4**, 1101–1108 (2012).
34. Campisi, S. *et al.* DFT-Assisted Spectroscopic Studies on the Coordination of Small Ligands to Palladium: From Isolated Ions to Nanoparticles. *J. Phys. Chem. C* **124**, 4781–4790 (2020).
35. Han Myoung Lee, Maofa Ge, B. R. Sahu, P. Tarakeshwar, A. & Kim*, K. S. Geometrical and Electronic Structures of Gold, Silver, and Gold–Silver Binary Clusters: Origins of Ductility of Gold and Gold–Silver Alloy Formation. *J. Phys. Chem. B* **107**, 9994–10005 (2003).
36. Nijamudheen, A. & Datta, A. Odd–even oscillations in structural and optical properties of gold clusters. *J. Mol. Struct. THEOCHEM* **945**, 93–96 (2010).
37. Zhen Yan, Sivadinarayana Chinta, Ahmed A. Mohamed, John P. Fackler, Jr., A. & Goodman*, D. W. The Role of F-Centers in Catalysis by Au Supported on MgO. *J. Am.*

Chem. Soc. **127**, 1604–1605 (2005).

38. Brown, M. A., Carrasco, E., Sterrer, M. & Freund, H.-J. Enhanced Stability of Gold Clusters Supported on Hydroxylated MgO(001) Surfaces. *J. Am. Chem. Soc.* **132**, 4064–4065 (2010).

Chapter 5

Monte Carlo global optimisation

Introduction

Among the difficulties to model supported NP systems, i.e. Au/MgO, finding the global minima geometry is very challenging and requires huge computational power. As previously described, a DFT methodology was employed in order to obtain low energy Au clusters. This methodology was successful due to the planar nature of the very small Au clusters. However, for other supported systems, rather than build up the calculation through mathematics alone, as performed with DFT, the use of parameters derived from experimental data can be used to reduce the reliance on mathematical equations for quantum behaviour. The reduction in computational time is an advantage of these more empirical methods, the main disadvantage is the restriction of their use to specific systems to which they have been benchmarked.¹ Empirical data is used in the production of interatomic potentials, which are mathematical functions used to calculate the potential energy of a system of atoms with particular positions in space. Some of these more empirical methodologies, such as the Monte Carlo global optimisation employed here, couple interatomic potentials with algorithms, e.g. basin hopping, to aid in the construction of the PES and the search for global minima for more complex and larger systems of interest (> 100 atoms). Potentials can vary in their complexity and this scales with the number of systems they can be used to describe, the following section describes two very simple potentials used to describe simple systems, e.g. diatomic molecules.

Simple pair potentials

Lennard-Jones (LJ) and Morse are examples of empirical pair potentials, these simple interatomic potentials are used to describe the interactions between pairs of atoms. The LJ potential can be used to model weak van der Waals bonds between noble gases accurately,² it does a less accurate job when modelling the interactions between covalently bonded molecules and within metallic systems. The LJ represented in Figure 5.1, takes the form:

$$V(r) = 4\varepsilon \left[\left(\frac{\sigma}{r} \right)^{12} - \left(\frac{\sigma}{r} \right)^6 \right] \quad (5.1)$$

where r is the distance between any two atoms and ε (depth of the well) and σ (the distance at which the potential between the two particles is zero) are fitting parameters from the known properties of the system.

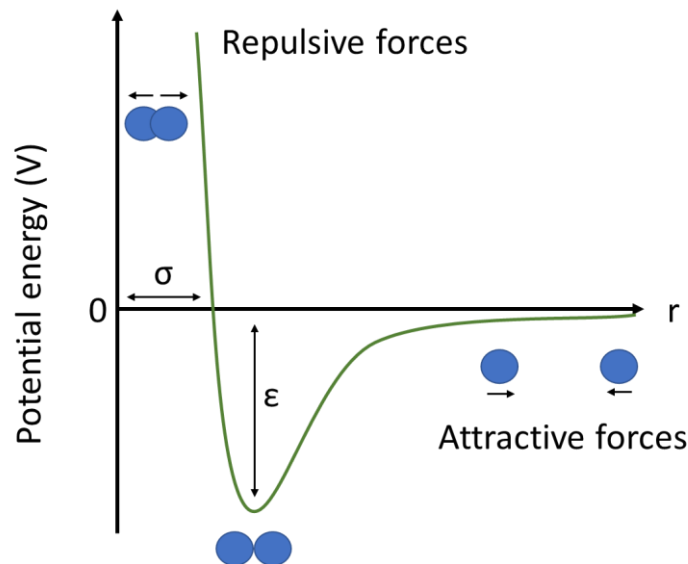


Figure 5.1: Representation of a Lennard-Jones potential

When atoms start at a non-interacting distance and move closer together, the fluctuations of the electron clouds of the atoms produce temporary dipoles that result in attractive forces between them, this interaction decays with distance $\left(\frac{1}{r^6}\right)$. Once the atoms are close enough, these interactions form a bond between the atoms, the length of which, found at the bottom of the well, is known as the equilibrium bond length. If the atoms continue to move closer, then the electron clouds overlap and the interaction between them becomes unfavourable, this causes a repulsive interaction which forces the atoms further apart again. The repulsive interactions decay much faster with distance than the attractive interactions, $\left(\frac{1}{r^{12}}\right)$.

The Morse potential³, graphically represented in Figure 5.2, is similar to LJ but better describes the attractive interactions when a bond is formed. Equation 5.2 defines this potential:

$$V(r) = \varepsilon \left[e^{-2\alpha(r-r_e)} - 2e^{-\alpha(r-r_e)} \right] \quad (5.2)$$

$$a = \sqrt{\frac{k_e}{2\varepsilon}}$$

Where r_e is equilibrium bond length and α is the width of the well, with k_e the force constant at the bottom of the well.

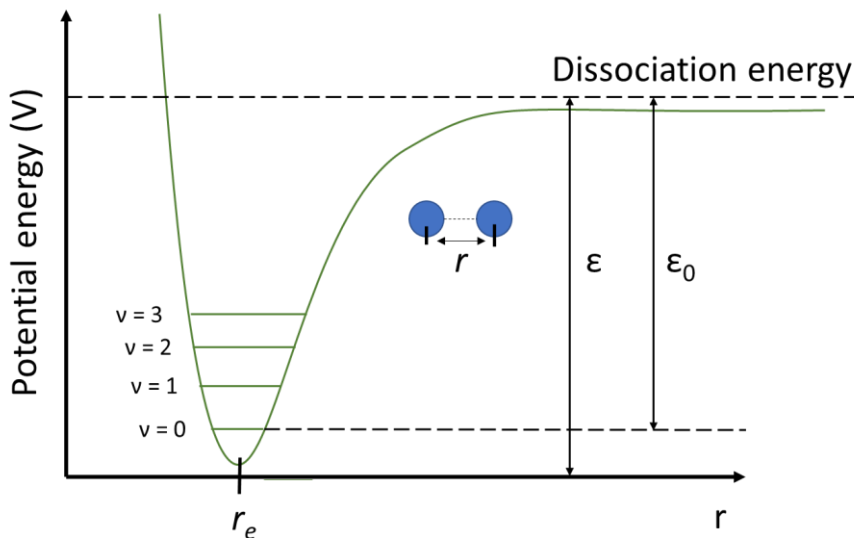


Figure 5.2: Representation of a Morse potential.

Pair potentials such as the two described, are unable to take into account the effect of other species around the atom pair simulated and they are poor representations of real systems for this reason. To make them more applicable, corrections can be made, for example the Buckingham potential is an adapted version of the LJ, where the repulsive interactions are simulated using an exponential function. This provides a better description of closed shell electron clouds and their stronger repulsive forces.

These simple examples shown how systems can be represented by interatomic potentials. However, as Au/MgO is a supported system, the potentials used to represent the interactions between atoms are much more complex.

Methodology

Empirical potentials

A Monte Carlo global optimisation methodology, as described by Ferrando *et al.*^{4,5} using interatomic potentials has been employed and evaluated for its efficacy in modelling the Au_n/MgO ($n \leq 20$) system. The method utilises a many-body potential (referred to as a Gupta-type potential) derived from the second-moment approximation to the tight binding model (SMATB)⁶ to model metal-metal (inter-cluster) interactions (E_i^{MM} , Equation 5.4) and a combination of a Morse and a periodic cosine function for the metal-surface interactions (E_i^{MS} , Equation 5.7).⁷

The total binding energy of the system is obtained from the combination of these potentials:

$$E_{tot} = \sum_{i=1}^N (E_i^{MM} + E_i^{MS}) \quad (5.3)$$

In a monometallic system, the many-bodied potential, E_i^{MM} is the sum of an attractive part (E_i^a , Equation 5.5) and a repulsive part (E_i^r , Equation 5.6):

$$E_i^{MM} = E_i^a + E_i^r \quad (5.4)$$

$$E_i^a = - \left\{ \sum_{j \neq i, r_{ij} < r_c} \xi^2 \exp \left[-2q \left(\frac{r_{ij}}{r_0} - 1 \right) \right] \right\}^{\frac{1}{2}} \quad (5.5)$$

$$E_i^r = \sum_{j \neq i, r_{ij} < r_c} A \exp \left[-p \left(\frac{r_{ij}}{r_0} - 1 \right) \right] \quad (5.6)$$

where r_{ij} is the distance between atoms i and j , r_c is the cut off radius, and r_0 is the nearest-neighbour distance. The parameter set (A , ξ , p , q and r_0) is fitted to experimental bulk values of cohesive energy, lattice constrained parameters and independent elastic constants. After fitting to the bulk properties, two independent parameters (p and q) that determine the range of the repulsive and attractive terms, are required. For Au, the values of these parameters⁴ are shown in Table 5.1:

Metal	A	ξ	p	q	r_0
Au	0.20957	1.8153	10.139	4.0330	2.885

Table 5.1: Au parameter set of the many-bodied metal-metal potential

On addition of a support, e.g. MgO, then an additional potential is used to model the interaction of the cluster atoms and the support (E_i^{MS}). As described, this is achieved using a Morse like potential for the energy dependence with elevation in the z direction and a periodic cosine function to model the dependence with regard to its position and coordination. This is shown below:

$$E_i^{MS} = \sum_{i=1}^N E_i(x_i, y_i, z_i, Z_i) \quad (5.7)$$

where N is the number of metal atoms; x_i , y_i , and z_i relate to the position of atom i above the surface, z_i depicting elevation and Z_i is the coordination number.

$$E_i(x_i, y_i, z_i, Z_i) = a_1(x_i, y_i, Z_i) \{ e^{-2a_2(x_i, y_i, Z_i)[z_i - a_3(x_i, y_i, Z_i)]} - 2e^{-a_2(x_i, y_i, Z_i)[z_i - a_3(x_i, y_i, Z_i)]} \}$$

$$a_j(x_i, y_i, Z_i) = b_{j1}(x_i, y_i) + b_{j2}(x_i, y_i) e^{\frac{Z_i}{b_{j3}(x_i, y_i)}}$$

$$b_{jk}(x_i, y_i) = c_{jk1} + c_{jk2} \{ \cos(\chi x_i) \} + \{ \cos(\chi y_i) \} + c_{jk3} \{ \cos(\chi(x_i + y_i)) \}$$

$$+ c_{jk3} \{ \cos(\chi(x_i - y_i)) \} \quad (5.8)$$

Where $\chi = 2\pi/a$, with a as the oxygen-oxygen distance of the oxide support; the x and y coordinates and a nearest neighbour cut off of $1.25 r_0$.

Monte Carlo global optimisation

In order to find the global minimum of the Au/MgO system a sampling method is also employed. Once the energy of the system with the atoms in a given position is calculated, using the potentials described above, then a Monte Carlo simulation makes random movements to species present in a system, sampling a large number of configurations. By using empirical potentials to describe the energy of the system, thousands of atomic moves can be made to the system along with the calculation of the energy, in a relatively short space of time (runs of 10000 moves were completed in less than 30 minutes for the system described).

The way in which the system performs changes to the atomic positions (moves) is defined⁸ to enable faster determination of global minima for different system types. For example, a single atom move, performs displacement of a random single atom in the cluster to another position within a spherical shell centred on the original position of the displaced atom. However, the greater the size of the system, the greater the configurational search space and the slower finding the global minima will be. Consequently, moves that make larger changes to the system in one step might achieve faster optimisation, case in point, the shake move, where the same random displacement in a single atom move is made to all of the atoms in system.⁹

Additionally, for specific types of systems, different moves maybe needed. For instance, in multi-metallic systems, where homotops are present, exchange moves are vital to account for the increased number of possible configurations. Homotops are defined as clusters with the same size, composition and geometrical arrangement, differing only in the way in which the different atom types are arranged. Exchange moves therefore allow the “swapping” of the different atoms types to better explore the PES. However, for the supported

monometallic system modelled here, exchange moves would not be suitable as they would be exchanges with an atom of the same element.

For the Monte Carlo global optimisation performed on the Au_n/MgO ($n = 5-20, 30, 40, 50$ and 70) systems, each calculation was run for 10000 Monte Carlo steps, with Brownian type moves. In this type of move atoms undergo a very short Langevin dynamics simulation (200 simulation steps, with a time step set to 5 fs) at high temperature (up to 2000 K). Brownian moves proved to be very efficient for the optimization of large clusters ($N > 200$),⁸ therefore they were performed for optimisation of this system.

Monte Carlo optimisation algorithms

From the energy calculations and the configurational sampling achieved with Monte Carlo, the potential energy surface (PES) is built up from a global optimisation technique called “basin hopping”.¹⁰ Basin-hopping (BH) is a global optimisation technique that occurs in two-phases, combining a global stepping algorithm, performing a random change of atomic arrangement, followed by a local minimization at each step. The new configuration is either accepted into the modified PES or rejected based on a minimized function value. By altering Figure 2.1, a graphical representation of the “basins” is shown in Figure 5.3. The PES is built-up by associating each point of the configuration space with the energy of its closest local minimum and is transformed into a multidimensional staircase function creating a simplified representation of the systems energy.

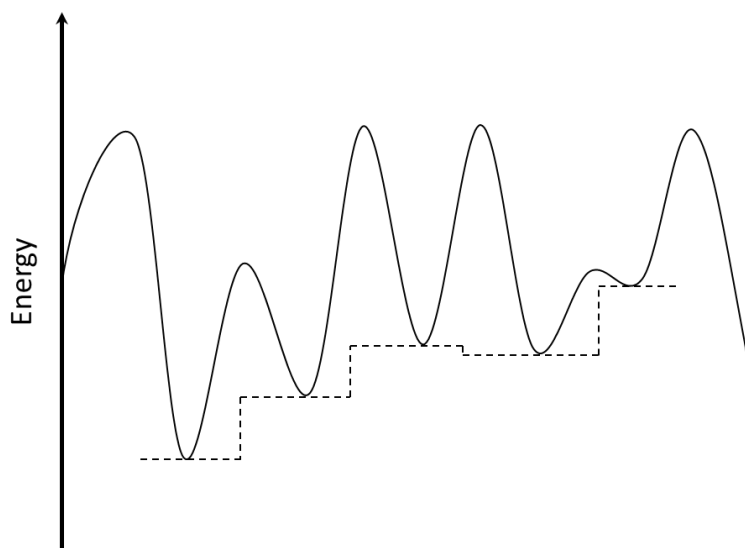


Figure 5.3: PES of an arbitrary system with basins of the type calculated by the basin hopping algorithm shown.

The inclusion of a parallel excited walker algorithm (PEW)¹¹ improves upon the results from the BH algorithm as it allows for better optimisation of more “rugged” systems, where the

PES has a greater number of “basins”. More successful optimisation is achieved for these systems by inclusion of order parameters, which prevents the optimisation from getting stuck in a basin and allows the system to reach the bottom of the basins faster. The two order parameters used for these calculations are the common neighbour analysis (CNA) and the surface contact. The CNA gives an analysis of the local environment of the pairs of atoms and can provide direct interpretation of various features in terms of atomic structure. It can also be used to identify atoms in particular environment, such as FCC, HCP, BCC or icosahedral. This can help to drive optimisation toward features it finds lower in energy. The surface contact parameter is the number of cluster atoms in direct contact with the surface, this can be useful to distinguish between different cluster-surface epitaxies in the search.⁸

Results and discussion

Results from Au_{50} and Au_{70} calculations

A Monte Carlo global optimisation was run on Au_n/MgO ($n = 5-20, 50$ and 70) systems. Initial calculations concentrated on the Au_{50} and Au_{70} cluster sizes. This was to ensure that the results seen previously by Ferrando’s group could be replicated using the method described above.⁴ The searches performed by Ferrando *et al.* for systems with 30 to 500 Au atoms, were run with 200000 steps, 6 times from random initial start structures (known as unseeded optimisations), as well as some additional searches started with known structures (seeded optimisations). The searches performed here, following the methodology described with 10000 steps only, resulted in finding several of the low energy structures, determined by Ferrando *et al.*,⁴ these structures were then optimised in subsequent DFT calculations. The lowest energy structures for Au_{50} and Au_{70} are shown in Figure 5.4.

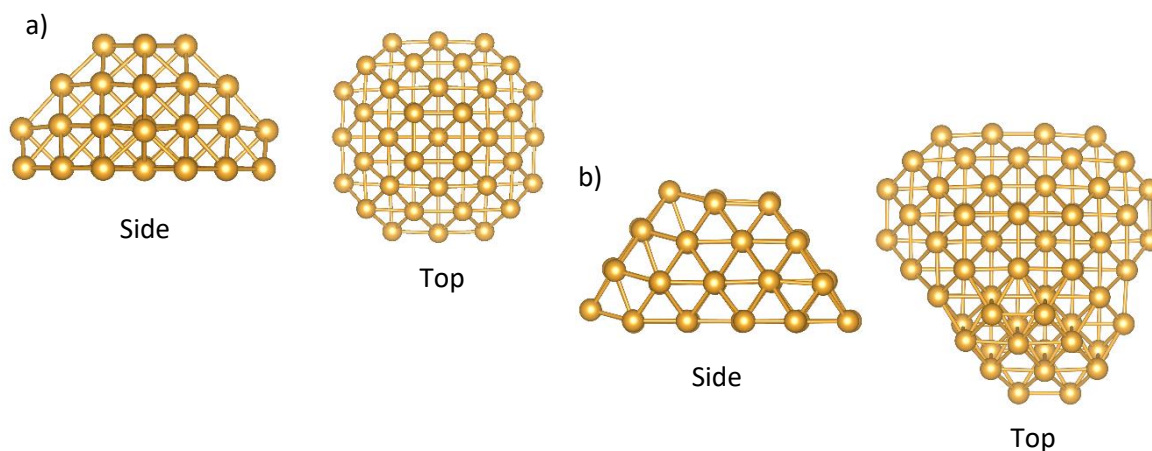


Figure 5.4: Configurations of the lowest energy structures of a) Au_{50} and b) Au_{70} , achieved after 10000 Monte Carlo steps

Both Au_{50} and Au_{70} are 3D square based pyramid type structures, with a (001) interfacial configuration. The term “interface” refers to the configuration of the Au atoms that are in direct contact with the support. Au clusters with an (001) interface have an (001) arrangement of Au atoms in contact with the surface, whilst Au clusters with a (111) interface have the hexagonal (111) arrangement in contact with the surface, see Figure 5.5 for an illustration of this.

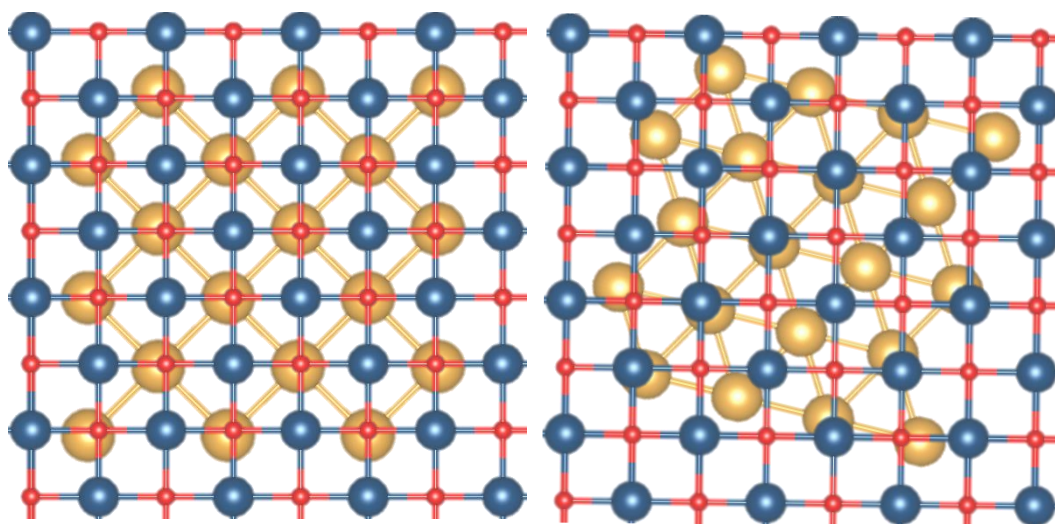


Figure 5.5: Schematic representation of a) Au (001) interface and b) Au (111) interface on MgO (001).

The shapes obtained for Au_{50} and Au_{70} in Monte Carlo were placed into DFT calculations on fixed MgO surfaces, as used in Monte Carlo optimisations, to observe any structural changes that occur under DFT optimisation. The DFT calculations on Au_{50} and Au_{70} were performed with and without the addition of dispersion corrections (D3 by Grimme,¹² as describe in Chapter 2) to account for long-range interactions. There is rearrangement within the Au_{50} cluster on optimisation, seen in Figure 5.6, it is probable that this deformation occurs to account for the strain of retaining the (001) interface. It can also be established from Figure 5.6 that while the overall shape for Au_{50} is retained in both calculations, dispersion corrections are seen to induce greater deviation of the atoms from the original configuration from Monte Carlo and the rearrangements becomes more pronounce. This is because the dispersion correction includes long-range interactions between the species, thus, more of the Au cluster atoms are influenced by the interaction with the support and affected more greatly by the strain it induces.

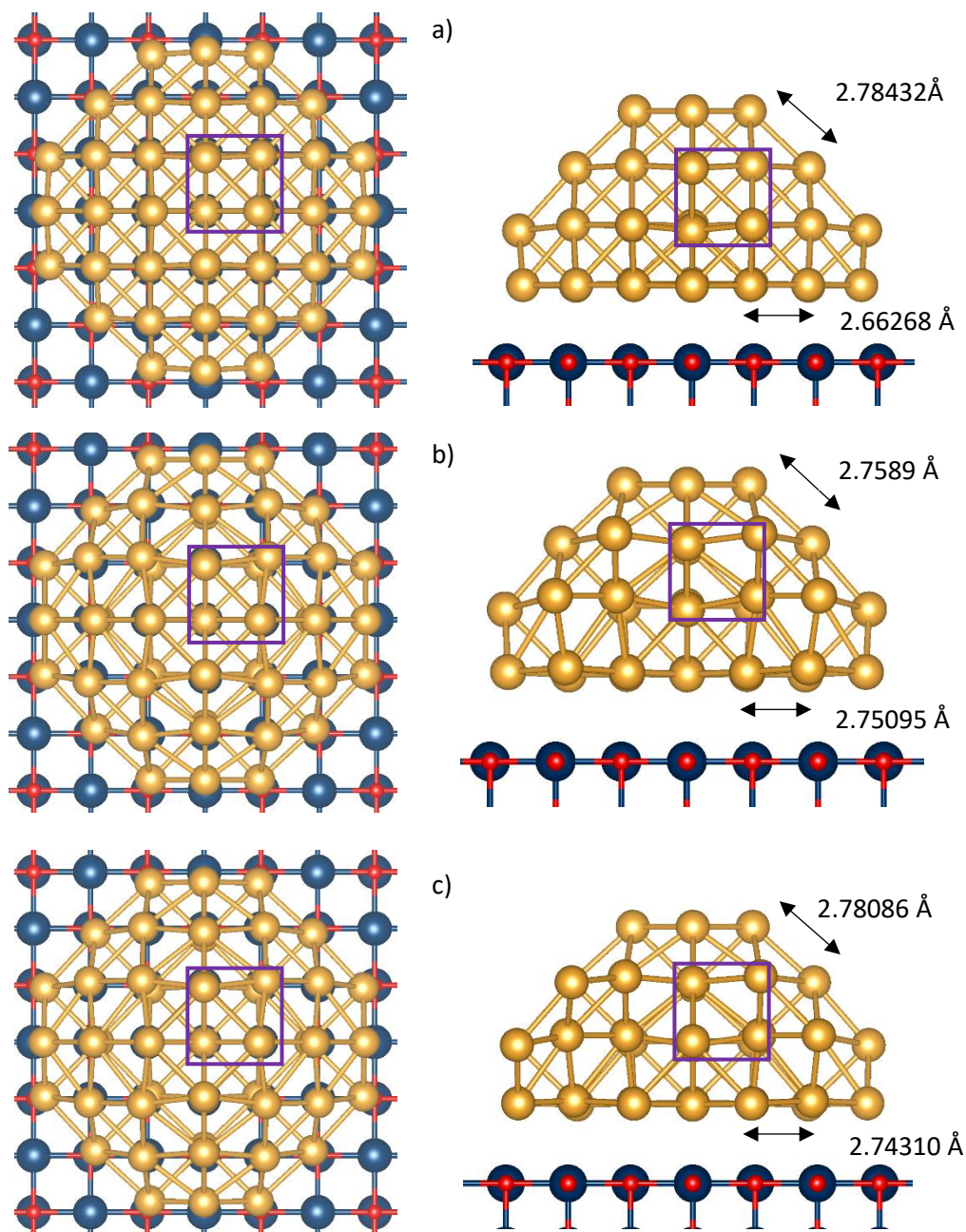


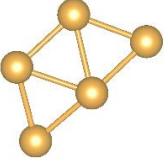
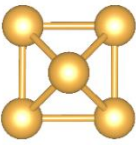

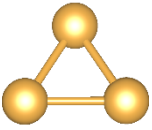
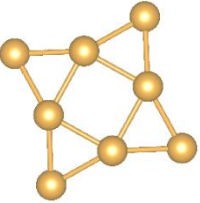
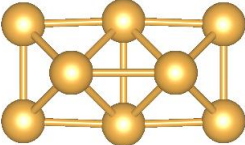
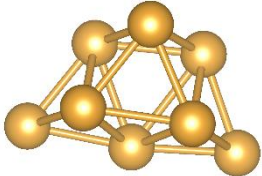
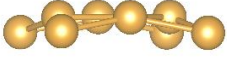
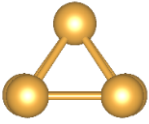
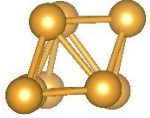
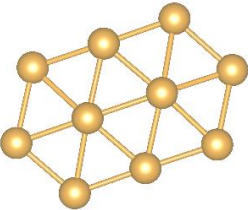
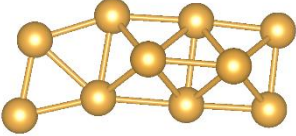
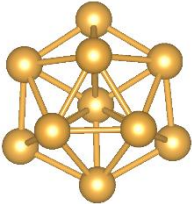

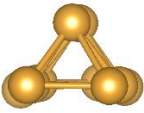
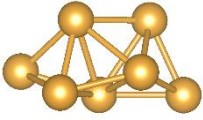
Figure 5.6: Images with some Au-Au bond distances of the lowest energy Au_{50} . Configurations are from Monte Carlo and subsequently optimised using DFT a) before DFT optimisation b) with dispersion corrections and c) without dispersion correction. The purple box frames a small portion of the structure to highlight the rearrangement of the atoms within that section.

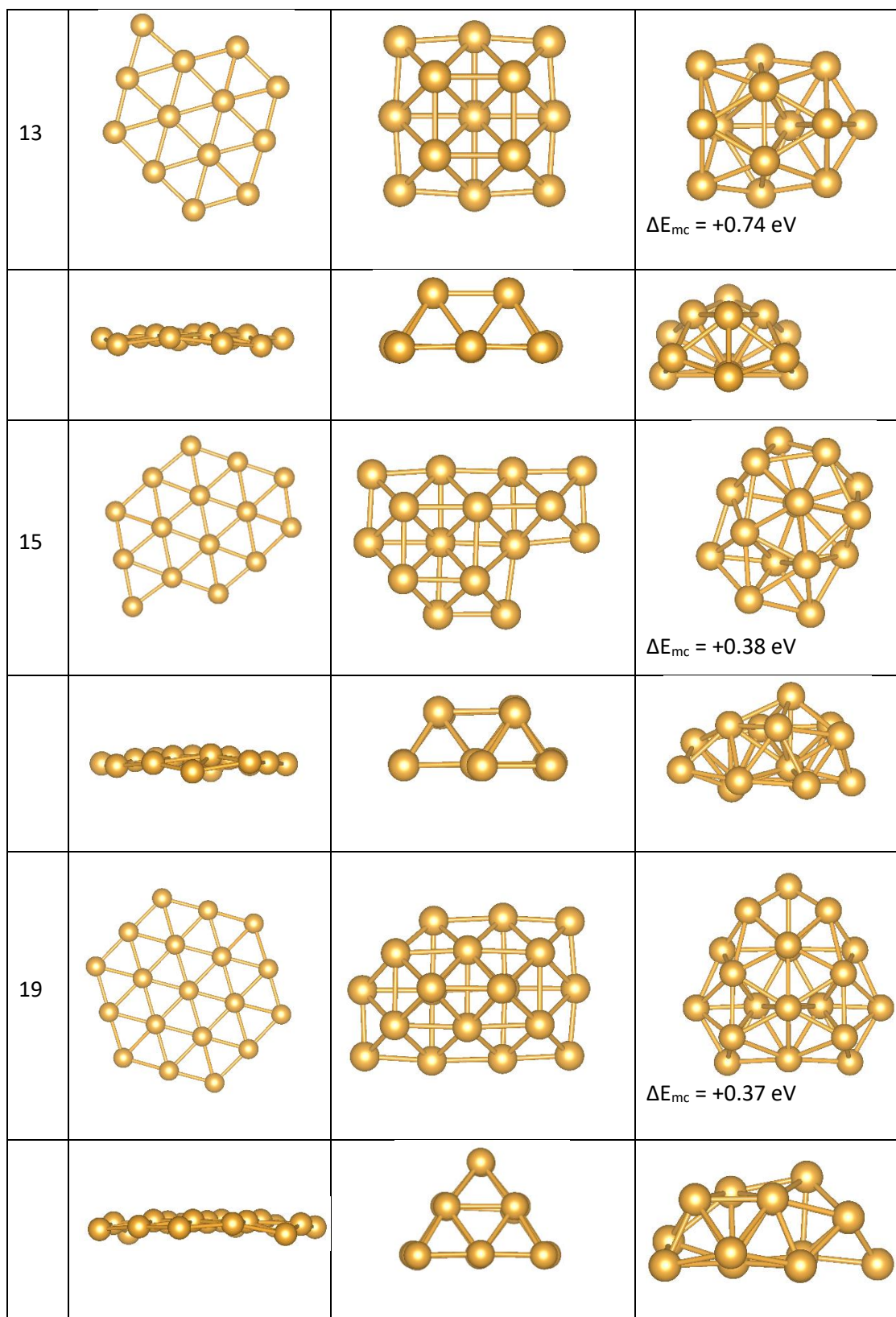
Results for Au_n/MgO ($n = 5-20$)

Many (though not all) of the lowest energy structures were found from the Monte Carlo searches performed for Au_{50} and Au_{70} , from a single 10000 step search. Thus, it was decided that the same 10000 step search, would be rigorous enough to determine low energy structures for Au_n/MgO ($n \leq 20$), as the possible configurations of the system would be significantly smaller with fewer Au atoms.

The lowest energy cluster shapes, calculated by the Monte Carlo optimisation, for the Au_n/MgO ($n = 5, 8, 10, 13, 15, 19$) systems are shown in Table 5.2. For all the sizes calculated ($n < 20$), the most stable structures found by Monte Carlo are all 3D and favour the (001) interface configuration. However, as described in Chapter 3, the lowest energy ($n < 20$) clusters calculated by DFT are all planar structures and favour a (111) interface configuration. Additionally, when the 3D, (001) interface Monte Carlo structures were subsequently optimised using DFT, the Au atoms often rearranged, implying that they were not stable structures according to the DFT methodology. Additionally, the relative energies calculated in VASP for these structures were comparatively higher than for the planar structures obtained by DFT. This shows that Monte Carlo global optimisation does not agree with DFT in its determination of the global minima of Au_n/MgO ($n = 5-20$). It also must be noted that 3D structures with a (111) interface were found by Monte Carlo but they had lower stabilities and higher energies than their (001) interface counterparts, see Table 5.2 for examples of the lowest energy, 3D (111) interface configurations found.

Table 5.2: Displaying the top view and side view of the lowest energy Au_n/MgO ($n=5, 8, 10, 13, 15, 19$) clusters optimised by DFT and Monte Carlo, the Monte carlo (111) column also shows the energy difference between the two monte carlo configurations (ΔE_{mc}).

n	DFT	Monte Carlo (lowest energy)	Monte Carlo (111)
5	 top view		
	 side view		
8			 $\Delta E_{mc} = +0.39$ eV
			
10			 $\Delta E_{mc} = +0.08$ eV
			



Discussion of the Monte Carlo method for Au_n/MgO systems.

As can be seen from Figure 5.2, the overall shape of the Au_{50} cluster obtained by Monte Carlo optimisation is retained after DFT optimisation. This implies that the empirical potentials employed by the Monte Carlo provide an adequate representation of the interactions between the atoms in Au_n/MgO systems of this size. It was previously described in the paper by Ferrando *et al.*⁴ that the potentials used in the Monte Carlo are not suitable for representing systems with small clusters ($n < 30$), due to the use of empirical data from bulk quantities, thus any inaccuracy in the results found for the Au_n/MgO ($n < 20$) system were not surprising. This is in part owing to the employment of the potentials used to describe the system. For very small supported clusters studied here, the addition of a single atom to the Au cluster can greatly change the values of parameters, such as bond lengths and coordination numbers of all the other atoms in the system. The larger the cluster size, the fewer the ratio of surface Au atoms, and the greater the ratio of atoms that have properties consistent with bulk, i.e. higher coordination numbers and therefore MC is more accurate. Therefore, the properties of a system with clusters of this size change rapidly, and the use of bulk benchmarked, empirical data is problematic.

As well as this, there are additional problems that arise from the potentials used to model the cluster surface interactions (E^{MS}). For instance, the nearest neighbour inclusion (Z) into the E_{MO} parameterisation is restricted to 0, 4 or 8, these Au coordination numbers represent single atom adsorption, an epitaxial monolayer or epitaxial bilayer, respectively. For the larger Au_n/MgO systems described in Ferrando's paper⁴ ($n = 30$ to 500), it is suggested that the use of restricted coordination numbers to describe the cluster surface interactions (E_{MO}) is a suitable approach. This is evidenced by the success in the method for finding the low energy Au structures at these sizes. However, the smaller the cluster size, the larger the ratio of atoms with co-ordination numbers varying from 0, 4 or 8, due to the increase in features such as steps, kinks and edges on the cluster topography. Thus, many of the metal-surface interactions (E^{MS}) for Au_n/MgO ($n \leq 20$) are not accurately modelled by the potential, leading to a poorer representation of how the structure is influenced by the surface. Increasing the range of coordination numbers represented by the potential could improve its use in smaller systems, however, there are additional issues that must be addressed in order to make this methodology more applicable to small, supported metal cluster systems.

Discrepancies in the shapes predicted by Monte Carlo also come from the Gupta type potential used to describe the interactions between the Au atoms in the cluster. As previously described, the parameters, A , ξ , p , q and r_0 used in the potential are constants

from experimental data that help model the Au-Au interactions (E_{MM}) for the chosen system. As these parameters are based on the properties of the system e.g. cohesive energies, lattice constants and elastic constants,¹³ when in bulk, the smaller the cluster size, the greater the proportion of atoms with non-bulk like properties and the poorer the representation of the Au-Au interactions by the potential.

An additional consideration is the so-called “metal-on-top” effect. Increased stabilisation is supplied to an atom in contact with the support from an atom placed above it, leading to a stronger adsorption of that atom to the surface. This effect is not taken into consideration as the overall adsorption energy is calculated as the sum of the energies of single atom adsorption to the support as a function of co-ordination and position on the surface.¹⁴

Interface epitaxy

The structures predicted by the Monte Carlo global optimisation are 3D structures with (001) interface. The paper by Ferrando et al.⁴ predicts a crossover in the structure at the interface after Au_{1200} , from (001) to (111). The results presented suggest the presence of another crossover, from a (111) to a (001) interface somewhere at the transition from very small cluster sizes to larger clusters sizes (somewhere after 20 atoms), as the lowest energy configuration for Au_{19} with DFT has a (111) interface. The overall retention of the structures for Au_{50} from Monte Carlo after DFT optimisation shows that the 3D (001) are at least local minima and suggests stability of this epitaxy at this size, therefore implying that this crossover could occur at $n < 50$.

The planar (111) growth of small supported clusters from DFT can be explained by the lower surface energy of Au(111) (1.137 J m^{-2}) in comparison to Au(001) (1.359 J m^{-2}),¹⁵ leading to a larger exposure of (111) at the surface. It is expected that further growth of the cluster beyond 19 atoms will result in 3D structures being formed to reduce the number of exposed surface atoms. At this point, the exposed surface will not be in contact with the support, and the crossover from a (111) to a (001) interface configuration would occur to reduce the strain induced by retention of (111) at the interface. This conclusion is supported by the calculation of mismatch in the Au/MgO(001) systems.

Mismatch

The preferable cluster morphology, i.e. flat versus 3D, is influenced by the structural mismatch between the interatomic distances, symmetry of the metals at the interface, and the preferable adsorption sites on the support as well as the relative strength of the Au–Au interactions within the cluster and the Au–MgO interactions (E_{coh}/E_{ads} ratio). In a recent

paper by the group, a mismatch calculation was devised which was performed on Au(111)/MgO(001) and Au(001)/MgO(001) systems to determine the structural mismatch.¹⁶

The mismatch is not only a function of the deviation of the interatomic distances but also the symmetry of the respective unit cells. While the difference in the interatomic distances can be determined from the relationship between the optimum bulk metal–metal distance ($d_{\text{Au–Au}}$) and the distance between the most favoured adsorption sites of a single adatom (O–O distance), in order to measure the influence of the symmetry, further information regarding the adsorption sites on the surface as well as at the cluster interface is required. As the overall mismatch results from the combination of both contributions, the measure needed to consider both, into a single value which allows for the comparison of e.g. two materials with the same symmetry but different interatomic distances with two other materials with different unit cell shapes but identical interatomic distances.

To calculate the mismatch between the Au interface layers and MgO (001), the structural data from optimised geometries of an Au(111) and Au(001) monolayer and the slab models of the MgO support was used. As shown in Figure 5.7, the distance (a and b) between the Au atoms in the (111) monolayer was found to be 2.74 Å with an angle of 60° (ϕ). For the Au(001) monolayer, the Au–Au bond distance was 2.752 Å, with an angle of 90° (ϕ). The MgO surface has an angle of 90° (θ) and a distance of 2.96642 Å (k and l) between the O atoms, the preferable adsorption site. The orientation between the cluster and the surface was optimised by rotating the cluster around angle α during the mismatch calculation. For Au(001)/MgO(001), where both materials have the same lattice angles, $\alpha = 0^\circ$ and for Au(111)/MgO(001) an angle $\alpha = 15^\circ$ was found for optimum orientation. The values of α agrees well with the calculated structures of the supported clusters. For example, Au₁₉/MgO shows an angle of 14.91° between the surface and the cluster.

The local mismatch (m_p) at the atom of each cluster atom is defined as the distance between the rotated cluster atom and a preferable adsorption site. The value is divided by the average length of the cell vectors to obtain a size consistent result. This means that the same value is obtained if the size of all vectors is scaled by the same factor.

The average mismatch (m_N) is therefore measured with the following Equation (5.9), where r is the radius, with $n(r)$ being the number of points within radius r , m_p is the local mismatch:

$$m_N(r) = \sum_r m_p(r_i) \cdot n(r)^{-1} \quad (5.9)$$

The initial change of the average mismatch with increasing radius r (the slope) describes the structural strain building up during the interfacial growth of the cluster on the surface.

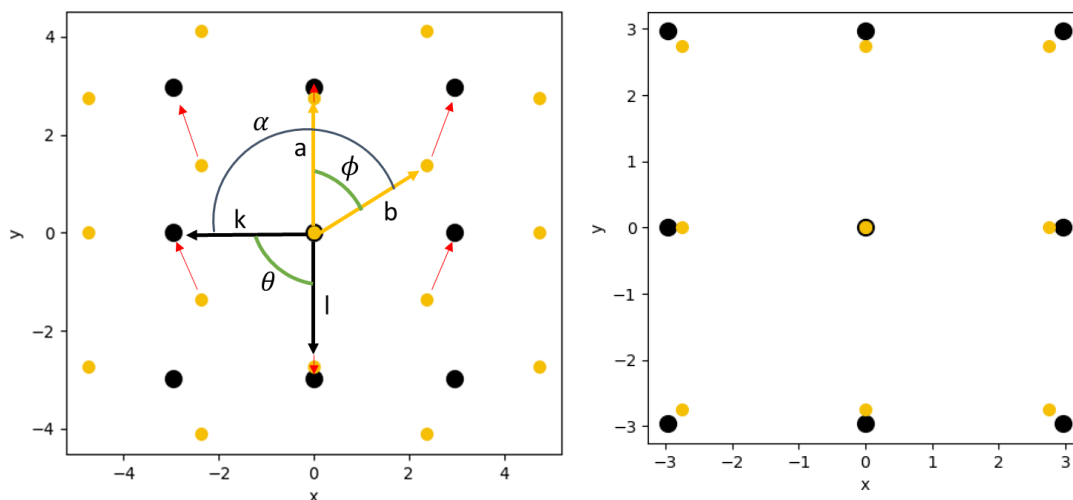


Figure 5.7: Schematic representation of the a) Au(111) and the b) Au(001) systems both on MgO(001). Preferable adsorption sites of the support (black, defined by the vectors k and l , angle defined by θ) and cluster atoms (yellow, defined by the vectors a and b , angle defined by ϕ). a defines the angle of the rotation of the cluster with respect to the support. The red arrows display the local mismatch (m_N) of the first neighbour cluster atoms.

As shown in Figure 5.8, the average mismatch $m_N(r)$ of the Au monolayers increases linearly with increasing r before converging to a value depending only on the support material. The initial slope of the mismatch $m_N(r)$ is a descriptor for the increasing structural strain on a growing cluster and the magnitude of the structural deformation needed for an ideal fit. The slope is less steep for Au(001)/MgO(001) than for Au(111)/MgO(001), 0.057 and 0.33 respectively. This implies there is lower mismatch for Au(001)/MgO(001) resulting in significantly less strain in the Au(001) system. Therefore an Au(001) interface is more favourable. However, the surface energy of Au(001) is higher (1.359 Jm^{-2}) than of Au(111) (1.137 Jm^{-2}). This results in competing forces, i.e. at small NP the strain is less important than the surface energy, as the NP grows the strain becomes more important. The difference in surface energy leads to an (111) exposed surface being more favourable and explains the stabilisation of the planar Au(111) clusters on the MgO support in our calculations. Yet, as the cluster grows, so does the epitaxial area, leading to increasing strain in the Au cluster. This means, that at a certain size, a change from (111) to a (001) interface can be expected to reduce the strain.

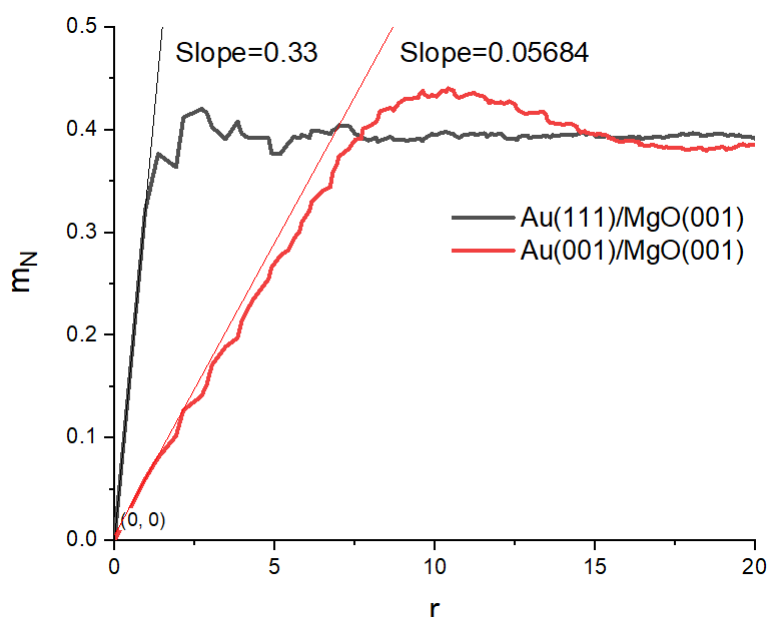


Figure 5.8: Graphical representation of the interfacial mismatch ($m_N(r)$) between an Au(111) and an Au(001) cluster with an MgO(001) support with increasing r .

Conclusions

The Monte Carlo global optimisation method, which uses potentials to describe the interactions between atoms, does not find global minima structures for the Au_n/MgO system, where $n < 20$ atoms. This is for several reasons. Firstly, the empirical data used by the potentials is fitted to bulk quantities. The properties of clusters at sizes such as these differ from that of the bulk, as the smaller the nanoparticle the greater the ratio of surface to bulk atoms. Secondly, the potential used here to describe the interaction of the Au cluster with the MgO support calculates energies based on a fixed Au co-ordination numbers, notably, coordination numbers associated with an Au atom being isolated on the surface, in a monolayer environment and a bilayer environment, 0,4 and 8 respectively. The average coordination number of atoms in small metal clusters are much lower than they would be in the bulk. Therefore, the potential used is not fitted to this system to predict the interactions with the support of clusters at these sizes accurately.

Au_n/MgO clusters below 20 atoms adopt 2D shapes with an Au(111) epitaxy in contact with the MgO support. This is owing to the lower surface energy of Au(111) in comparison to Au(001). From the combined work here with the work of Ferrando, with clusters of greater sizes, and the calculation of Au/MgO mismatch performed, it is suggested that the clusters will see a transition away from the Au(111) epitaxy to form 3D structures with (001) epitaxy as the cluster grows. The stability of (001) epitaxy 3D structures will increase with size, and although the exact size of the cluster at this crossover is not known, it is likely to be between 20 and 50 atoms.

References

1. Ferrando, R., Fortunelli, A. & Johnston, R. L. Searching for the optimum structures of alloy nanoclusters. *Phys. Chem. Chem. Phys.* **10**, 640–649 (2008).
2. Adams, J. B. Bonding Energy Models. in *Encyclopedia of Materials: Science and Technology* 763–767 (Elsevier, 2001). doi:10.1016/B0-08-043152-6/00146-7
3. Morse, P. M. Diatomic Molecules According to the Wave Mechanics. II. Vibrational Levels. *Phys. Rev.* **34**, 57–64 (1929).
4. Ferrando, R. *et al.* Structures of metal nanoparticles adsorbed on MgO(001). I. Ag and Au. *J. Chem. Phys. II. Pt Pd J. Chem. Phys.* **130**, 174702–174703 (2009).
5. Goniakowski, J. *et al.* Structures of metal nanoparticles adsorbed on MgO(001). II. Pt and Pd. *J. Chem. Phys.* **130**, 174703 (2009).
6. Cleri, F. & Rosato, V. Tight-binding potentials for transition metals and alloys. *Phys. Rev. B* **48**, (1993).
7. Vervisch, W., Mottet, C. & Goniakowski, J. Theoretical study of the atomic structure of Pd nanoclusters deposited on a MgO(100) surface. *Phys. Rev. B* **65**, 245411 (2002).
8. Rossi, G. & Ferrando, R. Searching for low-energy structures of nanoparticles: a comparison of different methods and algorithms. *J. Phys. Condens. Matter* **21**, 084208 (2009).
9. Rossi, G. & Ferrando, R. Searching for low-energy structures of nanoparticles: a comparison of different methods and algorithms. *J. Phys. Condens. Matter* **21**, 084208 (2009).
10. Wales, D. J. & Doye, J. P. K. Global Optimization by Basin-Hopping and the Lowest Energy Structures of Lennard-Jones Clusters Containing up to 110 Atoms. *J. Phys. Chem. A* **101**, 5111–5116 (1997).
11. Rossi, G. & Ferrando, R. Global optimization by excitable walkers. *Chem. Phys. Lett.* **423**, 17–22 (2006).
12. Grimme, S., Antony, J., Ehrlich, S. & Krieg, H. A consistent and accurate *ab initio* parametrization of density functional dispersion correction (DFT-D) for the 94 elements H-Pu. *J. Chem. Phys.* **132**, 154104 (2010).

13. Gingerich, K. A., Shim, I., Gupta, S. K. & Kingcade, J. E. Bond energies of small metal clusters. *Surf. Sci.* **156**, 495–503 (1985).
14. Barcaro, G. & Fortunelli*, A. The Interaction of Coinage Metal Clusters with the MgO(100) Surface. *J. Chem. Theory Comput.* **1**, 972–985 (2005).
15. Wang, J. & Wang, S.-Q. Surface energy and work function of fcc and bcc crystals: Density functional study. *Surf. Sci.* **630**, 216–224 (2014).
16. Engel, J., Francis, S. & Roldan, A. The influence of support materials on the structural and electronic properties of gold nanoparticles – a DFT study. *Phys. Chem. Chem. Phys.* **21**, 19011–19025 (2019).

Conclusions

The aim of the research performed for this thesis was to search for the configuration of the global minimum of an Au_n/MgO ($n < 20$ atoms) system and for this, various methodologies were employed. A systematic build-up method, using chemical intuition and the lowest energy cluster obtained previously, i.e. one atom smaller in size and global optimisation methods, specifically GA, building on the idea of natural selection to cross favourable structures in an attempt to find even more favourable ones were used. Both these search methods use DFT to calculate the energy of the electronic structure. A Monte Carlo global optimisation was also employed with empirical potentials used to calculate the energy of the electronic structure.

From the DFT searches performed, the preferable adsorption site for a single Au on MgO is on an oxygen, with an adsorption energy (E_{ads}) of 1.37 eV. From this single atom placement, further atoms were added one-by-one. As the cluster grows, there is a clear transition in the lowest energy structures, from perpendicular planar structures with respect to the surface, to parallel planar structures at Au_6 onwards. From Au_6 to Au_{19} all the most stable clusters are parallel planar with an Au (111) interface with the MgO. Although this means that there is symmetry mismatch between the cluster and the support, the interface adopted minimises the surface energy of the Au (1.137 J m⁻² for an Au (111) surface and in comparison, 1.359 J m⁻² for a (001) surface). This implies that, for clusters below 20 atoms, the surface energy has a greater influence on the shape of the Au cluster adopted than the mismatch, resulting in the 2D (111) structures.

As the cluster grows, the adsorption energy (E_{ads}) per atom decreases, the reduction in the surface interaction is also reflected in the reduction in charge transfer from the support to the cluster, obtained from the Bader charge analysis. Additionally, the cohesive energy (E_{coh}), that is the measure of the interaction between Au atoms in the cluster, increases with cluster growth. Both these trends (E_{ads} and E_{coh}) are due the increasing interface symmetry mismatch and the increase in the coordination of the Au atoms with cluster size. The increase in the coordination of the Au atoms from cluster growth also has an effect on the average Au-Au distance ($\overline{d_{\text{Au}-\text{Au}}}$), which increases from 2.522 Å for Au_2 to around that of an Au-Au monolayer (2.74 Å). The Au-surf ($\overline{d_{\text{Au}-\text{S}}}$) increases from 2.310 Å to 2.791 Å, this is influenced by the decreased surface interaction that also leads to the reduction in E_{ads} .

From the Monte Carlo optimisation, the Au structures determined to be the lowest in energy (for $n = 5 - 19$) were all 3D with a (001) interface. Once these structures were optimised using

DFT, the atoms in the cluster rearranged and their DFT energies were higher than their 2D (111) counterparts. From these results, it was determined that the empirical interatomic potentials, derived from bulk properties and used to obtain the energy of the structures were not suitable for supported systems with clusters of this size. The predicted structures produced by the Monte Carlo method and the increase in the mismatch (of a 111 interface) as the cluster grows, suggests the presence of a transition from 2D (111) to 3D (001) shapes at clusters sizes between 20 - 50 atoms. There is also likely to be a drive from 2D to 3D structures to decrease the number of Au atoms at the surface, i.e. the greater the ratio of surface to bulk atoms, the lower the coordination of the gold and the higher in energy the system.

Once the most stable structures for Au_n/MgO ($n < 20$) were established by the DFT calculations, they were then used to study the Ostwald ripening process through the application of microkinetics. For each cluster size, calculations of the barriers to ripening (E_a) and the reaction energy associated with the attachment of a single atom (E_r) to the cluster were performed. This starts with a single atom and initial calculations determined that when taking the most favourable path across the hollow, the barrier for single atom diffusion across the surface was 0.29 eV. From the calculation of all the barriers and the reaction energies up to Au_n , $n = 10$, a trend emerged. While all of the energy barriers are relatively low (< 1.05 eV), E_a is generally lower for the formation of an even numbered cluster. This is because, in the creation of an odd numbered cluster, the cluster has spin associated with the unpaired electron of the odd Au, causing some unfavourable interactions. However, an even numbered cluster, has full pairing of the atoms leading to no overall spin, as shown by the spin magnetisation and in the DOS and COHP graphs. A similar trend is observed for the energy of reaction (E_r), the formation of an even numbered cluster E_r being more negative, showing a more favourable reaction.

Once the ripening barriers and reaction energies were determined, then these values were integrated into microkinetic models. Microkinetic modelling is a method whereby the process of interest is broken down into its elementary reaction steps. This allows for a discussion of reaction dynamics and rates based on the partition function of each individual system. From the partition function, the thermodynamical variables (entropy, enthalpy and therefore, Gibbs free energy) can be defined. This is how the effect of temperature is incorporated into the evaluation of the ripening process. At the starting dispersions defined (maximum of $9564 \text{ m}^2\text{g}_{\text{Au}}^{-1}$, around 20x higher than a typical catalyst dispersion), results showed that below 160K, the Au_1/MgO system remained stable and ripening processes did

not occur. Above this temperature, the greater the coverage (the lower the dispersion), the quicker ripening processes occurred, e.g. at $\theta_{0.9}$ (90%) coverage after 1 second at 510 K, the fraction of Au_1 was down to 86% of its starting coverage. However, for $\theta_{0.1}$ (10%) coverage after 1 second at 510 K the fraction of Au_1 only went down to 99% of the starting coverage. An increase in the temperature also resulted in quicker ripening, e.g. with a starting coverage of $\theta_{0.9}$ after 1 second at 260 K, the fraction of Au_1 reduced to 98%, while with the same starting coverage but at 510 K for the same times frame, the fraction of Au_1 was down to just below 86% of its starting coverage.

Out of all the cluster sizes, the conversion is greatest to the Au_{10} cluster. This is as expected because Au_{10} is the most stable (and largest) cluster size in the simulation. In terms of the other possible sizes (Au_2 - Au_9), there are higher fractions of even numbered clusters produced, particularly Au_4 and Au_8 . This is reflective of the lower energy barriers (E_a) and more negative reaction energies (E_r) toward the even number clusters.

As well as ripening, the digestion process was also simulated using microkinetic modelling. The system for this model starts with an initial coverage of $\theta_{0.1}$ of Au_{10} clusters. There is very little conversion from Au_{10} to any other cluster size, consistent with Au_{10} being the most stable cluster in the system. Peaks are seen at moderate temperatures around 210 K after 1 second for Au_9 and Au_8 , which is consistent with the slight decrease in Au_{10} at these same temperatures. This implies some digestion is occurring to form these smaller clusters. After 1 second at the higher temperatures > 350 K, a peak at Au_2 , reduced conversion from Au_{10} and the decrease in Au_8 and Au_9 implies diffusion processes become more widespread and the system undergoes further ripening processes over digestion.

This study shows that there is considerable difficulty in the computation of low energy Au clusters in a system of this type. Further developments in methodologies are required to increase the scope of the searches as well as their accuracy in predicting the most stable shapes in similar supported systems. However, the combination of methodologies provided a wide screening of possible configurations and yielded interesting results for this system, providing useful data pertaining to structural and electronic trends of growing clusters.

Alternative ways of predicting low energy clusters should also be sought. A greater understanding of structural/electronic features associated with stability, might provide an alternative way of predicting favourable configurations. For example, this could include measuring the symmetry of clusters, to determine a particular preference for particular point groups.

With regard to expanding understanding of growth processes, greater information about how systems are influenced by certain factors could be achieved by a microkinetic study with wider parameters. For example, wider temperature ranges and metal coverages (related to dispersion) and longer time frames could be used. Also necessary for future understanding of growth processes would be a suitable model for coalescence. As previously described, modelling coalescence (or Smoluchski ripening) is very complex as there are a range of possible ways for clusters to move across the surface e.g. rolling or leap frogging. How the atoms in the migrating cluster interact with each other, as well as how they interact with the surface during diffusion would need to be considered in a viable simulation.

The research performed aimed to develop a greater understanding of stability and growth in the Au_n/MgO system. The study was successful in that the most stable structures of Au clusters on MgO, for up to 19 atoms were obtained. Discussion of the results showed that surface energy, structural mismatch as well as bonding interactions within the cluster and between the cluster and the support were all factors that influenced the shape of Au NP's. The growth process, Ostwald ripening, was also analysed using microkinetic modelling simulations. The results from this showed that even at very low metal dispersions and low temperatures (> 160 K) ripening processes occurred in order to increase the stability of the system. Further analysis showed that some cluster sizes were more stable than others, and as a result remained for longer on the surface. These conclusions can be used to support the findings of experimental catalyst characterisation and to inform future preparation of effective and resistant catalysts.

